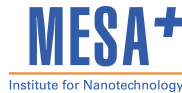


Interface engineering of spin-tunnel contacts to silicon

Towards silicon-based spintronic devices

PROMOTIECOMMISSIE

VOORZITTER:	prof. dr. ir. A. J. Mouthaan	
SECRETARIS:	prof. dr. ir. A. J. Mouthaan	Univ. Twente, EWI
PROMOTOR:	prof. dr. J. C. Lodder	Univ. Twente, EWI
ASS. PROMOTOR:	dr. R. Jansen	Univ. Twente, EWI
REFERENT:	dr. ir. W. Van Roy	IMEC, Belgium
LEDEN:	prof. dr. Y. Suzuki	Osaka Univ., Japan
	prof. dr. A. Fert	Univ. Paris-Sud, France
	prof. dr. B. J. Hickey	Univ. of Leeds, UK
	prof. dr. R. A. M. Wolters	Univ. Twente, EWI
	dr. ir. L. Abelmann	Univ. Twente, EWI



The research described in this thesis was funded by the Netherlands Nanotechnology network, NANOIMPULS and NANONED, supported by the Ministry of Economic Affairs, the Netherlands. The research was carried out in the Nanoelectronics group of the MESA⁺ institute for nanotechnology, the University of Twente.

Printed by:
Wöhrmann Print Service
Loskade 4
7202 CZ Zutphen, the Netherlands
www.wps.nl

© Byoung-Chul Min, Enschede, 2007
No part of this work may be reproduced by print,
photocopy or any other means without the permission
in writing from the publisher.

ISBN: 978-90-365-2543-5

INTERFACE ENGINEERING OF SPIN-TUNNEL CONTACTS TO SILICON

TOWARDS SILICON-BASED SPINTRONIC DEVICES

PROEFSCHRIFT

ter verkrijging van
de graad van doctor aan de Universiteit Twente,
op gezag van de rector magnificus,
prof. dr. W.H.M. Zijm,
volgens het besluit van het College voor Promoties
in het openbaar te verdedigen
op vrijdag 31 Augustus 2007 om 15.00 uur

door

Byoung-Chul Min

geboren op 2 Januari 1971

te Kyungbook, Zuid Korea

Dit proefschrift is goedgekeurd door

de promotor: Prof. dr. J. C. Lodder

de assistent promotor: Dr. R. Jansen

INTERFACE ENGINEERING OF SPIN-TUNNEL CONTACTS TO SILICON

TOWARDS SILICON-BASED SPINTRONIC DEVICES

DISSERTATION

to obtain
the doctor's degree at the University of Twente,
under the authority of the rector magnificus,
prof. dr. W.H.M. Zijm,
on account of the decision of the graduation committee,
to be publicly defended
on Friday 31 August 2007 at 15.00.

by

Byoung-Chul Min

born on 2 January 1971

in Kyungbook, South Korea

This dissertation is approved by

the promoter: Prof. dr. J. C. Lodder

the assistant promoter: Dr. R. Jansen

Contents

1	Introduction to silicon-based spintronic devices	1
1.1	Spintronics and spin transistor	1
1.2	Spin injection and spin-polarized transport in semiconductors	4
1.3	Silicon-based spin-MOSFET	7
1.3.1	Device concept and requirements	7
1.3.2	Requirements for source and drain contacts	10
1.4	Motivation and thesis outline	11
2	Tunable spin-tunnel contact to Si with low-work-function interfacial nanolayers	15
2.1	Introduction and motivation	16
2.2	FM/I/Si contacts	17
2.3	Fabrication of FM/I/Si contacts	19
2.4	FM/I/Si contacts with conventional ferromagnets (Co, NiFe)	22
2.4.1	FM/I/Si contact to lightly-doped Si	23
2.4.2	FM/I/Si contact to heavily-doped Si	25
2.5	FM/I/Si contacts with low-work-function ferromagnets (Gd)	27
2.5.1	Schottky barrier height of FM/I/Si contact	27
2.5.2	Fabrication of contacts with Gd	29
2.5.3	Schottky barrier removal with low work-function ferromagnet	30
2.5.4	RA product of NiFe/Gd/I/Si contacts	32
2.5.5	Work function engineering with a Gd interlayer	35
2.5.6	Structural and chemical properties of NiFe/Gd/I/Si contacts	37
2.6	Conclusions	42

3	Magnetic tunnel junctions using low work-function ferromagnet	45
3.1	Introduction and motivation	45
3.2	Gd and Gd-FM alloys	47
3.2.1	Magnetic properties of Gd	48
3.2.2	Gd-FM alloys	48
3.2.3	Gd/FM and Gd/insulator interfaces	51
3.3	Fabrication of magnetic tunnel junctions	52
3.4	MTJs with a low work-function Gd interlayer	54
3.5	MTJs with a Gd/Co bi-layer	60
3.6	Conclusions	68
4	Engineering of spin tunnel contacts to Si using Cs	71
4.1	Introduction and motivation	71
4.2	Fabrication of FM/I/Si contacts with Cs	72
4.3	Effect of Cs-deposition on Schottky barrier	74
4.4	Conclusions	79
5	Magnetic properties of nano-scale magnetic elements	81
5.1	Introduction and motivation	81
5.2	Fabrication of nano-scale magnetic elements	84
5.2.1	Laser interference lithography using image reversal technique	84
5.2.2	Pattern transfer using lift-off process	88
5.3	Characterization of nano-scale magnetic elements	91
5.3.1	Vortex structure in circular nano-scale elements	92
5.3.2	Inter-dot magnetic coupling in densely packed arrays	96
5.4	Conclusions	103
6	Prospects for Si-based spintronic devices	105
6.1	Introduction and motivation	105
6.2	Towards electrical spin injection and detection in Si	108
6.2.1	Prospects for MR observation in Si spin-MOSFET	108
6.2.2	Design of the source and drain contacts	110
6.2.3	Vertical geometry	112
6.2.4	Lateral geometry	115
6.3	Stray field in the Si channel	117
6.4	Conclusions	121
7	Conclusions	123
	Bibliography	129

Appendices	141
A. Process details of the fabrication of MIS contacts	141
B. Process details of the fabrication of the vertical geometry for two-terminal MR observation	145
Summary	151
Samenvatting	155
Acknowledgements	159
Curriculum Vitae	161

Introduction to silicon-based spintronic devices

This introduction presents the device concepts of a spin transistor and the motivation of the thesis. A brief history of spintronic devices is described to understand the concept of metal-based and semiconductor-based spintronic devices. We discuss the issues of spin injection and spin-polarized transport in semiconductors, and explain why silicon is selected as a semiconductor material. The requirements and obstacles for the realization of a silicon-based spin transistor will be discussed. We present the main motivation of the thesis, which is to investigate the issues for developing a silicon-based spintronic devices and to provide the solutions towards a realization of such devices.

1.1 Spintronics and spin transistor

Microelectronics is based on the transport, manipulation, and storage of charge, with the transistor as the central element[1]. Over the past five decades, there has been tremendous reduction of the size of the transistor from a few cm to 100 nm to improve performance of the devices. It is expected that this trend, so called "Moore's law", might approach a physical limitation, and perhaps, a technology more than scaling down the device size is required to continue the miraculous improvement of electronic devices. On the other hand, as mobile devices—such as cellular phones, digital cameras, personal digital assistants

(PDAs), and laptop computers—have become ubiquitous, the demand for reliable non-volatile memories increases explosively. The non-volatility of a memory is a great advantage for mobile information devices, since their functions rely on the limited battery life.

Given this, it is not surprising that alternative types of electronics are being developed. One such approach is spintronics, which represents an emerging field of electronics based on the spin of electron[2, 3]. The use of electron spin may provide non-volatility to the electronic devices. Spintronics has diverse fields of applications, such as magnetic data storages, memories, magnetic sensors, and microwave components. For instance, one can find the most famous success of spintronics in hard disk drives. The hard disk drive contains magnetic materials not only in the recording media, but also in the read head, which consists of magnetic multi-layers[4]. The unique property of this component is the magneto-resistance (MR), the resistance change in response to a magnetic field.

Although the MR effect in the ferromagnetic transition metals and alloys has been known for many years, a revolution of spintronics has begun since Fert *et al.*[5]and Grünberg *et al.* [6] discovered the giant magnetoresistance (GMR) effect in magnetic multilayer systems. They found that the inter-layer exchange interaction between the adjacent magnetic layers separated by a thin nonmagnetic spacer favors an anti-ferromagnetic configuration of the magnetic layers in remanent state. Because of the spin dependent scattering in the multilayer system, the resistance of the anti-ferromagnetic configuration in remanent state is much larger than that of ferromagnetic configuration obtained when an external field is applied. This resulted in the observation of a giant magnetoresistance ratio of 44% at 4.2 K[5]. It had been difficult to apply this effect to the real electronics until a soft magnetic GMR system, namely "spin-valve", was invented[7]. In the spin-valve system, the magnetization of one magnetic layer is pinned by the exchange anisotropy from an anti-ferromagnetic layer or by the large coercivity of the layer itself, while the magnetization direction of the other magnetic layer can be changed by a small magnetic field. Consequently, one can control the anti-ferromagnetic or ferromagnetic configuration using a relatively small magnetic field.

Large MR effects have also been expected in the tunnel junction system using a spin-polarized tunneling[8]. Moodera *et al.* [9] and Miyazaki *et al.* [10] have discovered the room-temperature tunnel magnetoresistance (TMR) in the magnetic tunnel junction (MTJ) consisting of two magnetic layers sep-

arated by a thin insulating barrier. The MTJ became the main building block of a new type of non-volatile solid state memory, so-called MRAM (Magnetoresistive Random Access Memory)[11].

The application of spin-dependent transport is not limited to metal-based spintronics, but also can be extended to semiconductor-based spintronics combining ferromagnetic properties and semiconductor characteristics[2, 3, 12, 16–18]. This new area has arrested a lot of the scientific interests with great expectations for novel devices by transforming the spin information into an electrical signal, and vice versa. For example, one can imagine a device which has the memory function of the magnetic materials and the amplification function of the semiconductor. One of the main goals of the semiconductor-based spintronics is to realize a three terminal device, a spin transistor, which has memory as well as amplification functionalities in one device.

The first type of spin transistor is based on the spin dependent transport in the metallic layers. The spin-valve transistor (SVT)[13]and the magnetic tunnel transistor (MTT) [14] are three-terminal hybrid devices consisting of a spin-polarized or a non-spin-polarized hot electron emitter, a ferromagnetic metal (FM) base, and a semiconductor collector. In the SVT and MTT, hot electrons are injected into the FM base by tunneling, scattered spin-dependently in the FM base, and collected in the conduction band of the semiconductor[15]. The magnetic response of the SVT and MTT, the so-called magnetocurrent (MC), is determined by spin-dependent transmission in the FM base, and, depending on geometry, by the spin-polarized tunneling from the emitter[15]. These devices show a large MC of a few hundred to a few thousand percent, but they do not provide the amplification function up to now.

The second type of spin transistor is based on the spin dependent transport in a semiconductor channel with two ferromagnetic contacts. Datta and Das have proposed the first concept of a spin field-effect transistor (spin-FET)[19]. Afterwards, various designs of spin transistors have been proposed with different structures, materials, and current manipulation mechanisms, but the realization of those devices has yet to be demonstrated[3, 16–18, 21, 22]. Although there are also different types of spin transistors, in this thesis, we concentrate our efforts on a spin transistor with a non-ferromagnetic-semiconductor channel and ferromagnetic metal contacts. One example of such devices is the spin-MOSFET[21], a gate-controlled magnetoresistive device with a semiconductor channel and a ferromagnetic source and drain, in

which the channel conductance can be modulated by the relative alignment of the source and drain magnetizations.

The motivation of the thesis is to investigate the issues for the development of Si-based spintronic transistors and to provide the solutions towards a realization of such devices. For a practical realization of this device, the electrical injection, transport, and detection of spin-polarized carriers in the semiconductor are required.

1.2 Spin injection and spin-polarized transport in semiconductors

There are many excellent original papers and review articles on the spin injection and spin-polarized transport in semiconductors [2, 3, 16-18, 23-38]. In this section, we introduce a very brief part of them, and restrict our discussions to within the scope of the thesis.

The target device of the thesis is a Si-based spin-MOSFET (see Fig. 1.1) structure consisting of two spin-tunnel contacts for the source and drain electrodes, which operates in the diffusive transport regime. The spin-MOSFET is analogous to metal-based spin-valve structures of which a non-magnetic metal spacer is replaced by a semiconductor channel. In order to realize the spin MOSFET, three requirements should be satisfied.

- (1) Injection of spin-polarized current of electrons from FM into semiconductor
- (2) Transport of electrons through the semiconductor without losing the spin information
- (3) Detection of spin-dependent transmission into the FM drain contact

It has been found that the first requirement is already a big challenge. The difficulty arises from the fundamental conductivity mismatch between metal and semiconductor[25]. The simplest way to inject spin-polarized current of electrons into a semiconductor is probably to form a direct contact of a ferromagnetic metal on a semiconductor. It has been shown that, in the diffusive transport regime, a direct contact of a ferromagnetic metal on a semiconductor gives a series circuit with a very small spin-dependent FM resistance and

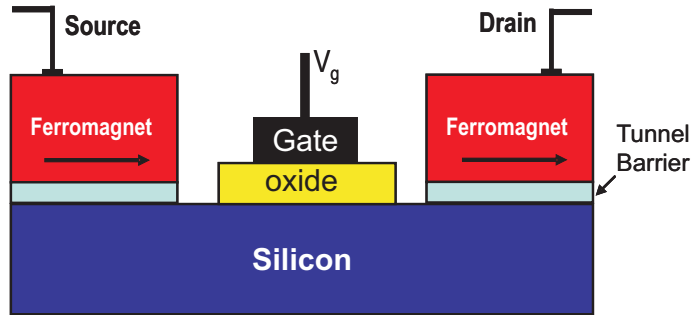


Figure 1.1. A schematic diagram of spin-MOSFET consisting of a ferromagnetic source, a Si channel, and a ferromagnetic drain.

a very large spin-independent semiconductor resistance, resulting in almost zero spin asymmetry of the current in the semiconductor[25].

This conductivity mismatch problem can be settled by introducing a spin-dependent resistance at the FM/semiconductor interface[26, 27]. If we introduce, for example, a thin tunnel insulator between the FM and Si, the tunnel barrier provides additional spin-dependent tunnel resistance. If the resistance of the contact is higher than a critical value, it is possible to achieve a non-equilibrium spin polarization in the semiconductor as depicted in Fig. 1.2. This criterion gives rise to a lower limit of the contact resistance for observing the electrical spin injection in an FM/semiconductor system.

GaAs has been a pilot system to study the spin injection and the spin-polarized transport in semiconductors, since optical techniques present versatile tools to detect the spin polarization in GaAs[3, 17, 23, 24]. Many experiments have recently shown that it is possible to inject spin-polarized carriers from FM metals such as Co and Fe into GaAs, using tunnel barriers to obtain conductivity matching[23, 24, 31-34].

We have selected Si as a semiconductor channel because Si has a smaller spin-orbit coupling and a lattice with inversion symmetry, and the mainstream semiconductor industry is based on Si technology. The properties of Si result in a longer spin life-time with less spin-relaxation mechanisms than that of III-V compound semiconductors. There are four mechanisms of spin relaxation in semiconductor: the Elliott-Yafet (EY), D'yakonov-Perel (DP), Bir-Aronov-Pikus (BAP), and hyperfine interaction mechanisms, respectively[3]. The EY mechanism in Si is expected to be weak given the small spin-orbit

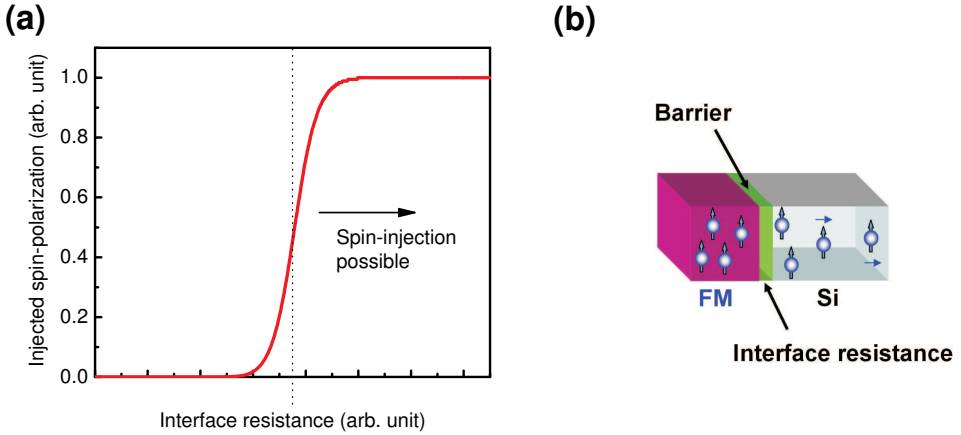


Figure 1.2. Criteria for the electrical spin injection. (a) Spin polarization in semiconductor vs the resistance-area product. (b) A contact of ferromagnet/semiconductor

coupling in materials with light elements[3]. The DP and BAP mechanisms are negligible for n -type Si, since the DP mechanism is associated with materials lacking inversion symmetry and the BAP mechanisms is substantial only for p -type semiconductors[3]. The absence of nuclear spin in the most abundant Si isotope reduces spin relaxation via hyperfine interaction. Considering the fact that the τ_s in n -type GaAs ($n_d = 10^{22} \text{ m}^{-3}$) exceeds 100 ns at 5 K and 1 ns at 100 K[35], a longer spin lifetime may be expected for n -type Si.

A similar approach as was used to inject spin polarized carriers into GaAs may be envisioned for the technologically most important semiconductor, Si. However, there has been no evidence of spin accumulation in Si. A complication is that optical methods to detect spin polarization in, for example, GaAs, are difficult to use for Si owing to the indirect bandgap of Si. A fully electrical device such as the spin-MOSFET with MR is needed to demonstrate spin injection into Si. Unfortunately, no electrical spin injection into Si has been demonstrated in the diffusive transport regime[3, 39]. If the spin polarization in the semiconductor is detected by optical technique, it is sufficient to make the resistance of the tunnel contact larger than a critical value to overcome the conductivity mismatch. However, if this spin polarization is to be transformed into an electrical signal, for instance, by measuring MR using a second FM detector contact, an extra condition, not relevant for optical detection, appears[16, 27]. Namely, the total device resistance (R) should be

as small as possible, since it enters in the denominator of the MR response ($\Delta R/R$). This leads to an upper limit to the contact resistance, which will be discussed in the next section. The different contact requirements for spin injection (single FM contact) and MR observation (two FM contacts) may lead to the situation that a contact that has been demonstrated to work for spin-injection (as detected for example by optical detection, or by non-local detection), might not work for MR observation in a two terminal source-drain geometry. Therefore, we examine the requirements in more detail in the next section.

1.3 Silicon-based spin-MOSFET

This section describes the device concept of a silicon-based spin-MOSFET, and the requirements to realize the device. We introduce a theoretical consideration, which provides the criteria to observe magnetoresistance signal in a semiconductor channel with two ferromagnetic contacts. We establish three requirements for the source and drain contacts.

1.3.1 Device concept and requirements

Figure 1.1 depicts the basic concept of the Si-based spin-MOSFET, which is very similar to an ordinary MOSFET except for the ferromagnetic source and the drain. The structure in Fig. 1.1 is slightly different from original devices proposed by Sugahara *et al.*[21] in that the Schottky junctions or the *PN* junctions of the original device are replaced by tunnel contacts, aiming to avoid the conductivity mismatch problem. The operation principle of this device is very simple and analogous to the metal spin-valve system. The resistance of this device depends on the relative magnetization orientation of the source and drain contacts. If the magnetization orientations of the source and drain contacts are parallel (anti-parallel), the resistance of the channel is low (high). As a consequence, it is possible to manipulate the resistance of the Si channel by controlling the magnetic configurations of the source and drain contacts as well as by applying the gate bias on the Si channel like in a conventional MOSFET. This is the main difference of this device in comparison with the Das and Datta spin-FET, where the gate bias is used to actively modulate the spin orientation of the non-equilibrium spin-polarized carriers

in a semiconductor channel.

If we set aside the current manipulation in the semiconductor by a gate bias, the Si spin-MOSFET can be modeled as a structure consisting of ferromagnet/ insulator/ silicon/ insulator/ ferromagnet (FM/I/Si/I/FM) layers[16, 21, 27]. Figure 1.3(b) depicts the simplified spin MOSFET structure consisting of a ferromagnetic source, a Si channel, and a ferromagnetic drain. Fert and Jaffrès [16, 27] have presented a calculation to obtain the MR response of this structure in the diffusive transport regime with flat band approximation, basically treating the semiconductor as a low conductivity nonmagnetic metal. According to their calculation, the observation of the MR signal of the device is possible in a relatively narrow range of the contact resistance. We have followed the theoretical considerations proposed by Fert and Jaffrès[16, 27] to calculate the MR response of the simplified MOSFET. One can also refer the calculations of Ref. [37, 38], where one has taken into account the effect of the electric field in semiconductor. The MR is given by Eq. (23) and (25) in Ref. [27], where resistance in the parallel configuration (R^P) increases exponentially with increase of the tunnel barrier thickness, while the resistance difference (ΔR) between the parallel and antiparallel configuration saturates to the maximum value. The MR of the FM/I/Si/I/FM structure is at the maximum at certain value of the contact resistance, and decreases with changing the contact resistance as shown in the Fig. 1.3(a). The maximum MR is given by[16, 27]

$$\left[\frac{\Delta R}{R^P} \right]^{MAX} = \frac{\gamma^2}{1 - \gamma^2}, \quad (1.1)$$

where γ is the interface spin-asymmetry coefficient. Consequently, a reasonable value of magnetoresistance (MR) can be obtained in the FM/I/Si/I/FM structure only if the RA product of both the FM/I/Si contacts is in a relatively narrow range given by [16, 27]

$$\rho_N t_N < r_b^* < \frac{\rho_N (l_{sf}^N)^2}{t_N}, \quad (1.2)$$

where ρ_N is the resistivity of semiconductor, r_b^* is the interface resistance, l_{sf}^N is the spin diffusion length in semiconductor, and the t_N is the semiconductor channel length. The width of this range depends on the channel length as shown in Fig. 1.3(a). Basically, the shorter the channel is, the wider the range is. It is desirable to make the channel length short enough to observe the MR

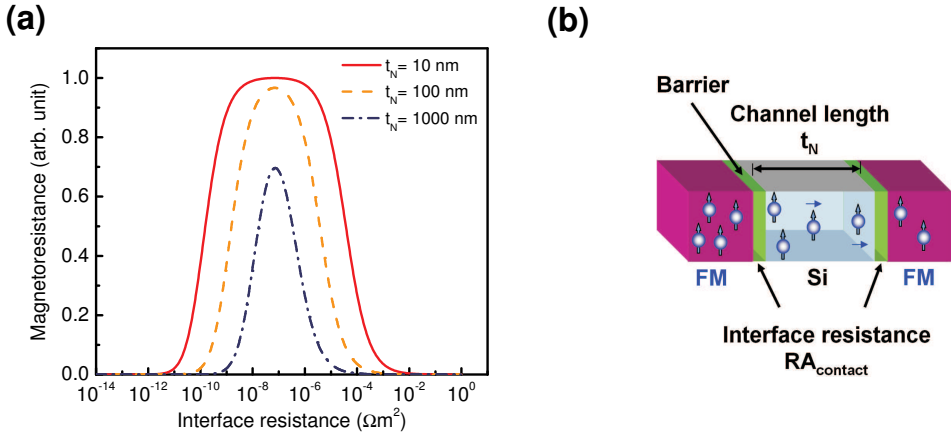


Figure 1.3. Criteria for observing MR response in spin-MOSFET. (a) Calculated magnetoresistance vs the resistance-area product of the contact with three different length of the Si channel. (b) A simplified spin MOSFET structure consisting of a ferromagnetic source, a Si channel, and a ferromagnetic drain. In this calculation, we used the spin lifetime of electrons in Si ($\tau_s = 7$ ns), temperature ($T = 300$ K), a dopant density of the Si channel ($n_d = 10^{21} \text{ m}^{-3}$), and the resistivity (ρ) versus the dopant density relation from Ref. [42].

of the device in a wide range.

We have calculated the MR response of the simplified MOSFET as a function of two parameters, RA product of the contact and dopant density of the Si channel using Eq. (23) and (25) in Ref. [27]. Figure 1.4 shows the calculation, where the color code designates the MR value of spin MOSFET structure. There is a certain range of RA in which MR can be observed. If the RA is located outside this range, no significant MR is expected. This figure allows us to determine the optimum range of the RA product of the contact for high MR as a function of the dopant density (n_d) of Si. In this calculation, we used the length of a Si channel (100 nm), the temperature (300 K), and the resistivity versus the dopant density relation from Ref. [42]. The spin lifetime of electrons in Si ($\tau_s = 7$ ns) was taken from electron spin resonance (ESR) data [3]. It was optimistically assumed in the calculation of Fig. 1.4 that the spin lifetime is constant over the entire range of the dopant density and the spin diffusion length follows the equation for non-degenerate Si for simplicity. Generally, the spin lifetime of electrons in a semiconductor is

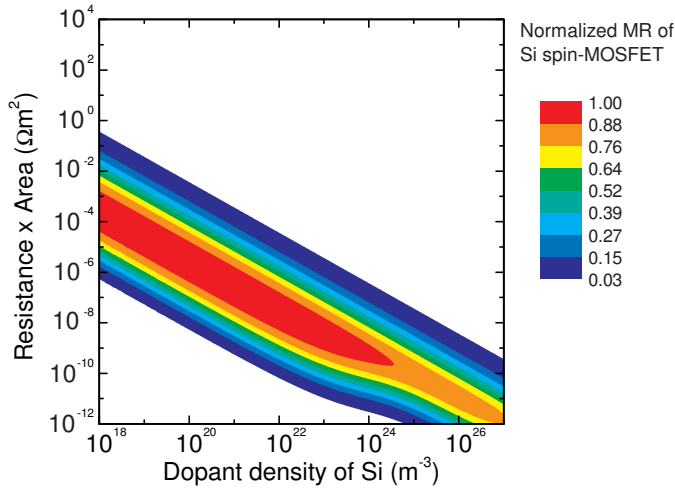


Figure 1.4. Calculated MR of FM/I/Si/I/FM spin-MOSFET structure as a function of the contact resistance-area product and the Si dopant density. The colour legend represents the value of normalized MR. The parameters used in the calculation is the same as those in Fig. 1.3

reduced at higher dopant density[35]. From Fig. 1.4, we can obtain that, for example, for a dopant density of 10^{21} m^{-3} , the RA product of both the FM contacts should lie between 10^{-8} and $10^{-5} \Omega\text{m}^2$.

1.3.2 Requirements for source and drain contacts

The Si spin-MOSFET has two spin-tunnel contacts for the source and drain electrodes. It is very important to secure proper contacts to inject and to detect highly-spin polarized carriers in Si. One of the most promising candidates for these contacts is a ferromagnetic metal/ insulator/ Si (FM/I/Si) contact, since this type of contact would, in principle, allow us to tune the resistance-area (RA) product of the contact by varying the insulator thickness. Although it is possible to adopt the Schottky tunnel contact that has been used in Fe/GaAs system, we exclude this option because of the silicide formation at the FM/Si interface[40, 41]. Inserting a tunnel barrier between FM and Si provides another benefit, as it avoids silicide formation at the FM/Si interface that is known to be detrimental to the spin transport[43]. In order to inject

and detect spin polarized carriers in Si, we have established the following three requirements for the ferromagnet/ insulator/ Si (FM/I/Si) contacts:

- (1) Suitable resistance-area (RA) product
- (2) High tunnel-spin polarization (TSP)
- (3) Controlled magnetic switching

The first requirement represents that the RA product of the source and drain contact should be matched to Si channel as shown in Fig. 1.4. The second requirement states that the source and drain contacts should have a high TSP to inject and detect spin-polarized carriers in the Si channel. It is desirable to make the TSP as high as possible to obtain a large MR in the spin-MOSFET, since the maximum MR is determined by the TSP of the injected carriers from ferromagnet (Eq. 1.1). The MR signal depends on the relative magnetic alignment of the ferromagnetic source and drain. This leads to the third requirement, the ability to control the magnetization of the ferromagnetic source and drain contact. Also, the spin polarization of carriers is closely related with the magnetization of ferromagnet. It is beneficial to obtain homogeneous magnetization in the source and drain contact, and to minimize spurious magnetic coupling from the magnetic surroundings. The distance between the spin injector and detector will be determined by a characteristic length scale of the spin transport in Si. Because the distance is expected to be of the order of a few hundred nanometers or less, it is important to understand the magnetic interactions of closely-packed nanoscale magnetic elements with this length scale.

1.4 Motivation and thesis outline

As discussed in the previous sections, the advent of semiconductor-based spintronics opens up a possibility to design novel devices combining ferromagnetic properties and semiconductor characteristics. Among various applications of semiconductor-based spintronics, the spin transistor is of a paramount importance as this device may enable the development of solid-state information devices such as high-density nonvolatile memories and reconfigurable logic gates.

The main objective of the thesis is to study the issues for the development of Si-based spintronic devices and to provide the solutions for the realization of such devices. Eventually, it is important to prove whether the conductance of a Si channel with two ferromagnetic contacts can be modulated by the relative alignment of their magnetization. In order to achieve this—as described in the previous section—three basic requirements should be satisfied for the spin-tunnel contacts for the source and drain electrodes: suitable RA product, high tunnel spin polarization, and controlled magnetic switching. It will be investigated whether real ferromagnet/insulator/Si (FM/I/Si) contacts satisfy three requirements.

Chapter 2 discusses how to develop FM/I/Si contacts that satisfy the requirements for the suitable source and drain electrodes of the Si spin-MOSFET structure. This chapter describes the fabrication of FM/I/Si contacts with various ferromagnetic materials, such as Co and $\text{Ni}_{80}\text{Fe}_{20}$ alloy, and the measurement of I - V characteristics of the contacts. The RA product of the FM/I/Si contacts will be compared with the optimum range for the MR observation in Si spin-MOSFET structure. We discuss the effect of Schottky barrier formation in FM/I/Si contacts, and clarify the major obstacles to the electrical spin injection and detection in Si in the diffusive transport regime. We present an innovative solution, based on the work function engineering of ferromagnetic materials, to overcome these obstacles and to control the RA product of the contact. This chapter also contains the characterization of the structural and chemical properties of these contacts.

Chapter 3 describes the fabrication and characterization of the magnetic tunnel junctions with a low work-function ferromagnet interlayer. The TSP of the spin tunnel contacts, developed in chapter 2, will be investigated by measuring the TMR of the magnetic tunnel junctions. This study allows us to verify whether the spin tunnel contacts with a low work-function ferromagnet interlayer can be used to inject reasonably high-spin-polarized carriers into a Si channel through a tunnel barrier. Magnetic properties of the rare earth metal, rare earth-transition metal alloys, and rare earth/transition metal interfaces will be discussed to explain the behavior of the magnetic tunnel junctions with a low work-function ferromagnet interlayer.

Chapter 4 presents an alternative approach to control and reduce the Schottky barrier height of FM/ Al_2O_3 /Si contacts by coating alkali metal atoms, such as Cs, on the Si surface prior to tunnel barrier formation. This chapter describes the fabrications and measurement that have been conducted to un-

derstand the mechanism of the reduction of the Schottky barrier height. We will investigate the possibility of the formation of two-dimensional electron gas at the n-type Si surface.

Chapter 5 is devoted to the magnetic properties of nano-scale magnetic elements fabricated by laser interference lithography (LIL) and lift-off technique. Using magnetometry and magnetic force microscopy, we study the effect of the size and shape of the elements on their magnetic configuration as well as the magnetostatic interaction among the magnetic elements that are densely packed at a length scale of 100 nm. The knowledge obtained from these studies can be used in designing the source and drain contacts of the spin-MOSFET.

Chapter 6 deals with the device-related issues and presents suitable device configurations, such as vertical and lateral geometries, to observe the MR in a Si channel between two ferromagnetic contacts. This chapter describes spurious effects owing to the current in the Si channel and the stray magnetic field from the ferromagnetic contacts, and their consequences. We present a perspective to electrical spin injection and detection in Si in the diffusive transport regime. Conclusions and outlook will be presented in chapter 7.

Chapter 2

Tunable spin-tunnel contact to Si with low-work-function interfacial nanolayers

The development of a spin-based transistor such as the spin-MOSFET requires careful design of the contacts between the ferromagnetic source/drain and the semiconductor. In this chapter, we clarify that the Schottky barrier formation in the ferromagnet/insulator/Si (FM/I/Si) contacts is a major obstacle to observe the magnetoresistance of such a device, operated in a two-terminal mode. This is partly due to the resulting large resistance area (RA) product of the contacts (precluding spin detection), and partly because of the potential energy landscape of the contacts. We present a solution to control the Schottky barrier height and RA product of spin tunnel contacts to Si by using low work-function materials, inserted between the FM and the insulator of FM/ Al_2O_3 /Si tunnel contacts. This allows tuning of the Schottky barrier height and thereby the RA product of the contacts over many orders of magnitude. Structural and chemical analysis of the spin tunnel contacts will also be presented.

2.1 Introduction and motivation

The Si spin-MOSFET structure has two spin-tunnel contacts for the source and drain electrodes, which play a decisive role in the injection and detection of the non-equilibrium spin-polarized carriers in a Si channel. The major topic in this chapter is to develop suitable contacts for the source and drain electrodes of the Si spin-MOSFET structure. As we have discussed in the previous chapter, one of the most promising candidates for these electrodes is a ferromagnetic metal/insulator/Si (FM/I/Si) contact, since this type of contact provides a possibility to inject highly spin-polarized carriers and to tune the resistance-area (RA) product of the contact. In the previous chapter, we have shown that there is a certain range of the RA product of the contacts in which magnetoresistance (MR) can be observed in the fully electrical Si spin-MOSFET structure. If the RA product of the contact is located outside this range, any significant MR cannot be expected. For example, for a dopant density of 10^{21} m^{-3} , the RA product of both the FM contacts should lie between 10^{-8} and $10^{-5} \Omega\text{m}^2$.

In this chapter, we describe the fabrication and properties of FM/I/Si contacts which satisfy the requirements for the electrical spin injection and detection in Si. Here, our discussion is concentrated on the first requirement, the RA matching to a Si channel; It will be shown, in the chapter 3, that this type of contacts also satisfy the second requirement, the high tunnel spin polarization. Section 2.2 describes the basic aspects of FM/I/Si contacts and the consequence of the Schottky barrier formation on the spin transport in Si. Section 2.3 presents the experimental details on the fabrication of the FM/I/Si contacts and the measurement of the I - V characteristics of the contacts. Section 2.4 discusses the properties of FM/I/Si contacts on n -type Si substrates with well-known ferromagnetic metals, such as $\text{Ni}_{80}\text{Fe}_{20}$ alloy and Co. The RA product of FM/I/Si contacts will be investigated as a function of tunnel barrier thickness, the oxidation time, and the doping concentration of silicon. From these results, we will examine whether the RA product of these contacts are in the proper range. It will be shown that Schottky barrier formation leads to a huge conductivity mismatch of ferromagnetic tunnel contact and Si, which cannot be solved by the well-known method of adjusting the tunnel barrier thickness. In section 2.5, we present a very effective solution to reduce and control the Schottky barrier using a low work-function ferromagnet inserted at the FM/tunnel barrier interface. It will be demonstrated that the

insertion of a low work-function interlayer in the FM/I/Si contacts provides remarkable tunability of the Schottky barrier height to Si; the FM/I/Si contacts with an ultrathin low-work-function FM interlayer secures the optimum RA product for the electrical spin injection and detection. The structural and chemical properties of FM/Gd/I/Si contacts will be discussed at the end of this section.

2.2 FM/I/Si contacts

Figure 2.1 shows schematic energy band diagrams of the metal-insulator-semiconductor (MIS) contacts with an n -type Si in both forward and reverse bias. When the metal and the semiconductor are brought into contact, a Schottky barrier is formed[44, 45]. The n -type semiconductor has a space charge region where the electrons are depleted, giving rise to additional resistance. The transport of electrons through the MIS contact depends on the width of depletion region. The basic transport mechanisms are the thermionic emission and tunneling[45]. The latter becomes important when the depletion region is thin enough. Otherwise, only the electrons which overcome the Schottky barrier can flow through the contact. In the forward bias (the spin detection condition), a negative voltage is applied to the semiconductor with respect to the metal. In the reverse bias (the spin injection condition), a positive voltage is applied to the semiconductor with respect to the metal.

The Schottky barrier in the metal-semiconductor contacts have drawn a lot of attentions, as metal-semiconductor contacts are broadly used in the fabrication of metal gates in MOSFET or MESFET devices[45]. Exact understanding of the Schottky barrier formation has been an issue of debates, and many models to explain the Schottky barrier have been proposed[44–48]. The Schottky barrier height depends on various intrinsic parameters such as the work function of metal, the electron affinity of semiconductor, the dielectric constant of insulator, the density of surface states, and the charge neutrality level at the semiconductor surface as well as extrinsic ones such as the surface preparation and thin film deposition parameters[44–48]. It is believed that the chemical bond and the formation of an electric dipole at the interfaces play an important role in the Schottky barrier height determination[47].

The existence of the Schottky barrier leads to three obstacles for the elec-

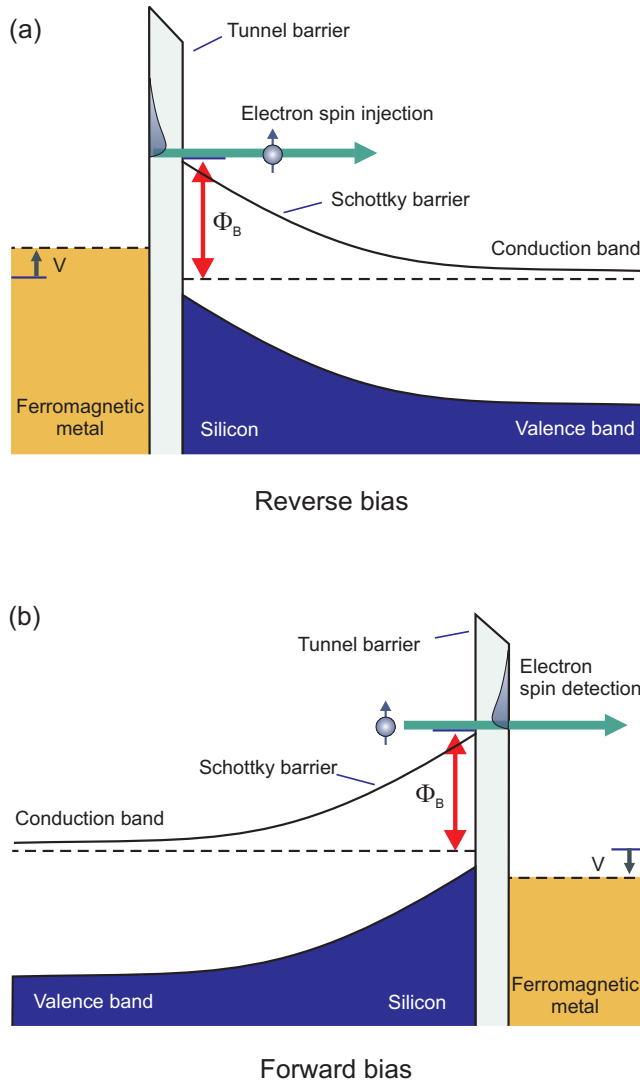


Figure 2.1. Schematic energy band diagrams of (a) the electrical spin injection (reverse bias) and (b) the electrical spin detection (forward bias) in a FM/I/Si junction. Φ_B is the Schottky barrier height, and V is the bias voltage. The broken lines depict the Fermi energy.

trical spin injection into Si and the observation of MR in the spin-MOSFET[50]. First, the current of the device is limited due to the reverse-biased Schottky barrier at one of the two FM/I/Si contacts, depending on the bias polarity. For the Schottky contact with Co and *n*-type Si with a resistivity (ρ) of 10 Ωcm (dopant density, $n_d = 10^{21} \text{ m}^{-3}$), the width of the depletion region is about 1 μm , which gives rise to additional resistance. Only the electrons which are thermally emitted over the Schottky barrier can flow across the contact[45], resulting in a low reverse bias current. The second obstacle is that the electrons involved in tunneling into the Si originated from states at elevated energy above the Fermi level of the FM source as shown in Fig. 2.1 (a), for which the TSP is significantly reduced[49]. Because the initial value of the TSP is small, the spin asymmetry in the Si cannot be expected to be large. The same argument can be applied for the spin detection condition, where the electrons tunnel into the states at elevated energy above the Fermi level of the FM drain (Fig. 2.1 (b)). The third and perhaps the most serious obstacle is that the additional resistance due to the Schottky barrier creates a huge conductivity mismatch of many orders of magnitude between the FM tunnel contact and Si channel, resulting in a negligible MR in a Si spin-MOSFET as we have discussed in chapter 1.

2.3 Fabrication of FM/I/Si contacts

Figure 2.2 depicts the layer stack of a Si/Al₂O₃/FM contact. The Si/Al₂O₃/FM contacts were fabricated on *n*-type Si (100) substrates. A 300-nm-thick SiO₂ layer was grown on a Si substrate by dry oxidation at 1150 °C. This oxide layer was patterned by lithography and wet etching to define circular contact holes with a diameter of 12 μm to 180 μm onto which the tunnel contacts were made. A 40-nm-thick sacrificial SiO₂ layer was then grown by dry oxidation at 950 °C followed by annealing at 1150 °C to obtain a high quality Si surface. This thin oxide layer was removed by HF acid just before the substrate was transferred to the load-lock chamber to prevent a native-oxide re-growth. The aluminium-oxide barrier and the ferromagnetic films were deposited by e-beam evaporation at a base pressure of 10⁻¹⁰ mbar. The tunnel barrier was deposited using a single-crystal Al₂O₃ source, followed by an additional *in-situ* plasma oxidation step to compensate for the oxygen defi-

ciency known to occur when Al_2O_3 is evaporated. This dielectric insulator provides a separation between the charges due to surface states and those on the metal. We prepared samples with different barrier thickness from 0.5 nm to 2 nm and with different oxidation time from 2.5 min to 10 min. The real thickness of an Al_2O_3 barrier after the plasma oxidation can be thicker than the nominal deposited thickness. The exact barrier thickness is determined by TEM experiments. FM layers and a gold capping layer were deposited as electrode material. Patterning for the electrical characterization was done by lithography and Ar-ion beam etching.

Figure 2.3 shows cross sectional transmission electron microscopy (TEM) images of Si/ Al_2O_3 / Co contacts on low-doped (resistivity, $\rho = 5\sim 10 \Omega\text{cm}$; dopant density, $n_d = 10^{21} \text{ m}^{-3}$) n -type Si substrates. The aluminum oxide barrier in Fig. 2.3 (a)-(d) was prepared by 0.5, 1.0, 1.5 and 2.0 nm Al_2O_3 deposition followed by 2.5 min *in situ* plasma oxidation, respectively; the barrier in Fig. 2.3 (e)-(h) was prepared by 0.5, 1.0, 1.5 and 2.0 nm Al_2O_3 deposition followed by 7.5 min *in situ* plasma oxidation, respectively. The Si/ Al_2O_3 and Al_2O_3 / Co interfaces in these TEM images are smooth, and the aluminum oxide barriers are amorphous, showing minimum thickness variation. Fig. 2.4 shows the thickness of the barrier measured from TEM images versus the deposited Al_2O_3 thickness. The thickness of the oxide barrier in the TEM images are thicker than the nominal thickness of the deposited Al_2O_3 film. Assuming that the growth rate of the oxide layer by the plasma oxidation is inversely proportional to the oxide thickness, we made simple fitting curves as shown in the Fig. 2.4. The offset for 2.5 min plasma oxidation is 1.1 nm, and the offset for 7.5 min plasma oxidation is 1.3 nm. This indicates that the thickness of the barrier shown in the TEM images might be a combination of a deposited Al_2O_3 layer and some silicon oxide layer.

We have conducted current-voltage (I - V) measurement of the Si/ Al_2O_3 / FM contacts using a source-measure unit (Keithley, Model 236) operated in voltage source mode. One port is connected to the top gold contact of each diode and the other port is connected on the large ohmic contact (1.2 mm \times 8 mm) to Si. The resistance of the metal-semiconductor is not well-defined, since the I - V characteristic is non-linear. In order to compare the RA product from one contact to another, in this thesis, the RA product of the FM/I/Si contact is defined as the voltage (V) divided by the current density (I/A) at a particular value of V .

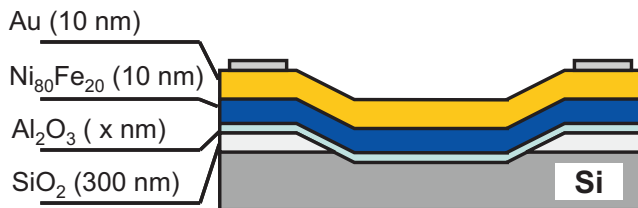


Figure 2.2. The layer stack of a $\text{Si}/\text{Al}_2\text{O}_3/\text{FM}$ contact. The tunnel contact area is defined by 300-nm-thick SiO_2 insulator layer.

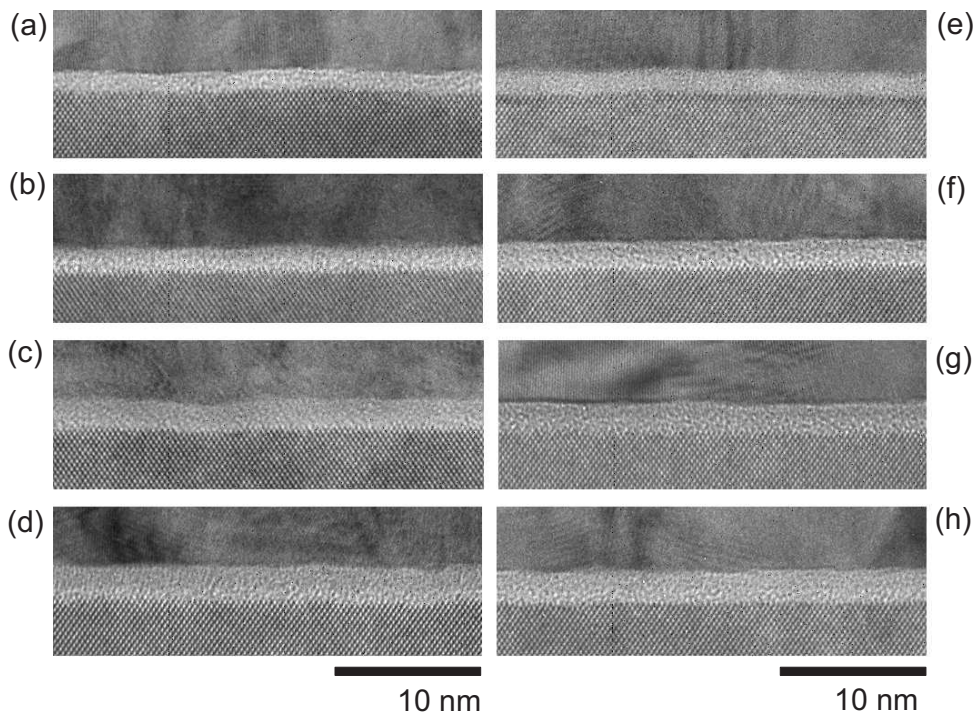


Figure 2.3. Cross-sectional TEM images of $\text{Si}/\text{Al}_2\text{O}_3/\text{Co}$ contacts on low-doped n -type Si substrates. The aluminum oxide barrier in (a)-(d) was prepared by 0.5, 1.0, 1.5 and 2.0 nm Al_2O_3 deposition followed by 2.5 min *in situ* plasma oxidation, respectively; the barrier in (e)-(h) was prepared by 0.5, 1.0, 1.5 and 2.0 nm Al_2O_3 deposition followed by 7.5 min *in situ* plasma oxidation, respectively.

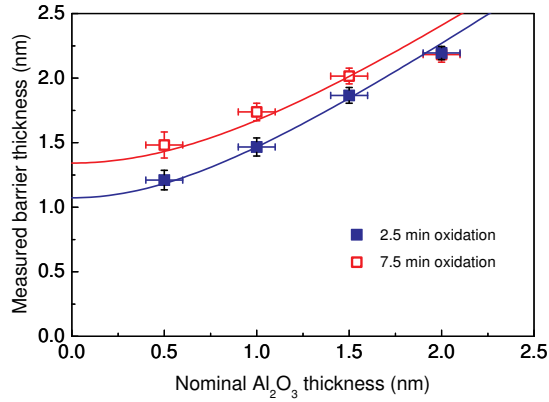


Figure 2.4. Barrier thickness measured from TEM images versus the deposited Al_2O_3 thickness. Solid (Open) square are for the samples prepared by 2.5 min (7.5 min) *in situ* plasma oxidation, as shown in Fig. 2.3

2.4 FM/I/Si contacts with conventional ferromagnets (Co, NiFe)

Ferromagnetic materials with high tunnel spin polarization and high curie temperature are the most obvious choice for the FM layer of the spin-MOSFET. In order to examine whether the RA products of these FM/I/Si contacts are in the proper range for the electrical spin injection and detection in Si, we have fabricated FM/I/Si contacts with well-known FM materials, Co and $\text{Ni}_{80}\text{Fe}_{20}$. From I - V measurements, we have investigated the RA product of FM/I/Si tunnel contacts for MR observation in the FM/I/Si/I/FM structure. Because the FM/I/Si contact consists of a Schottky barrier and a tunnel barrier, we are interested in which barrier plays a dominant role in the electronic transport. We have studied the effect of tunnel barrier thickness, the oxidation time, and the doping concentration of silicon on the resistance of the FM/I/Si contact. First, we studied the contacts to Si with low doping concentration ($n_d \sim 10^{21} \text{ m}^{-3}$) to find whether the RA product of the contact is affected by the Al_2O_3 tunnel barrier. Second, we have fabricated FM/I/Si contacts to Si with high doping concentration ($n_d \sim 5 \times 10^{25} \text{ cm}^{-3}$) to study whether the RA product of the contact depends on the depletion width in Si.

2.4.1 FM/I/Si contact to lightly-doped Si

Figure 2.5 (a) shows the I - V characteristics of FM/I/Si contacts with low-doped n -type Si ($n_d \sim 10^{21} \text{ m}^{-3}$) and various thickness of the Al_2O_3 barrier. The oxidation time for the tunnel barrier was 7.5 min. These I - V curves show rectifying characteristics. In the reverse bias range ($V > 0$), the current density is very small, having only a slight dependence on the voltage. In the forward bias range ($V < 0$), two different slopes are observed. At the lower voltage, the current increases exponentially due to the thermionic emission. At the higher voltage, tunneling through the Al_2O_3 barrier limits the current, and the slope is determined by the tunnel barrier. The current decreases as the thickness of the Al_2O_3 barrier is increased.

We have examined the well-known method for RA product control, used in metal magnetic tunnel junctions, namely, adjusting the tunnel barrier thickness. Figure 2.5 (b) shows the effect of the thickness of the tunnel barrier on the RA product of the FM/I/Si contact. The contact resistance in the reverse bias range (open symbols) remains constant when the thickness of the tunnel barrier is varied, since the depletion region in the silicon is very thick, about 1000 nm, and the resistance of the tunnel barrier is small in comparison with that of the depletion region. From this result, we find that the Schottky barrier plays a dominant role in the reverse bias range. Consequently, the RA value in the reverse bias is very high, $10^2 \Omega\text{m}^2$ which is about 9 orders of magnitude higher than the value needed for the efficient spin injection as shown in Fig. 2.6.

The RA product of the contact in the forward bias are taken at the relatively high voltage, 0.72 V at which the effect of the tunnel barrier is visible. As the thickness of the barrier increases, the RA product of the contact increases exponentially, since the tunnel transmission is exponentially dependent on the thickness of barrier[51]. With the same oxide thickness, the resistance also increases as the oxidation time increases. Under- and over-oxidation would be a possible explanation for these results. In the forward bias range, the RA product of the contact can be tuned over a range of three-orders of magnitude by varying the thickness and the plasma oxidation time. While the RA values in forward bias are smaller than those in reverse bias, they are above $10^{-5} \Omega\text{m}^2$, which is still too high for the efficient spin detection.

In summary, the RA product of tunnel contacts with a Co or $\text{Ni}_{80}\text{Fe}_{20}$ elec-

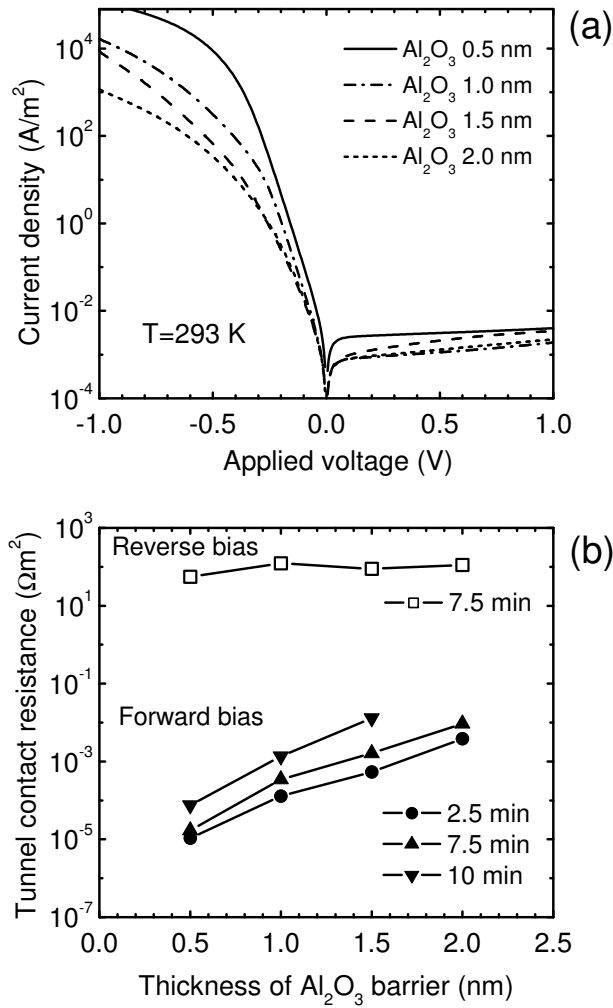


Figure 2.5. (a) I - V characteristics of Co- Al_2O_3 -Si contacts with different aluminum oxide thicknesses and low-doped Si ($T = 293$ K). The minus voltage is the forward bias, and the positive voltage is the reverse bias. The oxidation time of the tunnel barrier was 7.5 min. (b) The interface resistance-area (RA) product vs. the thickness of the Al_2O_3 tunnel barrier. The oxidation time is varied from 2.5 min to 10 min. The data for the reverse bias are taken at 0.12 V, and the data for the forward bias are taken at -0.72 V.

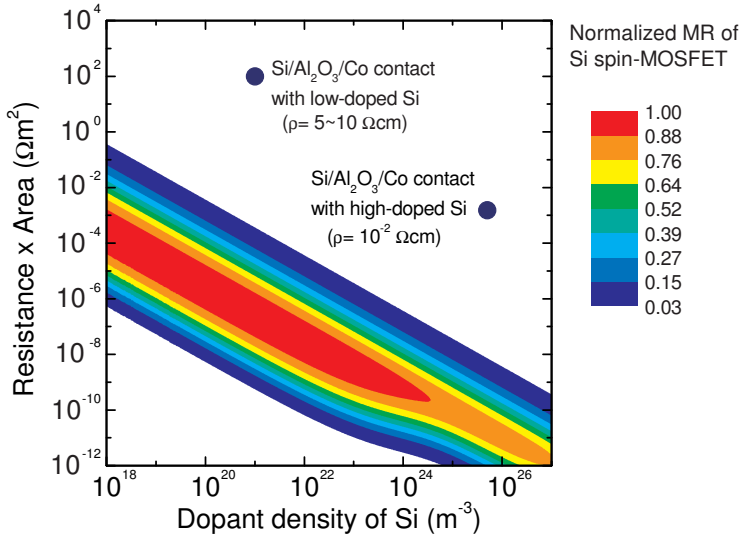


Figure 2.6. Calculated MR of FM/I/Si/I/FM spin-MOSFET structure as a function of the contact resistance-area product and the Si dopant density. The colour legend shows the value of normalized MR. Two solid symbols represent experimental results for Si/Al₂O₃ (1 nm)/Co (15 nm) contacts with two different dopant densities.

trode on low-doped Si ($\rho = 5\sim 10 \Omega\text{cm}$; $n_d = 10^{21} \text{ m}^{-3}$) varies little as the thickness of the Al₂O₃ tunnel barrier is varied. This is because the Schottky barrier dominates the resistance of the contacts rather than the tunnel barrier. The resulting RA product at the spin injection condition (+0.2 V) is about eight to nine orders of magnitude higher than the value needed for efficient spin injection; The resulting RA product at the spin detection condition is also two to four orders of magnitude higher than the value needed for efficient spin detection. With this type of contact, any significant MR cannot be expected.

2.4.2 FM/I/Si contact to heavily-doped Si

One method to decrease the RA product is to reduce the depletion width in Si using heavily-doped Si. We have fabricated Si/Al₂O₃/Co contacts on heavily-doped Si ($\rho = 10^{-2} \Omega \text{ cm}$; $n_d = \sim 5 \times 10^{26} \text{ m}^{-3}$), and measured the I - V characteristics of FM/I/Si contacts, as shown in Fig. 2.7. The oxidation time for the Al₂O₃ barrier was 7.5 min. The depletion region in Si with this doping

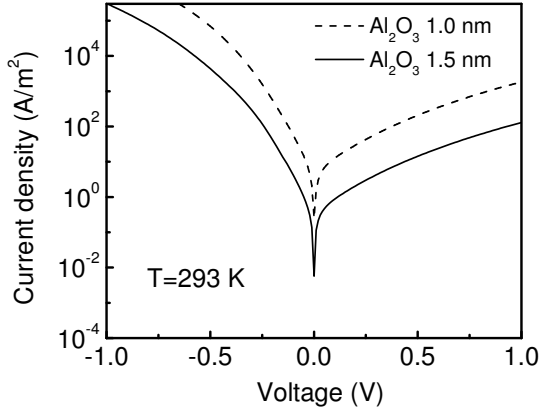


Figure 2.7. *I-V* characteristics of FM/I/Si contacts on heavily-doped Si with $n_d \approx 5 \times 10^{26} \text{ m}^{-3}$ at $T = 293 \text{ K}$. The broken line is for the FM/I/Si contacts with a 1.0-nm Al_2O_3 barrier, and the solid line is for the FM/I/Si contacts with a 1.5-nm Al_2O_3 barrier. The oxidation time for the Al_2O_3 barrier was 7.5 min. The bias polarity is the same as in Fig. 2.5.

concentration is relatively narrow, about 5 nm. As a result, we observe that the *I-V* characteristics are much less rectifying, and the Al_2O_3 tunnel barrier affects the electronic transport in both forward and reverse bias. The *RA* product of the FM/I/Si contact with a 1.0 nm barrier at 0.12 V and -0.72 V are $7.8 \times 10^{-3} \Omega\text{m}^2$ and $2.3 \times 10^{-6} \Omega\text{m}^2$ respectively.

This *RA* product is four orders of magnitude lower than that with the low-doped Si, but the optimum value of the *RA* product has also moved towards smaller values, as shown Fig. 2.6. Therefore, the *RA* product of contacts with heavily-doped Si is still far too high for efficient MR observation. Moreover, the high doping concentration deteriorates the spin-conserved transport in the semiconductor, because the spin diffusion length is proportional to $n^{-0.5}$ [27], and the spin lifetime may be decreased as the doping concentration is increased[35]. We thus find that using a heavily-doped Si channel is not a solution.

From these results, we conclude that the observation of MR in a Si spin-MOSFET is not possible with standard FM contacts and the conventional method to control the tunnel conductance, explaining the absence of positive results for Si in literature.

2.5 FM/I/Si contacts with low-work-function ferromagnets (Gd)

The main objective of this section is to develop effective methods to control the Schottky barrier height of the metal-insulator-semiconductor (MIS) contacts to Si. In the previous section, it has been pointed out that a high Schottky barrier height of MIS contacts is one of the major obstacles to realize a Si-based spin transistor based on electrical spin injection and detection in Si. We are especially interested in a low Schottky barrier height of a MIS contact for this application. In order to solve the issue discussed in previous section, we present an alternative approach to control the RA product of a spin tunnel contact by reducing the Schottky barrier.

2.5.1 Schottky barrier height of FM/I/Si contact

The Schottky barrier height (Φ_B) of a FM/I/Si contact is determined by various parameters, such as the work function of metal (Φ_m), the electron affinity of Si (χ), the thickness (δ) and dielectric constant (ϵ_i) of an insulator, the charge neutrality level ($q\phi_{cnl}$), and the surface density of gap states (D_s) at the Si surface[44, 45]. Using a simplified model taken into account the presence of the surface state, one can calculate the Schottky barrier height as explained in ref [45]. Introducing the quantities[45],

$$a \equiv \frac{\epsilon_i}{\epsilon_i + q^2\delta D_s} \quad (2.1)$$

$$b \equiv -a\chi + (1 - a)\left(\frac{E_g}{q} - \phi_{cnl}\right) - \Delta\phi \quad (2.2)$$

where q is the carrier charge, E_g is the energy band gap of Si, and $\Delta\phi$ is the image force barrier lowering, one can express the Schottky barrier of the contact in a very simple form as

$$\Phi_B = a\Phi_m + b. \quad (2.3)$$

During the fabrication process, the plasma oxidation might lead to some oxidation of Si. It is useful to consider the case that the insulator comprises two dielectric layers. The quantity a should be modified to include the dielectric

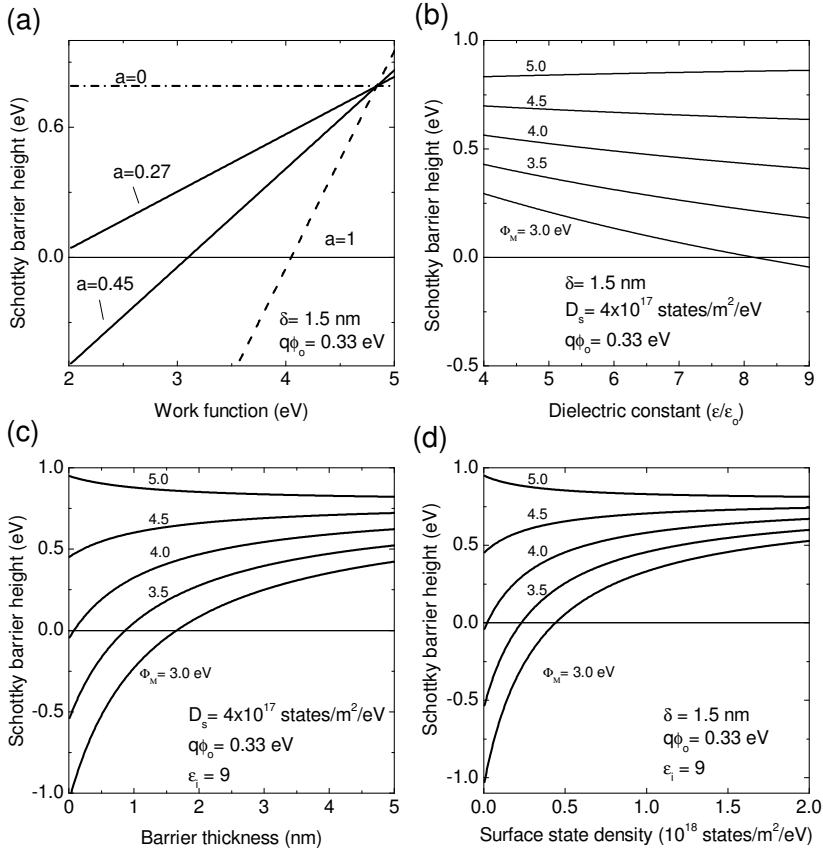


Figure 2.8. Schottky barrier height versus various parameters. (a) metal work function, (b) the thickness and (c) the dielectric constant of the tunnel barrier or insulator, and (d) the density of surface states at the Si surface. The parameters indicated are described in the text.

parameters of both layers.

$$a \equiv \frac{\epsilon_{1i}\epsilon_{2i}}{\epsilon_{1i}\epsilon_{2i} + q^2 D_s (\epsilon_{1i}\delta_2 + \epsilon_{2i}\delta_1)}. \quad (2.4)$$

where ϵ_{1i} , δ_1 , ϵ_{2i} , and δ_2 are the dielectric constants and the thicknesses of the two dielectric layers respectively.

Fig. 2.8 represents how the Schottky barrier depends on the various parameters, such as the work function of metal, the thickness and dielectric constant of the insulator, and the density of surface states at the Si surface. If the density of surface states at the Si surface is very high, then the Fermi energy

level at the interface is pinned by the surface states at the value $q\phi_{cni}$ above the valence band maximum[45]. Then the Schottky barrier height becomes independent of the metal work function as that in the compound semiconductor like GaAs[52]. If there is no surface state, the Schottky barrier height is directly dependent on the metal work function and the electron affinity of Si. In a real FM/I/Si contact, the value of a lies in between 0 and 1. Consequently, the Schottky barrier in a FM/I/Si contact can be controlled by changing the work function of the material. The quantity a becomes larger if the insulator is thinner, the dielectric constant is higher, and the surface density of gap states is lower at the Si surface.

Unlike GaAs of which Schottky barrier height is relatively insensitive to the used metal[52], the Schottky barrier height (Φ_B) to Si is subjected to change with the work function of metal(Φ_m)[45]. The Schottky barrier height of a FM/I/Si contact can therefore be reduced using a material with a work function lower than that of Co ($\Phi_m = 5.0$ eV), Ni (5.15 eV), or Fe (4.5 eV)[54–57], while the material should still be ferromagnetic in order to supply spin-polarized electrons. In the next section, we demonstrate this approach using Gd, a ferromagnetic material with reasonably low work function ($\Phi_m = 3.1$ V)[55] and the highest TSP (13.3%) among rare earth materials as shown in previous tunnel spin polarization measurements with $\text{Al}_2\text{O}_3/\text{Gd}$ structures[58].

2.5.2 Fabrication of contacts with Gd

Figure 2.9 depicts the layer stack of a Si/ Al_2O_3 / Gd/ Cap contact with thick Gd layer, and the layer stack of a Si/ Al_2O_3 / Gd/ $\text{Ni}_{80}\text{Fe}_{20}$ / Cap contact with sub-nm Gd interlayer. The experimental procedure is the same as the FM/I/Si contact with conventional ferromagnetic materials as described in section 2.3 except for the Gd layer deposition. Gd metal (99.99%, Stanford Materials Corp.) prepared by distillation was used as a source for the e-beam evaporation. The Gd are deposited by e-beam evaporation at a base pressure of 10^{-10} mbar. In order to prevent an oxidation of Gd, an Al/ Au layer or NiFe/ Au layer was used a capping layer.

First, we have fabricated a series of Si/ Al_2O_3 / Gd (15 nm)/ Cap contacts with different Al_2O_3 thicknesses to study the effect of the thick Gd layer on the Schottky barrier height. Thereafter, we have fabricated a series of Si/

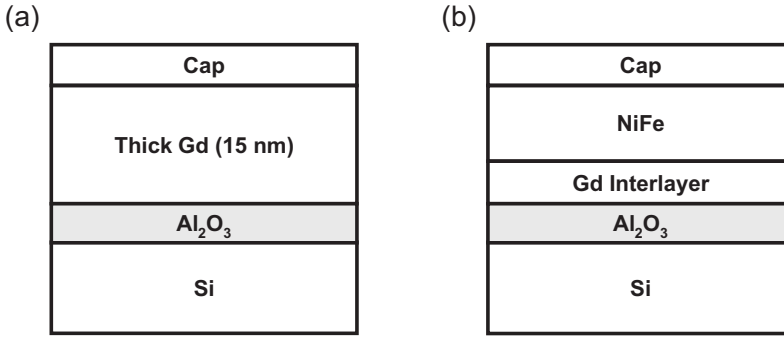


Figure 2.9. (a) The layer stack of a Si/ Al₂O₃/ Gd/ Cap with thick Gd layer. (b) The layer stack of a Si/ Al₂O₃/ Gd (x nm)/ Ni₈₀Fe₂₀ (10 nm)/ Cap with sub-nm Gd layer.

Al₂O₃/ Gd (x nm)/ Ni₈₀Fe₂₀ (10 nm)/Cap contacts with a sub-nm Gd interlayer to control the RA product of the contact.

2.5.3 Schottky barrier removal with low work-function ferromagnet

Figure 2.10 shows the I - V characteristics of a Si/ Al₂O₃ (0.5 nm)/ Ni₈₀Fe₂₀ and a Si/ Al₂O₃ (0.5 nm)/ Gd tunnel contact on low-doped Si ($\rho = 5\sim 10$ Ωcm ; $n_d = 10^{21}$ m^{-3}). The oxidation time for the Al₂O₃ barrier was 7.5 min. The current density of the Si/ Al₂O₃/ Ni₈₀Fe₂₀ contact is very small in the reverse bias range ($V > 0$, spin injection condition), having only a slight dependence on the voltage. By contrast, the current density of the Si/ Al₂O₃/ Gd tunnel contact in the reverse bias range is increased by almost eight orders of magnitude compared to the result with Si/ Al₂O₃/ Ni₈₀Fe₂₀. The current density of the Si/ Al₂O₃/ Gd tunnel contact in the forward bias range ($V < 0$, spin detection condition) is also increased significantly. As a consequence, the I - V curves of contacts with Gd show symmetric behavior, which is useful to obtain the same RA product of the source and the drain contacts.

The RA product of the Si/ Al₂O₃/ Gd contact at ± 0.2 V is 10^{-7} Ωm^2 , which reaches the optimum range in Fig. 2.6 for both spin injection and detection contacts. The RA product of the contact with a Gd layer shows an exponential dependence on the barrier thickness (Fig. 2.11), implying that the thermionic emission is no longer the dominant transport mechanism but the

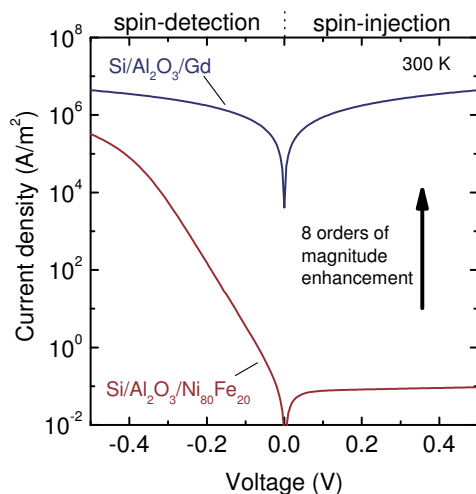


Figure 2.10. Absolute value of current density versus bias voltage of Si/Al₂O₃ (0.5 nm)/Ni₈₀Fe₂₀ (15 nm) and Si/Al₂O₃ (0.5 nm)/Gd (15 nm) contacts. The oxidation time for the Al₂O₃ barrier was 7.5 min. The minus voltage is the forward bias (the spin detection condition); the positive voltage is the reverse bias (the spin injection condition).

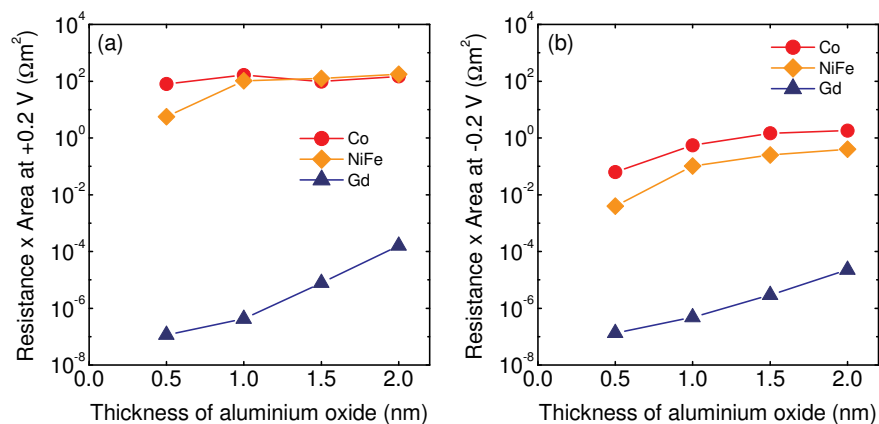


Figure 2.11. Resistance-area product of the tunnel contact versus the thickness of the Al₂O₃ tunnel barrier (a) at the reverse bias of +0.2 V and (b) at the forward bias of -0.2 V. The red (or orange) data is for a Si/Al₂O₃/Co (or Ni₈₀Fe₂₀) (15 nm) contacts; the blue data is for the Si/Al₂O₃/Gd (15 nm) contacts. The oxidation time for the Al₂O₃ barrier was 7.5 min.

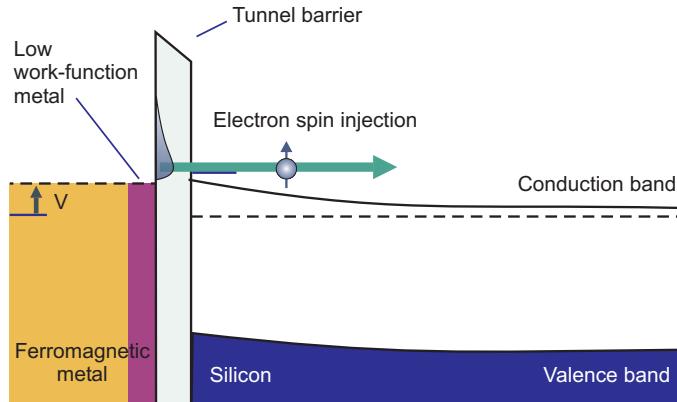


Figure 2.12. Schematic energy band diagram of the electrical spin injection (reverse bias) in a FM/I/Si junction with interfacial low-work-function metal layer. Φ_B is the Schottky barrier height, and V is the bias voltage. The broken lines depict the Fermi energy.

tunnel transport across the Al_2O_3 barrier is important. We therefore concluded that the Schottky barrier is removed by low work-function metal.

2.5.4 RA product of NiFe/Gd/I/Si contacts

Besides a low RA product, the ability to *tune* the RA product is essential, since the RA product of the tunnel contact should be in a specific range (Fig. 2.6) that also depends on the τ_s in Si, which is not accurately known. To tune the tunnel contact resistance, we exploit the fact that the work function is determined by the outermost surface layers of a material. We thus control the RA product by inserting an ultrathin Gd layer between a conventional FM electrode and the Al_2O_3 barrier, as depicted in Fig. 2.12 for FM/I/Si tunnel contacts consisting of Si/ Al_2O_3 (0.5 nm) / Gd (0 to 5 nm) / $\text{Ni}_{80}\text{Fe}_{20}$ (10 nm) / Au (10 nm). The oxidation time for the Al_2O_3 barrier was 7.5 min. As shown in Fig. 2.13, the current density of these tunnel contacts in the reverse bias range is dramatically enhanced by inserting a sub-nanometer Gd interlayer. The I - V curves of these contacts show rectification that gradually disappears as the Gd thickness is increased, while the rectifying behavior is absent for thicker Gd interlayer (0.8 to 5.0 nm).

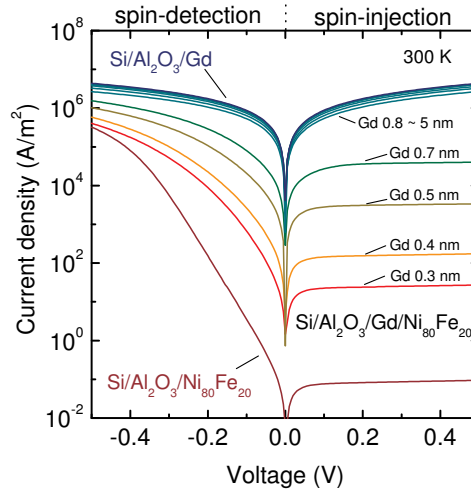


Figure 2.13. Absolute value of current density versus bias voltage of Si/ Al₂O₃ (0.5 nm)/ Ni₈₀Fe₂₀ (15 nm), Si/ Al₂O₃ (0.5 nm)/ Gd (15 nm) as well as Si/ Al₂O₃ (0.5 nm)/ Gd (0.3 to 5 nm)/ Ni₈₀Fe₂₀ contacts with an interfacial nanolayer of low work-function Gd. The oxidation time for the Al₂O₃ barrier was 7.5 min. The minus voltage is the forward bias (the spin detection condition); the positive voltage is the reverse bias (the spin injection condition).

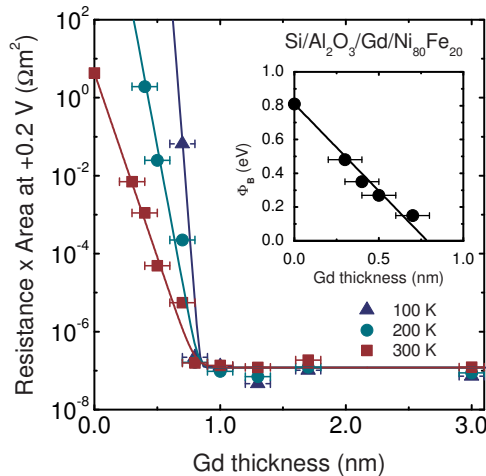


Figure 2.14. Resistance-area product of the Si/ Al₂O₃ (0.5 nm)/ Gd/ Ni₈₀Fe₂₀ (10 nm) contacts at a reverse bias of +0.2 V versus the thickness of the Gd interlayer at three different temperatures. The solid lines are a guide to the eyes. The inset shows the Schottky barrier height (Φ_B) of the contact versus the thickness of the Gd interlayer. The error bars denote the accuracy of the determination of the Gd thickness.

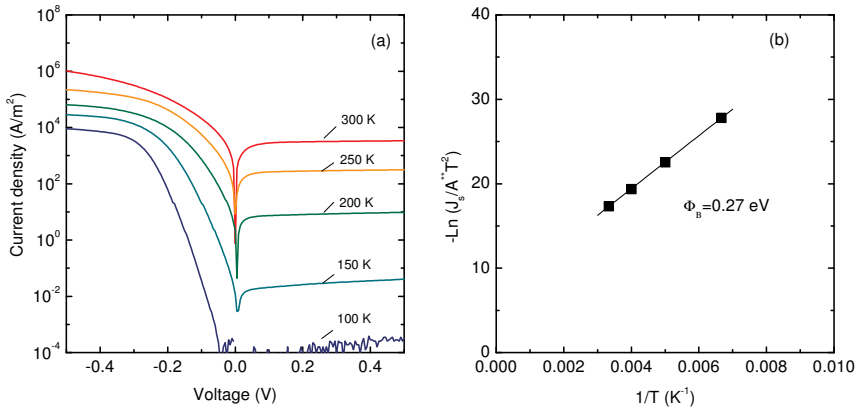


Figure 2.15. (a) The temperature dependence of the I - V curves of Si/ Al₂O₃ (0.5 nm)/ Gd (0.5 nm)/ Ni₈₀Fe₂₀ (10 nm)/ Au (10 nm) contact. The oxidation time for the Al₂O₃ barrier was 7.5 min. (b) $J_s/(A^{**}T^2)$ versus reciprocal of temperature, where J_s is the saturation current density in the reverse bias range, A^{**} is the Richardson coefficient, and T is temperature[45]. A linear fit is used to determine the Schottky barrier height of the MIS contact.

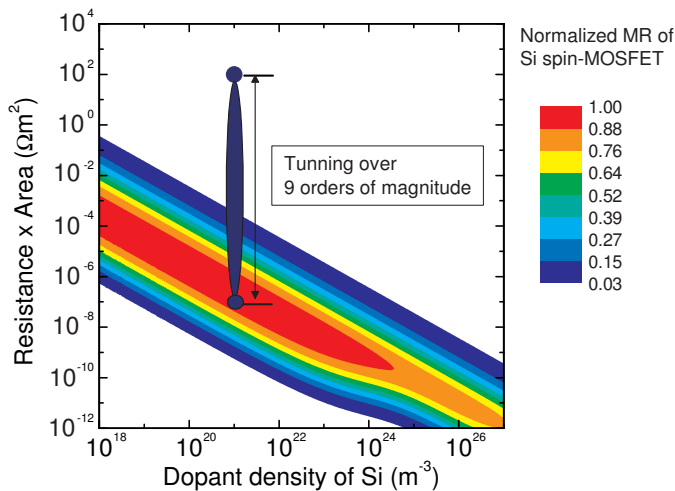


Figure 2.16. Calculated MR of FM/I/Si/I/FM spin-MOSFET structure as a function of the contact resistance-area product and the Si dopant density. The colour legend shows the value of normalized MR. Blue area shows the range over which the RA product of the MIS contact can be tuned using a low work-function ferromagnet interlayer.

As shown in Fig. 2.14, the RA product of the tunnel contacts decreases abruptly by increasing the thickness of the Gd interlayer in the sub-nanometer regime, and saturates to the RA product of the FM/I/Si contact with a thick (15 nm) Gd film. For a 1 nm Gd interlayer, the RA product for the spin injection condition ($V = +0.2$ V) is reduced by about eight orders of magnitude. Similar behaviour occurs for the RA product in the negative bias range, the spin detection condition. When the thickness of the Gd layer is more than about 1 nm, the RA product of the contact saturates at a constant value. Since the work function is very sensitive to the outermost surface layers of a material, the surface coverage of the Gd must be complete for 1 nm of Gd. Generally, lowering the temperature makes the RA product of a Schottky contact higher, as thermal emission across the Schottky barrier is rapidly suppressed. This temperature dependence still remains for the tunnel contacts with a thinner (< 0.7 nm) Gd interlayer, but it disappears for the tunnel contacts with a thicker (> 1.0 nm) Gd interlayer, for which the Schottky barrier is removed. The inset of Fig. 2.14 shows the Schottky barrier height of MIS contacts as a function of Gd thickness. The Schottky barrier heights has been calculated from the temperature dependence of the I - V curves[44, 45], as shown in Fig. 2.15. The Schottky barrier height is 0.81 eV for a tunnel contact without the Gd interlayer; it decreases by increasing the Gd thickness; for a 1 nm Gd interlayer, the Schottky barrier vanishes. Thus, by adjusting the Gd thickness, we can control the Schottky barrier height and thereby tune the RA product over eight orders of magnitude (Fig. 2.16).

2.5.5 Work function engineering with a Gd interlayer

We have found, in the previous section, the Schottky barrier height of Si/Al₂O₃ / Gd (x nm)/ Ni₈₀Fe₂₀ contacts has been tuned by the insertion of a low work-function interlayer in between a metal and an insulator of MIS contacts; the Schottky barrier height of the contacts is almost linearly proportional to the Gd thickness up to 0.8 nm as shown in Fig. 2.14.

According to Eq. 2.3, the Schottky barrier height has also a linear relation with the work function of the metal. This implies that it is possible to control the effective work function of the Gd (x nm)/ Ni₈₀Fe₂₀ (10 nm) bi-layer by changing the Gd thickness. If the Gd thickness is zero, the work function of Ni₈₀Fe₂₀ determines the Schottky barrier height. The work function of

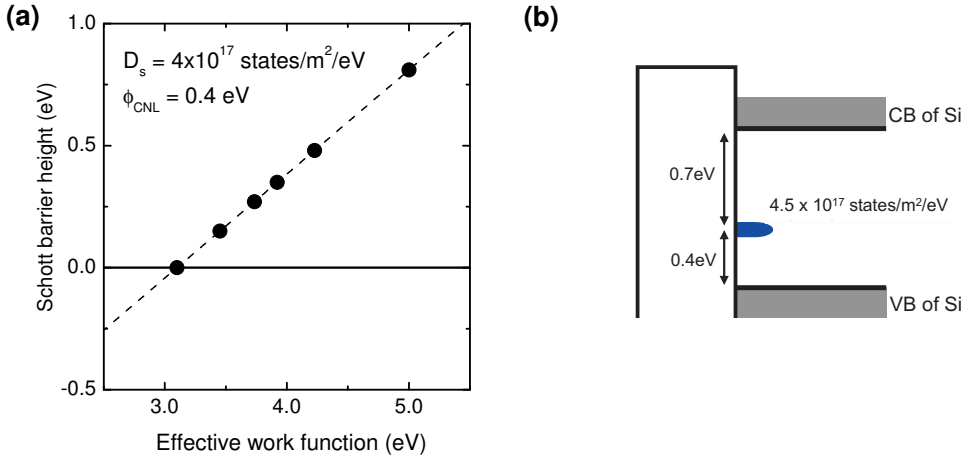


Figure 2.17. The Schottky barrier height of Si/ Al_2O_3 (2.0 nm)/ Gd (0~3 nm)/ $\text{Ni}_{80}\text{Fe}_{20}$ (10 nm) /Au (10 nm) tunnel contacts as a function of the effective work function of the metal layer as determined by the Gd thickness. The dashed line is the linear fit using Eq. 2.3 to determine the density of gap states and the position of the charge neutrality level. (b) Schematic energy band diagram of a MIS contact with n-type Si. The charge neutrality level is depicted.

$\text{Ni}_{80}\text{Fe}_{20}$ is estimated as 5.0 eV from the weighted average of the work functions of individual components, Ni and Fe[59]. If the Gd thickness is thicker than 0.8 nm, the work function of the bilayer saturates to the work function of bulk Gd, 3.1 eV. From these two extreme cases, we can obtain the coefficients, a and b in Eq. 2.1 and Eq. 2.2: $a = 0.426$ and $b = -1.321$. Fig. 2.17(a) shows the linear line with obtained a and b values as well as the measured Schottky barrier height of the Si/ Al_2O_3 / Gd (x nm)/ $\text{Ni}_{80}\text{Fe}_{20}$ contacts on this line. Comparing this result with the Eq. 2.1 and Eq. 2.2, we can obtain the surface density of gap states (D_s) and the charge neutrality level (ϕ_{cnl}): $D_s = 4.5 \times 10^{17} \text{ states/m}^2/\text{eV}$ and $\phi_{\text{cnl}} = 0.41 \text{ eV}$. Fig. 2.17(b) shows the schematic energy diagram of the contact where the charge neutrality level located at $\sim 0.4 \text{ eV}$ above the valence band maximum. In this calculation, we used the dielectric constant of bulk Al_2O_3 ($\epsilon = 9$), and thickness of the insulator determined from the TEM experiment ($\delta = 1.5 \text{ nm}$), neglecting the image-force-induced lowering of the Schottky barrier.

Using Eq. 2.3 and Fig. 2.17(a), we can obtain the effective work function of the Gd (x nm)/ $\text{Ni}_{80}\text{Fe}_{20}$ (10 nm) bi-layer from the measured Schottky barrier height (Fig. 2.14). From this results we find a linear relationship between

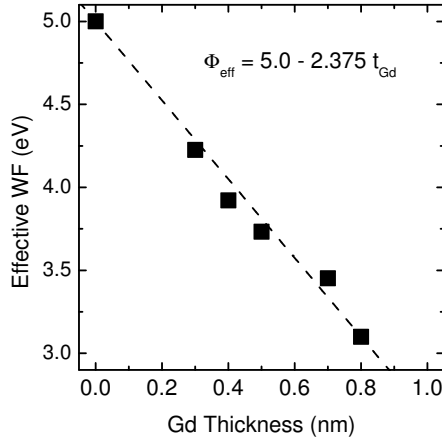


Figure 2.18. The effective work function (Φ_{eff}) of Gd (x nm)/ Ni₈₀Fe₂₀ (10 nm) bi-layer versus the thickness of the Gd interlayer (t_{Gd}). The dash line shows a linear relation between the Φ_{eff} and t_{Gd} .

the effective work function and Gd thickness as shown in Fig. 2.18.

$$\Phi_{eff} = 5.0 - 2.375 \times t_{Gd} \text{ (eV)} \quad (2.5)$$

This relation will be used in chapter 4 to investigate the charge neutrality level and the surface density of the gap states of the tunnel contacts with Cs-coated Si surface.

2.5.6 Structural and chemical properties of NiFe/Gd/I/Si contacts

Because rare earth metals are known to get oxidized very fast even at room temperature, we have conducted chemical analysis of a thick Gd film (40 nm) with Al capping layer (30 nm) deposited on a Si substrate. As shown in Fig. 2.19, depth profile x-ray photoelectron spectroscopy (XPS) showed that the oxygen content in the Gd film is negligible. The XPS peak remained at the energy for metallic Gd, assuring that the deposited films were purely metallic Gd without significant oxygen uptake from the background gas in the chamber.

Since this does not preclude any possible oxidation of the Gd in the immediate contact with the Al₂O₃ barrier, we have fabricated Si/ Al₂O₃/ FM contacts with an intentionally oxidized Gd layer. The Gd layer of a series of

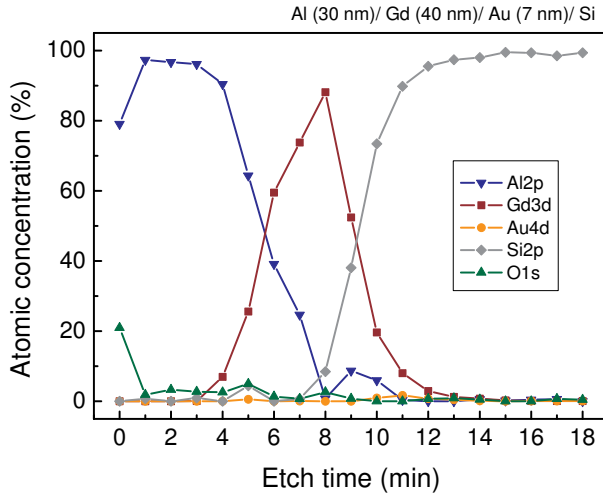


Figure 2.19. Atomic concentration versus etch time in depth profile x-ray photoelectron spectroscopy (XPS).

Si/ Al₂O₃/ Gd/ Ni₈₀Fe₂₀ contacts was oxidized by an extra natural oxidation step in O₂ pressure of 100 Torr for 1 hour at room temperature, before deposition of the Ni₈₀Fe₂₀ top electrode. The I - V characteristics of Si/ Al₂O₃/ Gd/ Ni₈₀Fe₂₀ contacts with an as-grown Gd layer is compared with those with the intentionally oxidized Gd layer in Fig. 2.20. The current density of the latter contacts was reduced 2~6 orders of magnitude compared to junctions without intentional Gd oxidation, while also the rectification increases. This implies that the removal of the Schottky barrier is not effective for the oxidized Gd. This investigation ruled out a significant oxidation of the Gd layer due to contact with the Al₂O₃ barrier for the results presented in previous sections.

We have investigated the structural properties of FM/Gd/I/Si contacts using a normal TEM and an energy-filtered TEM. The energy-filtered image is based on the electron energy-loss-spectra specific to elements[60]. By comparing the energy-filtered TEM images adjacent to the energy-loss peak of an element, one can obtain an element map of the selected element with a high spatial resolution.

Figure 2.21 shows a cross sectional transmission electron microscopy image of Si/ Al₂O₃ (1.5 nm)/ Gd (2 nm)/ Ni₈₀Fe₂₀ (10 nm)/ Au (10 nm) contact on low-doped n -type Si substrates (resistivity, $\rho = 5\sim 10 \Omega\text{cm}$; dopant density, $n_d = 10^{21} \text{ m}^{-3}$). The oxidation time for the Al₂O₃ barrier was 7.5

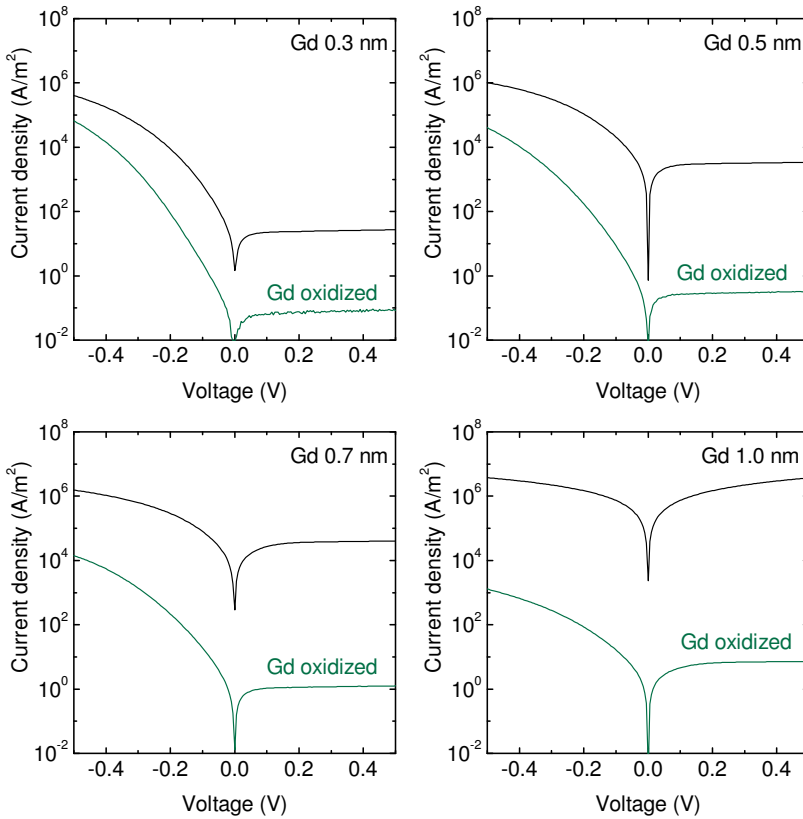


Figure 2.20. Absolute value of current density versus bias voltage of Si/ Al_2O_3 (0.5 nm)/ Gd (0.3, 0.5, 0.7, and 1 nm)/ $\text{Ni}_{80}\text{Fe}_{20}$ (10 nm) contacts. Black lines are for the contacts with the un-oxidized Gd layer. Green lines are for the contacts with the Gd layer intentionally oxidized in 100 Torr oxygen for 1 hour. The minus voltage is the forward bias (the spin detection condition); the positive voltage is the reverse bias (the spin injection condition).

min. The interfaces between different materials are clear, and each layer in this TEM image is smooth, showing minimum thickness variation. Fig. 2.22 shows a cross-sectional TEM image of the contact with a higher spatial resolution. It appears that the deposited Gd layer is amorphous, while the $\text{Ni}_{80}\text{Fe}_{20}$ and Au layers are polycrystalline.

Figure 2.23 shows elemental images of Gd, oxygen, and Ni respectively. The white intensity on the energy-filtered images indicates the presence of the elements at the location. Those energy-filtered TEM images are juxtaposed to a normal TEM image for comparison. Figure 2.23 contains all three images

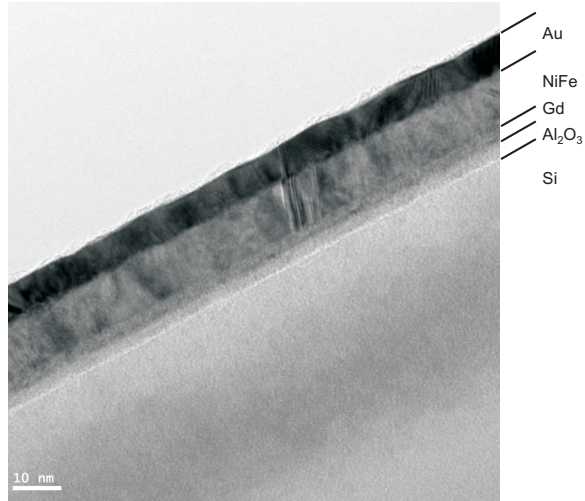


Figure 2.21. Cross-sectional TEM image of Si/ Al₂O₃/ Gd/ Ni₈₀Fe₂₀ contacts.

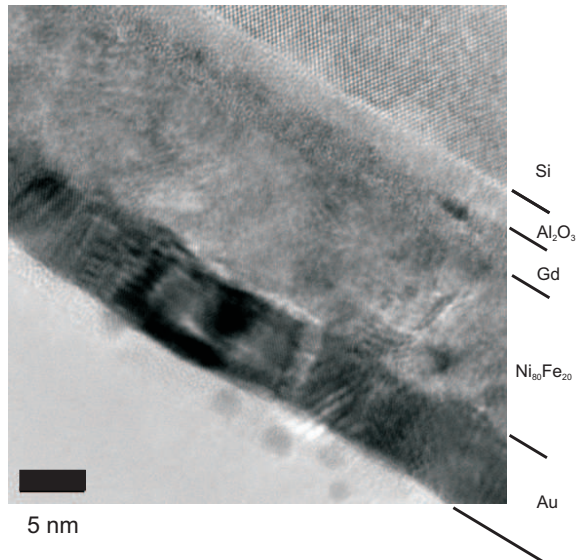


Figure 2.22. Cross-sectional TEM image of Si/ Al₂O₃/ Gd/ Ni₈₀Fe₂₀ contacts with a high spatial resolution.

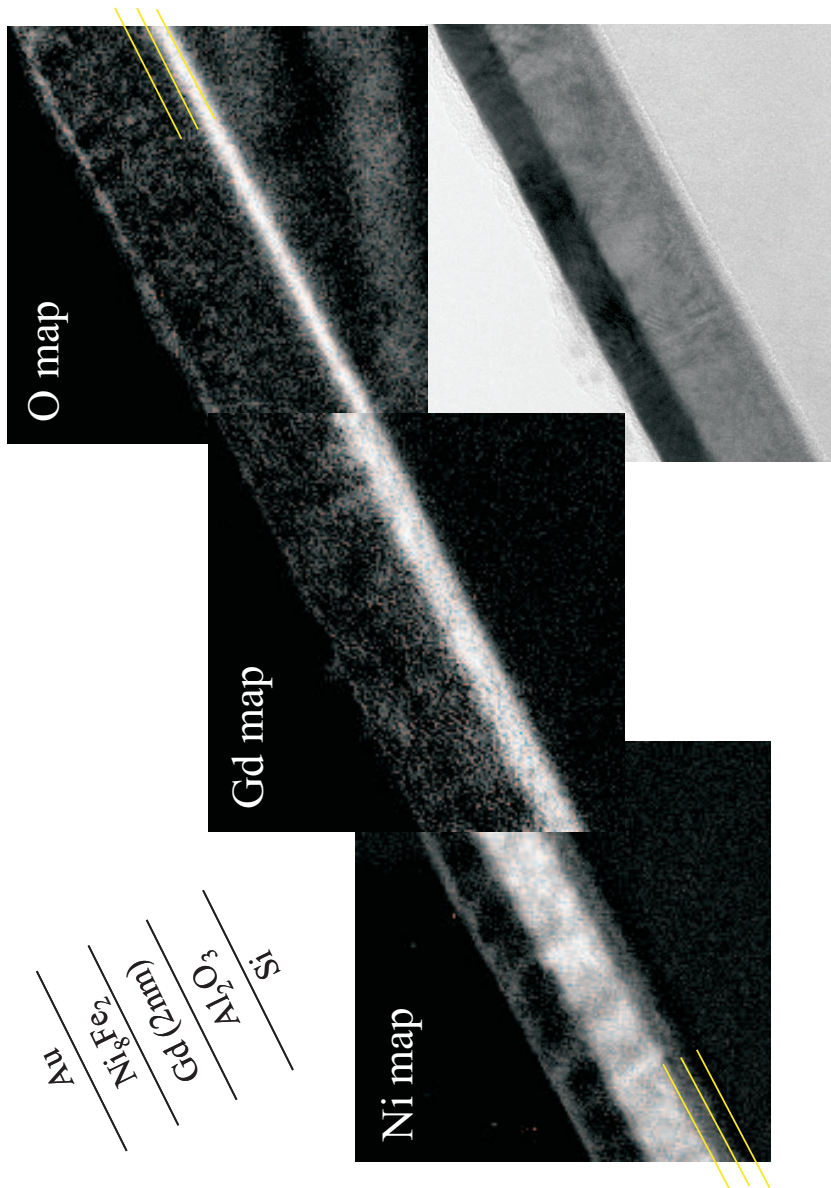


Figure 2.23. The element-specific TEM images of Si/Al₂O₃/Gd/Ni₈₀Fe₂₀ contacts for Gd, Ni₈₀Fe₂₀, and oxygen. A normal TEM image is shown for the comparison.

put side by side for an overview. Those images provides crucial information to understand inter-diffusion among elements in the MIS contacts. The thickness of a white band in the Gd image (Fig. 2.23) is much thicker than that of the deposited Gd layer; and the thickness of the white band rather corresponds to the sum of thickness of Gd and Al_2O_3 layers. It seems that some amount of Gd diffuses into the Al_2O_3 barrier, while the diffusion of Gd into the $\text{Ni}_{80}\text{Fe}_{20}$ is negligible. The consequence of the Gd diffusion into the tunnel barrier will be discussed in chapter 4. The oxygen image (Fig. 2.23) is very useful to check whether the oxygen stays inside of the barrier or diffuses into the Gd layer. The oxygen image clearly shows that the diffusion of oxygen into the Gd layer is negligible. It seems that the diffusion of Gd into oxide barrier is energetically favorable while the diffusion of oxygen into Gd layer is difficult. This result again confirms that the Gd layer does not take oxygen from a tunnel barrier; and the Gd layer on the barrier is purely metallic. This pure metallic layer makes it possible to do a work function engineering in the previous section. The Ni image (Fig. 2.23) suggests that small amount of the Ni diffuses into Gd layer as indicated by the gray contrast for Ni on the location of the Gd layer. The diffusion of Ni into Gd results in alloying of Gd with Ni, which might affect the magnetic behavior of the tunnel contact, such as magnetic ordering temperature. This issue will be addressed in chapter 3.

2.6 Conclusions

In this chapter, the properties of FM/I/Si contacts has been studied for the application of the source and drain electrodes of the Si spin-MOSFET structure. A series of high-quality FM/I/Si contacts has been fabricated with standard ferromagnetic materials, such as Co and $\text{Ni}_{80}\text{Fe}_{20}$ alloy. It turns out that the RA product of these contacts are many orders of magnitude higher than the optimum values for the MR observation in a Si spin-MOSFET structure, because the Schottky barrier formation in the FM/I/Si contacts gives rise to the major obstacle to the MR observation: namely, (i) low current due to a (reverse biased) Schottky barrier, (ii) electrons tunnel into or out of states at elevated energy, for which the TSP is strongly reduced, and (iii) a huge conductivity mismatch of many orders of magnitude between Si and tunnel contacts with ferromagnetic metals such as Co and NiFe alloys. From these results, we conclude that the observation of MR in a Si spin-MOSFET is not

possible with standard FM contacts and the conventional method of adjusting the tunnel barrier thickness to control the tunnel conductance.

We have presented a breakthrough to this problem by introducing a low work-function ferromagnet inserted at the FM/tunnel barrier interface. It has been shown that the Schottky barrier is completely removed by using a thick Gd electrode, the resistance-area (RA) product of FM/ Al_2O_3 /Si contacts is reduced by eight orders of magnitude, and the optimum RA product for the MR observation in spin-MOSFET structure is obtained. Besides a low RA product, the ability to *tune* the RA product is essential, since the RA product of the tunnel contact should be in an optimum range that also depends on the spin life-time in Si, which is not accurately known. The tuning of Schottky barrier height has been demonstrated using a sub-nm low-work-function Gd interlayer, based on the idea that the work function of the electrode is determined by the outermost layers. We find that the Gd thickness needed to completely remove the Schottky barrier is only 0.8 nm. In this way the resistance-area (RA) product of FM/ Al_2O_3 /Si contacts can be tuned over eight orders of magnitude, and the optimum RA product for the MR observation in spin-MOSFET structure can be achieved.

The work-function engineering of the spin-tunnel contact is a very useful tool to reduce the Schottky barrier of Si/ Al_2O_3 / Gd/ $Ni_{80}Fe_{20}$ contacts. We find that the effective work function of Gd/ $Ni_{80}Fe_{20}$ bi-layer of the contact is linearly proportional to the Gd interlayer thickness up to 0.8 nm. By varying the effective work function of the metal, we have obtained the surface density of gap states (D_s) and the charge neutrality level (ϕ_{CNL}) at the Si/ Al_2O_3 interface of the contact.

Structural analysis of Si/ Al_2O_3 / Gd/ $Ni_{80}Fe_{20}$ contacts shows that the deposited Gd layer is amorphous with relatively uniform thickness. The chemical and electrical analyses indicate that the oxidation of the deposited Gd layer is negligible in the contact. Using the element-specific TEM images, inter-diffusions between the elements has been observed; Gd diffuses into an oxide barrier, and Ni diffuses into the Gd layer; by contrast, Gd doesn't diffuse into the NiFe layer, and oxygen doesn't diffuse in the Gd layer. This again confirms that the work-function engineering by a sub-nm Gd interlayer has been done by the metallic Gd.

In conclusion, we have developed the FM/I/Si contacts which satisfy the first requirement for the source and drain electrodes of the Si spin-MOSFET, the RA matching to a Si channel for the MR observation in the FM/I/Si/I/FM

structure. In the next chapter, it will be shown that this type of contact also satisfies the second requirement, the high tunnel spin polarization.

Chapter 3

Magnetic tunnel junctions using low work-function ferromagnet

It has been shown, in the previous chapter, that the tunable spin tunnel contact with an ultrathin low-work-function interlayer—inserted between the ferromagnet and insulator of ferromagnet (FM)/ Al_2O_3 / Si tunnel contacts—provides the optimum resistance-area (RA) product for the electrical spin injection and detection in Si. Here we examine whether the FM/ Gd/ Al_2O_3 contact shows a high tunnel-spin polarization (TSP). For this purpose, we investigate the TSP of $\text{Ni}_{80}\text{Fe}_{20}$ / Gd/ Al_2O_3 and Co/ Gd/ Al_2O_3 contacts by fabricating magnetic tunnel junctions (MTJs). This chapter describes the effect of the Gd thickness on the TSP of the contacts as well as their temperature and bias dependence. The fundamental aspects of the rare earth-transition metal (RE-TM) systems will be discussed to explain various properties of MTJs with a low work-function FM interlayer.

3.1 Introduction and motivation

We have developed spin tunnel contacts with a low work-function ferromagnet interlayer—as described in the previous chapter—which satisfy the requirement of the RA matching to the Si channel of a spin-MOSFET. The main topic of this chapter is to examine whether the spin tunnel contacts with a low work-function ferromagnet also satisfy the second requirement for the

suitable source and drain contacts of a Si-based spin MOSFET that the electron tunneling through the barrier conveys a reasonably high degree of spin polarization. This requirement is essential to realize Si-based spin MOSFETs, because the spin-polarized tunneling of electrons from a ferromagnet (FM) to Si through a tunnel barrier determines the degree of spin accumulation inside Si, and vice versa [27, 50].

The tunnel spin polarization (TSP) of an FM/barrier is a key factor to describe the degree of the spin polarization in the tunneling process[61–63]. The tunnel spin polarization is not an inherent property of the FM layer, but is related to the transport through a barrier, thereby the properties of a tunnel barrier and the interface between an FM and a tunnel barrier [62, 63]. For example, the symmetry of wave functions plays an important role in the transport in an epitaxial MgO barrier [64], resulting in a very high TSP [65, 66]; the sign of TSP is dependent on the properties of an interface like FM/SrTiO₃[67].

An MTJ consists of two magnetic layers separated by a thin insulating barrier [9, 10]. The resistance of an MTJ is a function of the relative alignment of the magnetization of the two magnetic layers. The most important figure-of-merit of the MTJ is the tunnel magnetoresistance ratio (TMR), defined as the relative resistance change in response to a magnetic field divided by the junction resistance;

$$TMR = \frac{R_{AP} - R_P}{R_P}, \quad (3.1)$$

where R_P (R_{AP}) is the resistance when the magnetization of two layer are in parallel (anti-parallel) [65, 66]. The TMR is determined by the TSP of the FM/barrier electrodes as

$$TMR = \frac{2P_1P_2}{1 - P_1P_2}, \quad (3.2)$$

where P_1 and P_2 are the TSP of the FM/barrier electrodes. This equation is the same as that of the Julliere's model[68], but it differs from the model in that the definition of TSP includes the effect of the tunnel barrier and the interface between the FM and a tunnel barrier.

A classic technique for probing the TSP of an FM/barrier, developed by Meservey and Tedrow [58], uses a superconductor electrode in a FM/ insulator/ superconductor junction. This technique requires the measurements to be conducted at a very low temperature owing to the superconductor electrode.

Recently, an alternative method has been developed to probe the TSP of an FM/barrier using a magnetic tunnel transistor (MTT), which enables us to apply the technique up to room temperature [69].

It is known that Eq. 3.2 is a valid for many $\text{FM}_1/\text{Al}_2\text{O}_3/\text{FM}_2$ junctions. If one knows the tunnel spin polarization of $\text{FM}_1/\text{Al}_2\text{O}_3$ and $\text{FM}_2/\text{Al}_2\text{O}_3$ structures, one can estimate the TMR of an MTJ consisting of the $\text{FM}_1/\text{Al}_2\text{O}_3/\text{FM}_2$ using above equation; conversely, if one knows the TSP of the $\text{FM}_1/\text{Al}_2\text{O}_3$ and measures the TMR of $\text{FM}_1/\text{Al}_2\text{O}_3/\text{FM}_2$, one can determine the TSP of the $\text{FM}_2/\text{Al}_2\text{O}_3$. As we have measured the TSP of a well-known electrode like $\text{Co}/\text{Al}_2\text{O}_3$ from separate MTT experiments, we are able to obtain the TSP of an unknown electrode using a TMR measurement. The advantage of this approach is that it allows us to measure the TSP of the unknown electrode at wide temperature range and to study its temperature dependence and bias dependence. This method will be used to verify whether the magnetic tunnel contacts with a low work-function FM interlayer satisfy the second requirement for the suitable contacts, a high TSP.

We are interested in not only the TSP of pure low work-function materials but also the TSP of bilayer systems, for example, $\text{Ni}_{80}\text{Fe}_{20}/\text{Gd}/\text{Al}_2\text{O}_3$ or $\text{Co}/\text{Gd}/\text{Al}_2\text{O}_3$ —where the low work-function material is used as sub-nm interlayer—because this structure is used to control the RA of the FM/Gd/I/Si contacts. We shall study the effect of the magnetic coupling and inter-diffusion between two layers on the TSP of the FM/Gd/ Al_2O_3 systems.

In section 3.2, we review the fundamental aspects of the rare earth metal, RE-TM alloys, and RE/TM interfaces including magnetic properties and exchange interactions. In section 3.3, we describe the fabrication of magnetic tunnel junctions using thin-film depositions and standard cleanroom techniques. In section 3.4 and 3.5, we present the TMR measurements of the MTJs, $\text{Ni}_{80}\text{Fe}_{20}/\text{Gd}/\text{Al}_2\text{O}_3/\text{Co}$ and $\text{Co}/\text{Gd}/\text{Al}_2\text{O}_3/\text{Co}$, with sub-nm Gd interlayer, and discuss various properties of the MTJs such as temperature and bias dependence. Using this result, we will examine whether the spin tunnel contacts with a low work-function FM interlayer show a reasonably high TSP.

3.2 Gd and Gd-FM alloys

It is worthwhile reviewing the physical properties of Gd and Gd-FM alloys—where the FM is Fe, Co, or Ni—in order to discuss their consequences for the

TSP of FM/Gd/barrier. Amorphous rare-earth transition-metal (RE-TM) alloys or RE/TM multi-layers have attracted much attention as a candidate for a magneto-optical storage medium [70, 71]. There are many excellent reviews on the magnetic properties of RE metals and RE-TM alloys [70–73]. Here we focus on a few fundamental aspects quoted from these reviews within the scope of this chapter.

3.2.1 Magnetic properties of Gd

We have chosen Gd for the electrode material, because Gd presents not only low work-function properties, but also the highest TSP among other heavy rare-earth metals such as Tb, Dy, and Ho [58]. The ground-state configuration of Gd is $4f^7 5d 6s^2$. The ferromagnetism of Gd stems from an indirect RKKY interaction between the strongly-localized $4f$ -electron moments mediated by the conduction electrons [58, 70]. The localized $4f$ electrons mainly contribute the magnetic moment of Gd; the seven unpaired $4f$ electrons contribute $+7 \mu_B$ —where the μ_B is the Bohr magneton—according to Hund’s first rule, and the $5d 6s^2$ conduction electrons contribute $+0.63 \mu_B$. [58, 70]. Meservey *et al.* [58] have investigated the TSP of heavy rare-earth metals, Gd, Tb, Dy, Ho, Er, and Tm with an aluminum-oxide tunnel barrier. They have shown that the TSPs of heavy rare-earth metals do not scale with the total magnetic moments, but is approximately proportional to the magnetic moment of the $5d$ or $6s$ conduction electrons [58]. The TSP of Gd/aluminum-oxide is $13.3 \pm 2.5\%$, the highest among heavy rare-earth metals [58]. Physical properties of a few heavy rare-earth metals are summarized in the table 3.1.

3.2.2 Gd-FM alloys

It is important to understand the magnetic behavior of Gd-FM alloys, since we found that there is an inter-diffusion at the RE/FM interface in the previous chapter. The properties of amorphous RE-TM alloys are strongly dependent on the alloy composition and temperature. The most interesting feature of the amorphous RE-TM alloy is that this system reveals a deep minimum in magnetization as a function of the alloy composition as well as a function of

Table 3.1. Physical properties of heavy rare-earth metals from references: [55], [58], [72], and [73]. The a_o and c_o are the lattice constant of the crystal; the T_C is the Curie temperature; the S is the total spin of $4f$ electrons; the L is the total orbital angular momentum; the J is the total angular momentum; the g is the Landé g factor; the μ is the total magnetic moment; the μ_{CE} is the magnetic moment contributed by conduction electrons; the μ_B is the Bohr magneton; the P is the TSP of RE/Al_2O_3 measured at 0.45 K from Ref. [58].

	Gd	Tb	Dy	Ho	Er	Tm
Atomic number	64	65	66	67	68	69
Ground state [Xe]	$4f^7 5d 6s^2$	$4f^9 6s^2$	$4f^{10} 6s^2$	$4f^{11} 6s^2$	$4f^{12} 6s^2$	$4f^{13} 6s^2$
Crystal structure	hcp	hcp	hcp	hcp	hcp	hcp
a_o (Å)	3.6336	3.6055	3.5915	3.5778	3.5592	3.5375
c_o (Å)	5.7810	5.6966	5.6501	5.6178	5.5850	5.5540
Metallic radius (Å)	1.8013	1.7833	1.7740	1.7661	1.7566	1.7462
Ionic radius (Å)	0.94	0.93	0.92	0.91	0.89	0.87
Density (g/cm ³)	7.900	8.229	8.550	8.795	9.066	9.321
Melting point (°C)	1313	1356	1412	1474	1529	1545
Work function (eV)	3.1	3.0	-	-	-	-
T_C (K)	293.4	219.5	89.0	20.0	20.0	32.0
S	$\frac{7}{2}$	3	$\frac{5}{2}$	2	$\frac{3}{2}$	1
L	0	3	5	6	6	5
$J = L + S$	$\frac{7}{2}$	6	$\frac{15}{2}$	8	$\frac{15}{2}$	6
g	2	$\frac{3}{2}$	$\frac{4}{3}$	$\frac{5}{4}$	$\frac{6}{5}$	$\frac{7}{6}$
gJ	7.0	9.0	10.0	10.0	9.0	7.0
μ (μ_B)	7.63	9.34	10.33	10.34	9.1	7.14
μ_{CE} (μ_B)	0.63	0.34	0.33	0.34	0.1	0.14
P (%)	13.3 ± 2.5	6.0 ± 1	6.4 ± 1	7.1 ± 1	5.0 ± 1	2.7 ± 1

temperature [70, 71]. A RE-TM alloy comprises two sub-networks of RE and TM atoms. The inter-atomic RE-TM exchange is antiferromagnetic (negative) below a magnetic ordering temperature (T_C); therefore, the net magnetic moment (M_{net}) of the RE-TM alloy is expressed as

$$M_{net} = M_{RE} - M_{TM}, \quad (3.3)$$

where M_{RE} (M_{TM}) is the magnetization from the RE (TM) subnetwork [70]. At a compensation temperature (or at a compensation composition), the two subnetwork magnetizations cancel each other, and reveal null net magnetic moment. Gambino [70] has explained the reason for the negative exchange between RE and TM as follows: "it is likely that the rare earth exchange mainly involves the $6s$ and $5d$ electrons which have much greater radial extent than the $4f$ electrons. The rare earth $5d$ and the transition metal $3d$ inter-atomic exchange is probably positive (ferromagnetic) but the $5d-4f$ rare earth intra-atomic exchange is strongly negative." We will recall his remark in analyzing the TSP of FM/Gd/barrier in section 3.4.

The magnetic moment of an atom is sensitive to its local environment; a minimum exchange interaction from magnetic neighbors is required for the atom to carry a magnetic moment [72]. The exchange energy between two subnetworks can be obtained from the mean field theory [70–72]. The strength of major exchange interactions strongly depends on the inter-atomic distance;

$$|J_{TM-TM}| > |J_{RE-TM}| \gg |J_{RE-RE}|, \quad (3.4)$$

where J_{A-B} represents the strength of the exchange interaction between A and B subnetwork [70, 72]. The strong J_{TM-TM} and J_{RE-TM} mainly contribute the magnetic properties of Gd-FM alloys; J_{RE-RE} is relatively unimportant in Gd-FM alloys—usually 2 orders of magnitude smaller than J_{TM-TM} . [71, 72]

It is known that the amorphous Gd-Co alloys are simple ferromagnets, but the amorphous Gd-Fe or Gd-Ni alloys show great complexity [70–72]. J_{TM-TM} and J_{RE-TM} are strongly dependent on the alloy composition, and so is the magnetic ordering temperature as shown in the Fig. 3.1. For example, the magnetic ordering temperature of Gd_xCo_{1-x} alloy decreases steeply with increasing Gd content down to $T_C = 200$ K at $x = 0.6$, and develops a minimum T_C of 150 K at $x = 0.8$ [74]. Gd_xNi_{1-x} alloy has much lower ferromagnetic ordering temperature [75]. For Ni rich composition ($x \ll 0.2$),

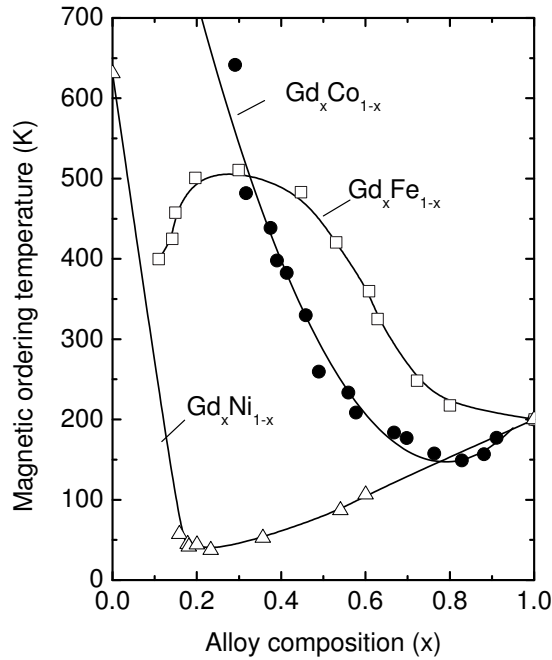


Figure 3.1. Compositional variation of the Curie temperature for RE-TM alloys from references. GdCo: Ref. [71]; GdFe: Ref. [71]; GdNi: Ref. [75].

the Ni develops a strong magnetic moment due to ferromagnetic ordering between Ni atoms [75]. The ferrimagnetic ordering temperature of $\text{Gd}_x\text{Ni}_{1-x}$ alloy also decreases steeply down to 40 K at $x = 0.2$ with increasing Gd content, and then it increases slowly as Ni starts to act like a non-magnetic diluent among the ferromagnetically-coupled Gd [75]. $\text{Gd}_x\text{Fe}_{1-x}$ alloy shows even more complex characteristics, because the magnetic moments of the Fe subnetwork are not parallel, but are panned out [70]. The magnetic ordering temperature of Gd-rich $\text{Gd}_x\text{Fe}_{1-x}$ alloys are higher than those of Gd-rich Gd-Co and Gd-rich Gd-Ni alloys, but sensitive to the method of sample preparation [71, 72].

3.2.3 Gd/FM and Gd/insulator interfaces

It is necessary to understand the properties Gd/FM and Gd/insulator interfaces, as the FM/ Gd/ Al_2O_3 tunnel contact comprises two interfaces: Gd/

$\text{Ni}_{80}\text{Fe}_{20}$ and $\text{Gd}/\text{Al}_2\text{O}_3$ interfaces. Because the magnetic moment of Gd is very sensitive to local environment, a Gd deposition on a non-magnetic material results in a decrease of the Curie temperature of the Gd film. Farle *et al* [76] found that the Curie temperature of 5-100 monolayers Gd on $\text{W}(110)$ decreases with decreasing the film thickness, T_C (hcp crystalline Gd) = 292.5 K to T_C (5 monolayers) = 120 K; the Curie temperature of film depends also on the growth conditions very sensitively. For example, the Curie temperature of amorphous Gd is about 200 K much lower than the T_C of hcp crystalline Gd[70–72]. On the other hand, the Curie temperature of a Gd layer may be enhanced by placing a ferromagnetic layer with high Curie temperature at the proximity of the Gd layer. This is what we are aiming for. We have expected the increase of the Curie temperature of Gd by using $\text{FM}/\text{Gd}/\text{Al}_2\text{O}_3/\text{Si}$ tunnel contacts instead of a pure- $\text{Gd}/\text{Al}_2\text{O}_3/\text{Si}$ tunnel contact.

RE/FM bi-layers, FM/RE/FM sandwiches, and RM/FM multilayers represent very interesting magnetic systems with various magnetic configurations [77–80]. For example, the magnetic moment of Gd in a Gd/Fe multilayer shows a twisted spin state [77]. The exchange interaction between the elements can explain the complex behaviors of RE/FM bi-layers, FM/RE/FM sandwiches, and RE/FM multilayers.

3.3 Fabrication of magnetic tunnel junctions

In order to determine the TSP of the $\text{Ni}_{80}\text{Fe}_{20}/\text{Gd}/\text{Al}_2\text{O}_3$ electrode, we have fabricated metal MTJs with a well-known counter electrode, Co. The MTJ stack—fabricated on Al_2O_3 (0001) substrates—consists of Co (8 nm)/ Al_2O_3 (3 nm)/ Gd (0 to 1.8 nm)/ $\text{Ni}_{80}\text{Fe}_{20}$ (15 nm)/ Al (1 nm), as shown in Fig. 3.2. The MTJ stack has a layer structure with a well-known bottom Co/ Al_2O_3 electrode with a top $\text{Ni}_{80}\text{Fe}_{20}/\text{Gd}/\text{Al}_2\text{O}_3$ electrode. Because we know the TSP of Co/ Al_2O_3 from separate MTT measurements[69], we can obtain the TSP of $\text{Ni}_{80}\text{Fe}_{20}/\text{Gd}/\text{Al}_2\text{O}_3$, measuring the TMR of Co/ $\text{Al}_2\text{O}_3/\text{Gd}/\text{Ni}_{80}\text{Fe}_{20}$.

It is necessary to pattern the MTJs into a cross-geometry structure for TMR measurements. We have used a shadow mask process for patterning tunnel junction layouts with consecutive depositions through different metal shadow masks. We have selected this method because the shadow mask technique provides us shorter process time than the standard lithography and ion

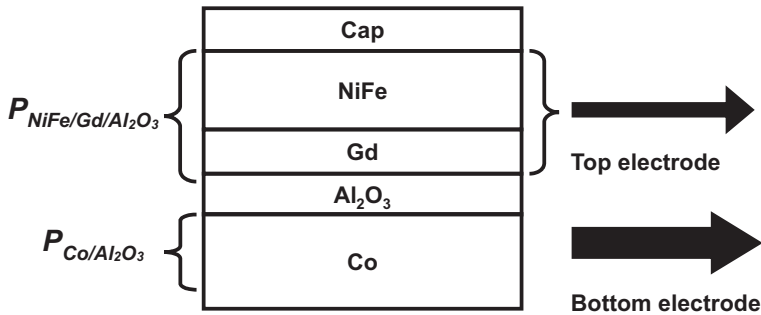


Figure 3.2. A schematic representation of a magnetic tunnel junction with a low work-function Gd layer.

beam etching process.

The patterning steps of the shadow mask technique are as follows. First, the bottom Co layer is deposited through a strip mask. Then a metal Al layer is deposited on top of the Co layer through the same strip mask and subsequently oxidized in a remote oxygen plasma. In chapter 2, we have evaporated Al_2O_3 to form a tunnel barrier on top of Si. We find that the Al_2O_3 deposition shows very smooth layer on Si while an Al deposition shows a rough layer on Si. In the MTJ fabrication, we use metal Al deposition instead of Al_2O_3 deposition for the barrier formation, because the metal deposition provides a better quality of barrier on top of the Co metal electrode. The junction area is defined using a thick insulation layer with a $250\text{-}\mu\text{m}$ -wide slit structure. Finally, top electrode materials are deposited through a shadow mask to form $300\text{-}\mu\text{m}$ -wide cross strips. We have measured the roughness of Co/ Al_2O_3 surface of a test sample after the plasma oxidation using an atomic force microscope (AFM) to examine the quality of the surface. The surface shows an rms roughness of 0.17 nm in $1\text{ }\mu\text{m}$ square area. This guarantees that the surface of Co/ Al_2O_3 electrode has almost similar smoothness compared to the Si/ Al_2O_3 surface shown in chapter 2.

The deposition of magnetic materials requires careful attention, since the deposition at an oblique angle often induces a magnetic anisotropy in the film. We will discuss this issue in chapter 5 in detail. In order to avoid any complexity caused from the growth-induced anisotropy, we have used two processes. The first method is to maintain the same deposition angle for the bottom magnetic electrode and the top magnetic electrode to keep the mag-

netic easy axis in the same direction for both layers; the second method is to pin the magnetic moment of one electrode using an exchange coupling from an anti-ferromagnetic layer. We have used the latter method when the coercivities of the top and bottom electrodes of a MTJ are very close to each other.

3.4 MTJs with a low work-function Gd interlayer

In this section, we describe the properties of MTJs with a low work-function Gd interlayer. We investigate the TSP of the tunnel contacts, $\text{Ni}_{80}\text{Fe}_{20}/\text{Gd}/\text{Al}_2\text{O}_3$, versus the thickness of the Gd interlayer. We study the TSP and resistance (R) of the tunnel contacts versus temperature as well as the TSP and R versus the applied voltage bias.

In order to determine the tunnel spin polarization of the $\text{Ni}_{80}\text{Fe}_{20}/\text{Gd}/\text{Al}_2\text{O}_3$ electrode, we have fabricated metal MTJs consisting of Co (8 nm)/ Al_2O_3 (3 nm)/Gd (0 to 1.8 nm)/ $\text{Ni}_{80}\text{Fe}_{20}$ (15 nm)/Al (1 nm), as described in section 3.3. Figure 3.3 shows the TMR versus magnetic field for MTJs with different Gd interlayers measured at 100 K. All curves show a reasonably high value of TMR and two clear transitions corresponding to the magnetization reversal of the bottom Co electrode (~ 35 Oe) and the top Gd/ $\text{Ni}_{80}\text{Fe}_{20}$ electrode (~ 10 Oe). The TMR as a function of thickness of the Gd interlayer is given in Fig. 3.4 at four different temperatures: 10 K, 100 K, 200 K, and 300 K.

From the measured TMR values, the TSP of the $\text{Ni}_{80}\text{Fe}_{20}/\text{Gd}/\text{Al}_2\text{O}_3$ electrode is calculated using Eq. 3.2 where the TSP of the Co/ Al_2O_3 electrode was independently determined from magnetic tunnel transistor experiments [69]. The TSP of the Co/ Al_2O_3 electrode is 36%, 35%, 33%, 30%, respectively at 10, 100, 200, and 300 K. We find that the TSP of $\text{Ni}_{80}\text{Fe}_{20}/\text{Gd}/\text{Al}_2\text{O}_3$ electrodes at 100 K remains reasonably large; the spin tunnel contacts at 100 K show a TSP higher than 10% even for the thickest Gd layer. In chapter 2 we found that the RA product of the contacts starts to saturates with increasing Gd thickness at 0.8 nm Gd thickness, and shows the optimum for the electrical spin injection and detection. The TSP of a contact with a 0.8-nm Gd layer is 19%, 10%, and 5%, respectively, at 100, 200, and 300 K (Fig. 3.4(b)). This means that the $\text{Ni}_{80}\text{Fe}_{20}/\text{Gd}/\text{Al}_2\text{O}_3$ tunnel contact satisfy the second requirement of the source and drain contacts, a reasonably high

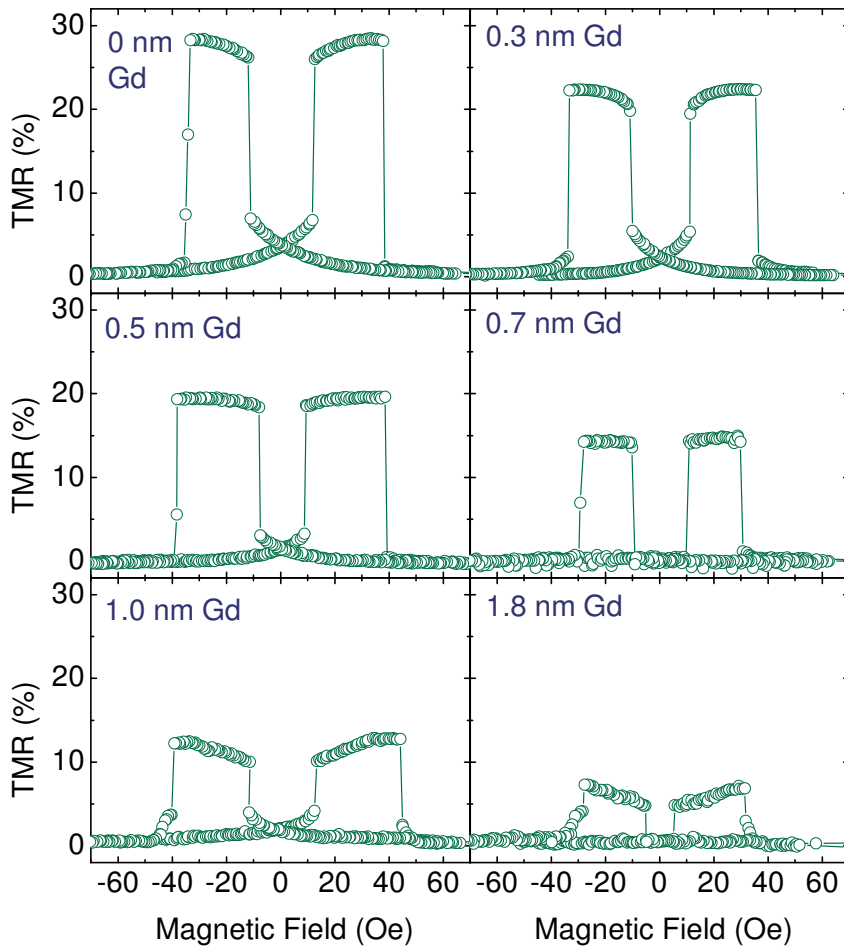


Figure 3.3. TMR of MTJs with a low work-function ferromagnet versus magnetic field measured at 100 K. The MTJs consists of Co (8 nm)/ Al₂O₃ (3 nm)/ Gd (0.3 to 1.8 nm)/ Ni₈₀Fe₂₀ (15 nm).

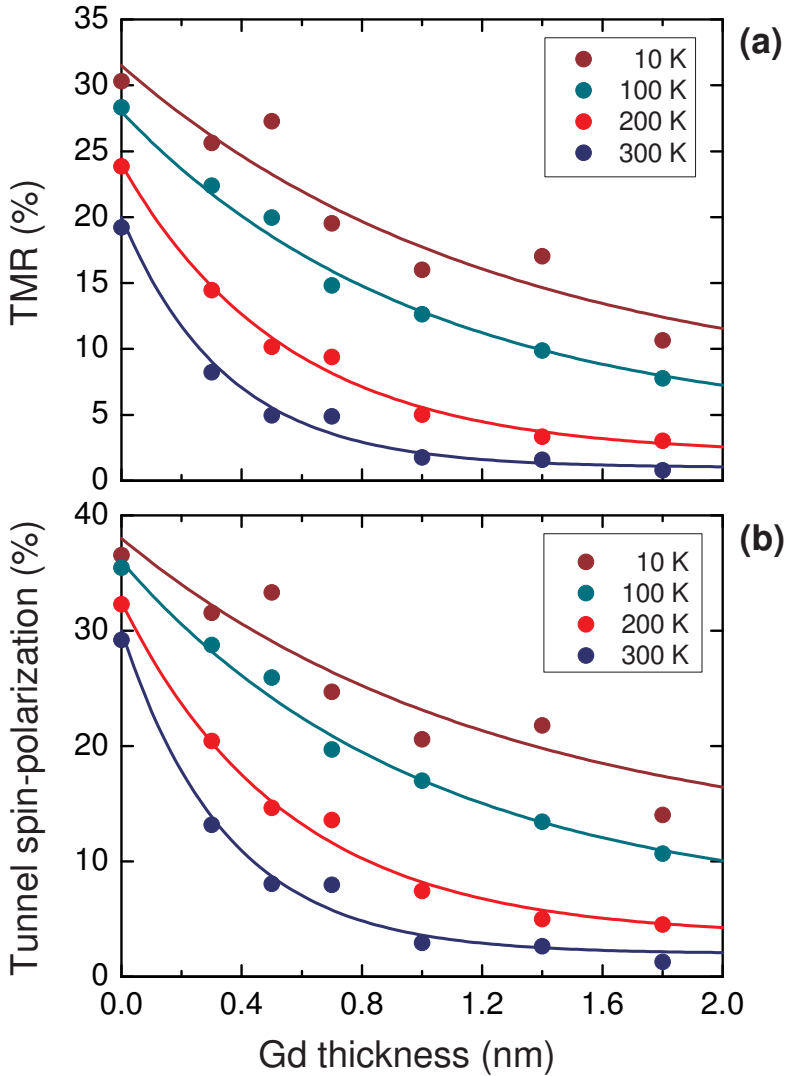


Figure 3.4. (a) TMR and (b) TSP of MTJs with low work function ferromagnet. The MTJs consists of Co (8 nm)/ Al_2O_3 (3 nm)/ Gd (0.3 to 1.8 nm)/ $\text{Ni}_{80}\text{Fe}_{20}$ (15 nm). TMR and TSP, respectively, as a function of the thickness of the Gd interlayer measured at four different temperatures, 10 K, 100 K, 200 K, and 300 K. The solid lines are a guide to the eyes.

TSP.

The magnetic interactions in the $\text{Ni}_{80}\text{Fe}_{20}/\text{Gd}/\text{Al}_2\text{O}_3$ are complicated, because of the amorphous RE-TM elements. The MTJs without a Gd layer shows a large TSP, $\sim 38\%$. The TSP of the contact decreases as the Gd thickness increases as shown in the figure Fig. 3.4(b). The experimental results in Fig. 3.4(b) show that the measured TSP is positive in the measured Gd thickness range. In order to understand this, we should take into account the following three points.

First, the element-specific TEM image in chapter 2 (see Fig. 2.23) indicates that some amount of Ni (and possibly Fe) diffuses into the Gd layer, transforming the Gd layer into a Gd-Ni alloy layer. The exact alloy composition is not known. It is likely that the alloy composition at the Al_2O_3 surface is relatively Ni-rich with a thinner Gd thickness, and the alloy composition is relatively Gd-rich with a thicker Gd layer. Second, Fig. 3.1 shows that the magnetic ordering temperature (T_C) of Gd-Ni alloy is quite low. For example, the T_C of $\text{Gd}_{20}\text{Ni}_{80}$ alloy is about 40 K. Third, the TSP of Gd is mainly attributed by the $5d$ and $6s$ conduction electrons, not the $4f$ electrons. The bulk Gd has a moment of $+7 \mu_B$ from the $4f$ electrons, and $+0.63 \mu_B$ due to the $5d$ and $6s$ conduction electrons. Total moment $+7.63 \mu_B$ (table 3.1) suggests that both moments are aligned parallel. The TSP of pure Gd measured with the Tedrow/Meservey technique is positive ($+13\%$, see section 3.2.1), which is consistent with tunneling of the $5d$ and $6s$ conduction electrons with $+0.63 \mu_B$ moment aligned along the total Gd moment.

It is known that the magnetic moment of Gd in Gd-TM alloys is antiferromagnetically coupled with that of TM. However, we don't know whether all electrons ($4f$, $5d$, and $6s$) of Gd is 100% antiferromagnetically coupled with those of Ni. If the inter-atomic exchange coupling between rare earth (Gd) $5d$ and the transition metal Ni $3d$ is antiferromagnetic, the TSP can be negative in a Gd-rich Gd-Ni alloy where the tunneling from the Gd is dominant. However, the experimental results in Fig. 3.4(b) show that the measured TSP is always positive in all Gd thickness range. This suggests two possibilities: (i) the alloy composition is Ni-rich where the tunneling from Ni is dominant, or (ii) the inter-atomic exchange coupling between rare earth $5d$ and the transition metal $3d$ is ferromagnetic. For case (i), there would be a positive contribution (Ni) and a negative contribution (Gd, $5d$, $6s$), and their relative contribution determines the overall sign of the TSP. If there are large amount of Ni atoms at the surface of Al_2O_3 barrier, the total TSP is also dominantly

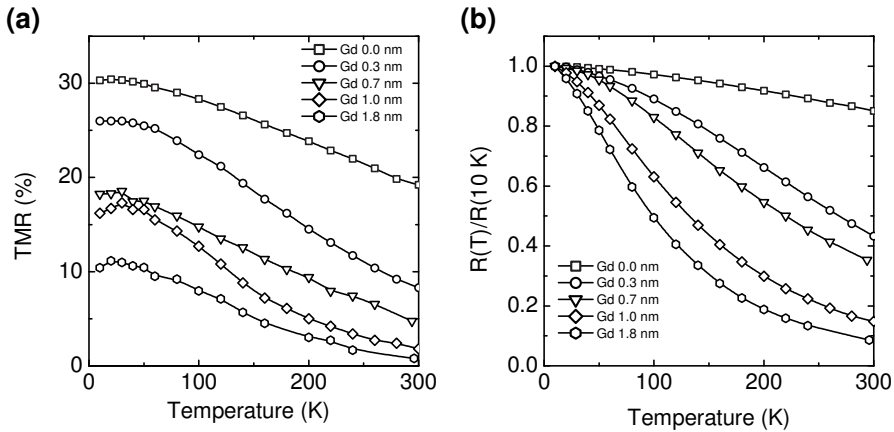


Figure 3.5. Temperature (T) dependence of (a) TMR and (b) resistance of MTJs with a low work-function ferromagnet. The MTJs consists of Co (8 nm)/ Al₂O₃ (3 nm)/ Gd (0.3 to 1.8 nm)/ Ni₈₀Fe₂₀ (15 nm). The resistance, $R(T)$ is normalized to the resistance measured at 10 K.

determined by the TSP of Ni of which magnetic moment is aligned parallel to the magnetic moment of the big Ni₈₀Fe₂₀ layer. For case (ii), it would be useful to remember that the inter-atomic exchange coupling between rare earth $5d$ and the transition metal $3d$ is possibly ferromagnetic, but the $5d$ – $4f$ rare earth intra-atomic exchange is strongly antiferromagnetic[70]. Although the magnetic moments of the Ni₈₀Fe₂₀ ($3d$ electrons) subnetwork and that of Gd ($4f$ electrons) subnetwork are coupled antiferromagnetically, it is possible that the $5d$ and $6s$ conduction electrons of Gd— which mainly contributes the TSP—are coupled ferromagnetically with the conduction electrons of the Ni. Consequently, the TSP of Gd/ Al₂O₃ can have the same polarity as the TSP of Ni₈₀Fe₂₀/ Al₂O₃. Nevertheless, it is difficult to decide which explanation is right, and further study is required.

For the Gd films much thicker than 2 nm, the TMR measurement as a function of magnetic field was found to be not reproducible. The shape of TMR curves lacks clear switching, which changes irregularly from one measurement to another. When the Gd thickness is thin enough in our experiment, the magnetic moment of Gd is strongly coupled with those of Ni and Fe. Accordingly, the magnetization of the FM layer aligns the Gd magnetic moments uniformly in one direction. As the Gd thickness becomes thicker than the characteristic length of the exchange coupling, the magnetization of the FM layer can no longer aligns the Gd magnetic moments on the Al₂O₃

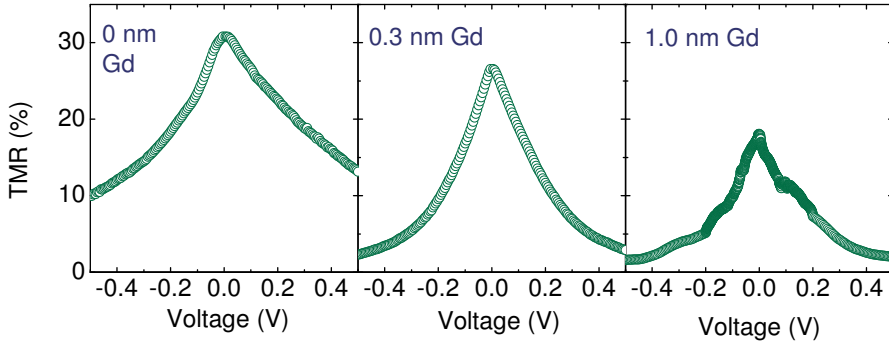


Figure 3.6. TMR versus applied voltage bias ($T = 5$ K) of (a) an MTJ without a Gd layer, (b) an MTJ with a 0.3 nm Gd layer, and (c) an MTJ with a 1.0 nm Gd layer. Electrons tunnel into the top (bottom) electrode at the positive (negative) voltage range. A Gd layer is the top electrode, and a Co layer is the bottom electrode.

surface uniformly. It is likely that the magnetic moments of both FM and Gd layers rotate out of the applied-field angle within a characteristic length, which depends on the magnetic anisotropy and the exchange energy of the materials [77, 80].

Figure 3.5 shows the temperature dependence of the resistance and TMR of MTJs, Co (8 nm)/ Al₂O₃ (3 nm)/ Gd (0 to 1.8 nm)/ Ni₈₀Fe₂₀ (15 nm)/ Al (1 nm). The MTJs with a Gd interlayer display stronger temperature dependence than that of the MTJ without Gd interlayer. As the temperature increases from 10 K to 300 K, the resistance of the MTJs with a Gd interlayer decreases a factor of 2 to 10, and their TMR decreases a factor of 3 to 14. We find, in the chapter 2, that some amount of Gd diffuses into the Al₂O₃ barrier, while the diffusion of Gd into the Ni₈₀Fe₂₀ layer is negligible. The Gd diffusion into the tunnel barrier results in this strong temperature dependence. It is known that three mechanisms—the spin conserved tunneling, impurity assisted tunneling, and spin exchange scattering—contribute the tunnel conductance of the junction with a doped-barrier [81]. Jansen *et al.* [81] have reported that magnetic impurity inside a barrier yields the spin-exchange scattering, which enhances the temperature and bias dependence of TMR.

The MTJs with a Gd interlayer shows a stronger bias dependence of TMR (Fig. 3.6) in comparison with that of a control sample without a Gd layer. Fig. 3.7 shows the differential conductance (dI/dV) of MTJs as a function of the applied voltage bias. The control sample without a Gd interlayer shows

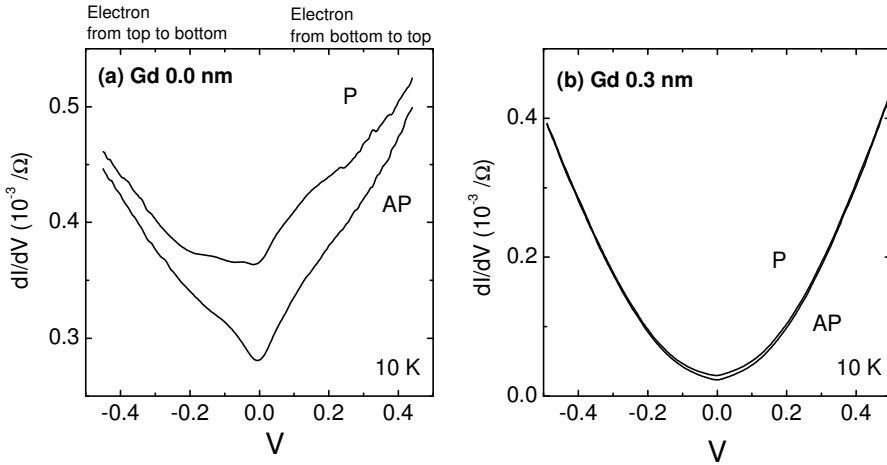


Figure 3.7. Differential conductance (dI/dV) versus applied voltage bias of (a) an MTJ without a Gd layer and (b) an MTJ with a 3-nm Gd layer. The MTJs consist of Co (8 nm)/ Al₂O₃ (3 nm)/ Gd (0.0 or 0.3 nm)/ Ni₈₀Fe₂₀ (15 nm). Electrons tunnel into the top (bottom) electrode at the positive (negative) voltage range. The Gd layer is the top electrode, and the Co layer is the bottom electrode.

typical zero bias anomaly of MTJs, while the sample with a Gd interlayer displays a steep parabolic increase of the conductivity with increasing the voltage bias. We believe that this is also the consequence of the Gd diffusion into the tunnel barrier as also found for Ni doping of Al₂O₃ barriers[81]. Because this strong temperature and bias dependence of the TMR are unprofitable for the spin tunnel contact, these properties should be improved.

3.5 MTJs with a Gd/Co bi-layer

The main motivation to study MTJs with a Gd/Co bi-layer electrode is to increase the TSP of magnetic tunnel contacts with a low work-function interlayer at room temperature. Because amorphous Gd-Co alloy has a higher magnetic ordering temperature than that of the Gd-Ni alloys (Fig. 3.1), the TSP of Co/Gd/Al₂O₃ might be also higher than that of Ni₈₀Fe₂₀/ Gd/ Al₂O₃ at the same temperature.

We have investigated the tunnel spin polarization of the Co/ Gd/ Al₂O₃ electrode by fabricating MTJs with this electrode. The MTJ stack, fabricated

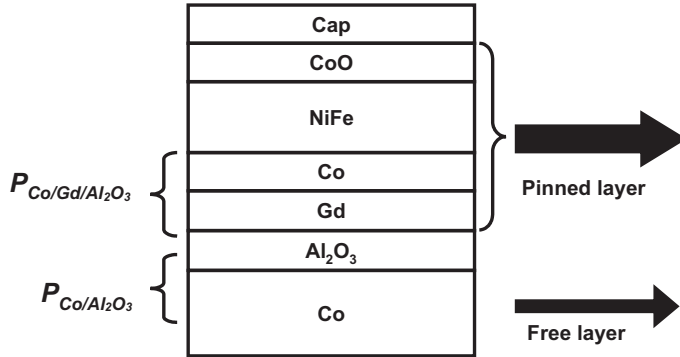


Figure 3.8. A schematic representation of a magnetic tunnel junction with a Gd/Co bi-layer. An exchange biasing layer (CoO) fixes the magnetization of the top $\text{Ni}_{80}\text{Fe}_{20}$ electrode, while the magnetization of the bottom Co layer rotates freely with a field of 100 Oe.

Table 3.2. TMR of the MTJs with a Gd/Co bilayer.

Sample No.	Gd thickness (nm)	Co thickness (nm)	TMR at 10 K (%)	TMR at 100 K (%)
1	0.0	1.0	28.5	26.7
2	0.2	1.0	23.3	19.8
3	0.4	0.6	23.4	17.5
4	0.6	0.6	19.9	13.2
5	0.8	0.2	7.3	3.3
6	1.0	0.2	-3.7	-0.8

on Al_2O_3 (0001) substrates, consists of Co (8 nm)/ Al_2O_3 (3 nm)/ Gd (x nm)/ Co (y nm)/ $\text{Ni}_{80}\text{Fe}_{20}$ (15 nm)/ CoO (2.5 nm)/ Al (1 nm), as shown in the Fig. 3.8. We have varied the Co and Gd layer thickness, x and y , as summarized in the table 3.2. It is known that a strong asymmetric diffusion occurs at a Co/Gd interface; Co diffuses throughout the Gd layers and forms a $\text{Gd}_x\text{Co}_{1-x}$ alloy that is limited at nearly the eutectic composition ($\text{Gd}_{63}\text{Co}_{37}$) [78]. We expect a different Co/Gd bilayer configuration results in a different Co-Gd alloy composition at the Al_2O_3 surface.

We have used an exchange biasing layer to pin the magnetization of the

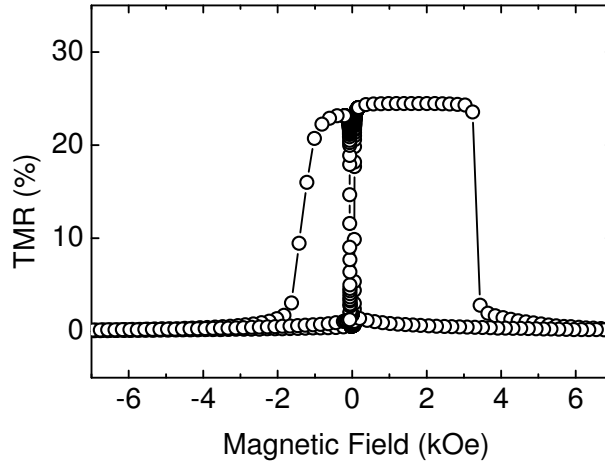


Figure 3.9. TMR of MTJs with a Gd/Co bi-layer versus magnetic field measured at 10 K. The MTJs consists of Co (8 nm)/ Al₂O₃ (3 nm)/ Gd (0.2 nm)/ Co (1.0 nm)/ Ni₈₀Fe₂₀ (15 nm)/ CoO (2.5 nm)/ Al (1 nm). This curve shows a full hysteresis loop

top Ni₈₀Fe₂₀ electrode, since the coercivity of the top Gd/Co electrode is very close to that of the bottom Co electrode. An anti-ferromagnetic CoO layer is formed by Co deposition (2.5 nm) on the Ni₈₀Fe₂₀ layer and by *in situ* plasma oxidation (3 min). The low blocking temperature of CoO (~ 240 K) limits the temperature range of the exchange bias. The Ni₈₀Fe₂₀ layer has two functions: to control the magnetization of the Gd/Co layers and to protect those layers from the oxidation. The fixed magnetic moment of the Ni₈₀Fe₂₀ magnet aligns the magnetic moment of the Co in the same direction, and thereby the magnetic moment of the Gd in the opposite direction owing to the strong anti-ferromagnetic coupling between the Co and the Gd in the layer.

Figure 3.9 shows the TMR versus the applied magnetic field for MTJs consisting of Co (8 nm)/ Al₂O₃(3 nm)/ Gd (0.2 nm)/ Co (1.0 nm)/ Ni₈₀Fe₂₀ (15 nm)/ CoO (2.5 nm)/ Al (1 nm) measured at 10 K. This curve shows a full hysteresis loop, where the Co bottom layer switches at a small field (~ 50 Oe), and the exchange-biased top electrode switches at higher field (a few kOe). Because of the relatively high switching field of the top electrode, we can assume the top electrode as a fixed magnet within 100 Oe magnetic field range.

Figure 3.10 shows the TMR versus the applied magnetic field for the MTJs with various Gd/Co bi-layers measured at 10 K. All curves show clear transitions corresponding to the magnetization reversal of the bottom Co elec-

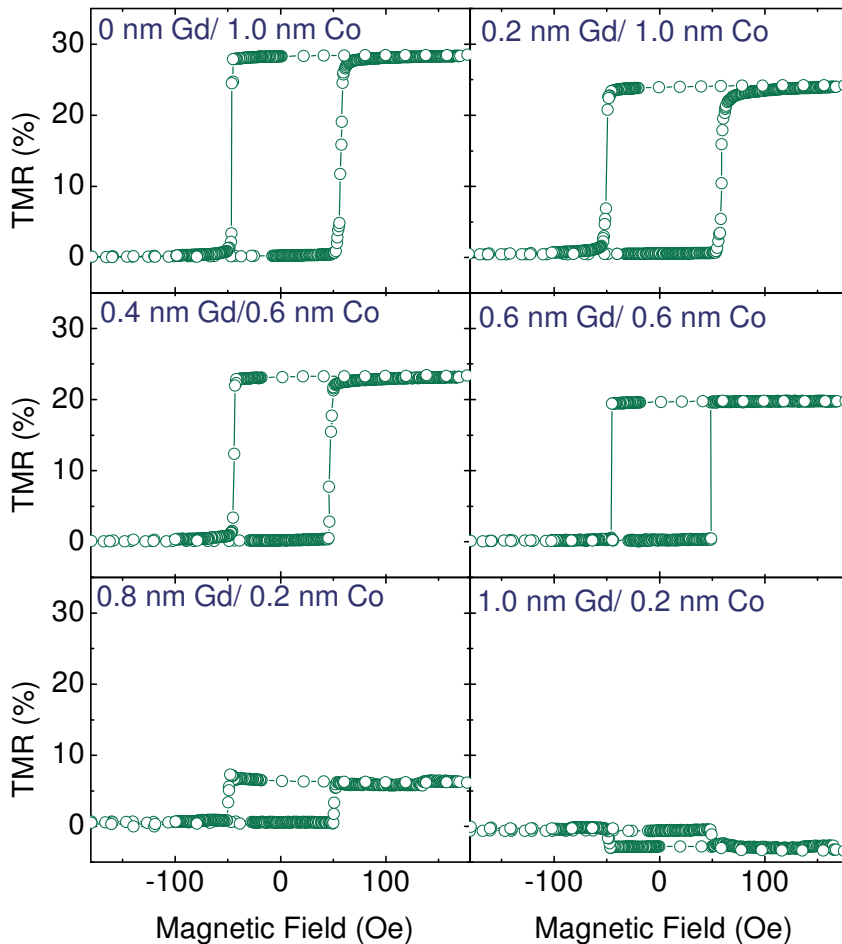


Figure 3.10. TMR of MTJs with a Gd/Co bi-layer versus magnetic field measured at 10 K. The MTJs consists of Co (8 nm)/ Al_2O_3 (3 nm)/ Gd (x nm)/ Co (y nm)/ $\text{Ni}_{80}\text{Fe}_{20}$ (15 nm)/ CoO (2.5 nm)/ Al (1 nm). These curves show only minor hysteresis loops with a small magnetic field, where only the magnetization of the bottom Co layer switches. The magnetic moments of the top and bottom electrodes are in the antiparallel (parallel) configuration with the positive (negative) magnetic field.

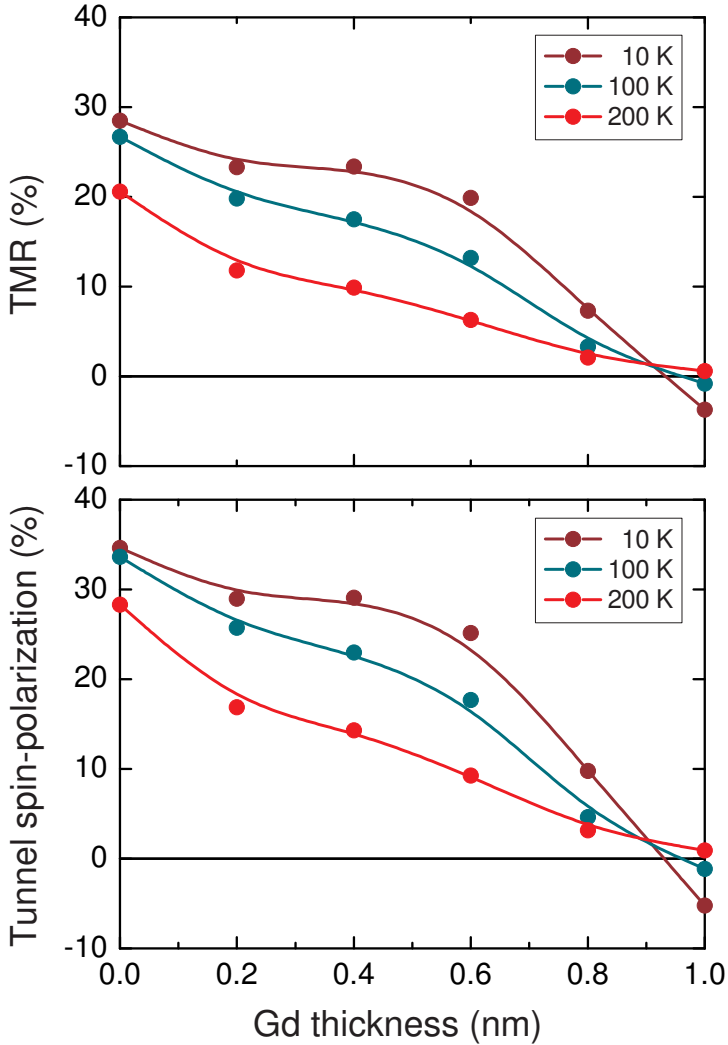


Figure 3.11. (a) TMR of MTJs with a Gd/Co bi-layer. The MTJs consists of Co (8 nm)/ Al₂O₃(3 nm)/ Gd (x nm)/ Co (y nm)/ Ni₈₀Fe₂₀ (15 nm)/ CoO (2.5 nm)/ Al (1 nm). (b) TSP of the Al₂O₃ (3 nm)/ Gd (x nm)/ Co (y nm)/ Ni₈₀Fe₂₀ (15 nm) electrode. TMR and TSP, respectively, as a function of the thickness of the Gd interlayer measured at three different temperatures, 10 K, 100 K, and 200 K. The solid lines are a guide to the eyes.

trode only. The MTJs with a thinner Gd layer ($t_{Gd} < 0.6$ nm) present a reasonably high value of TMR, but the MTJ with a 0.8 nm presents a quite small TMR. The most striking result is that the MTJ with a 1.0 nm Gd layer shows a small negative TMR.

Fig. 3.11 shows the TMR of MTJs consisting of Co (8 nm)/ Al₂O₃(3 nm)/ Gd (x nm)/ Co (y nm)/ Ni₈₀Fe₂₀ (15 nm)/ CoO (2.5 nm)/ Al (1 nm), and TSP of the Al₂O₃ (3 nm)/ Gd (x nm)/ Co (y nm)/ Ni₈₀Fe₂₀ (15 nm) electrode as a function of thickness of the Gd interlayer at three different temperatures: 10 K, 100 K, and 200 K. The TSP values are obtained by the same way that we have described in the section 3.4. The TSP measured at 10 K decreases slightly with increasing the Gd thickness up to 0.6 nm, showing a positive value higher than 25%. As the Gd thickness increases further, the TSP of the tunnel contact decreases steeply, crosses zero, and becomes negative at the thickest Gd layer. With increasing temperature, the TSP at a small Gd thickness remains positive, but the TSP at 1-nm Gd thickness changes its sign from negative ($T < 100$ K) to positive ($T > 200$ K). Consequently, the TSP of these tunnel contacts with a thicker Gd layer ($t_{Gd} > 0.6$ nm) is smaller in comparison with the tunnel contacts of the previous section at the same Gd thickness.

We have observed a negative TSP of the Gd/ Co electrode with a thick Gd layer ($t_{Gd} = 1.0$ nm). In the Al₂O₃/ Gd-Co/ Ni₈₀Fe₂₀ (15 nm) contact, the magnetic moment of Co is aligned ferromagnetically with the moment of the Ni₈₀Fe₂₀ (15 nm) electrode, while the total magnetic moment of Gd is antiferromagnetically aligned with that of Co as well as that of Ni₈₀Fe₂₀ (15 nm) electrode. The Co would contribute positively to TSP, and thus, this cannot explain the negative TSP. Because the $4f$ electrons in Gd does not contribute to the TSP, it means that the negative TSP is due to the Gd $5s$ and $6s$ electrons, which mainly contribute the TSP of Gd. This implies that Gd $5s$ and $6s$ electrons are coupled antiferromagnetically with the $3d$ moment of Co, and coupled ferromagnetically with the Gd $4f$ as in the bulk Gd. This is consistent with the results that Kaiser *et al.*[82] has reported in the TSP of Gd-Co alloy system, taking into account that the direction of the total magnetic moment of a Gd/Co bi-layer is pinned by a bigger Ni₈₀Fe₂₀ magnet in our experiment. The magnetic ion-conduction electron exchange interaction is an oscillatory function of the inter-atomic distance and the wave vector at the Fermi surface [83]; there is a possibility that the sign and magnitude of the magnetic ion-conduction electron exchange interaction depends on the alloy material and composition.

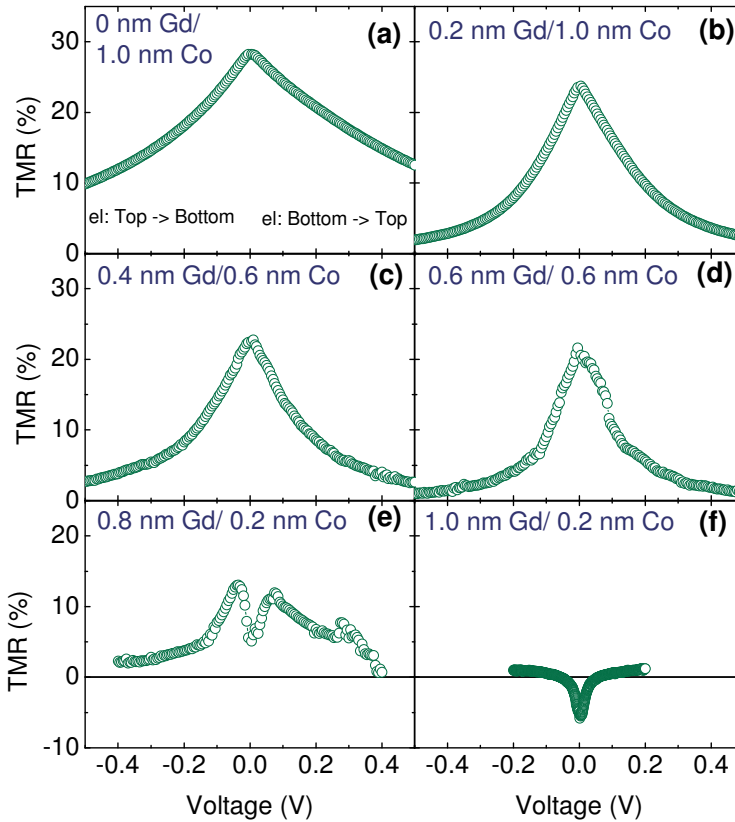


Figure 3.12. TMR versus applied voltage bias of MTJs with a Gd/Co bi-layer. The MTJs consist of Co (8 nm)/ Al₂O₃ (3 nm)/ Gd (x nm)/ Co (y nm)/ Ni₈₀Fe₂₀ (15 nm)/ CoO (2.5 nm)/ Al (1 nm). Electrons tunnel into the top (bottom) electrode at the positive (negative) voltage range. The Gd layer is the top electrode, and the Co layer is the bottom electrode.

The spin tunnel contacts with a Gd/Co bi-layer present a high TSP, if the Gd layer is thin enough. The strong antiferromagnetic coupling between the conduction electrons of Co and Gd results in a steep decrease of the TSP of the tunnel contacts with a thick Gd layer, compromising the benefits from the possible higher Curie temperature of the Gd/Co system. Despite this clear limitation, one can optimize the performance of the spin tunnel contacts, if there is a way to reduce the Schottky barrier height with a thinner Gd thickness. In the next chapter, we will show that it is actually possible that only a

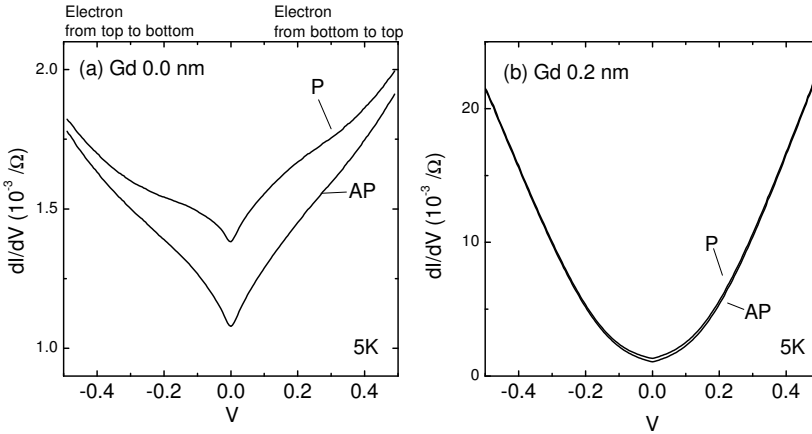


Figure 3.13. Differential conductance (dI/dV) versus applied voltage bias of MTJs (a) without a Gd/Co bi-layer and (b) with a Gd/Co bi-layer. The MTJs consist of Co (8 nm)/ Al_2O_3 (3 nm)/ Gd (x nm)/ Co (1.0 nm)/ $\text{Ni}_{80}\text{Fe}_{20}$ (15 nm)/ CoO (2.5 nm)/ Al (1 nm). Electrons tunnel into the top (bottom) electrode at the positive (negative) voltage range. The Gd layer is the top electrode, and the Co layer is the bottom electrode.

thin Gd layer ($t_{\text{Gd}} < 0.6$ nm) with the Cs-dosed Si surface is enough to get the desired RA product for the suitable source and drain contacts of a spin-MOSFET.

The bias dependence of MTJs with a thinner Gd layer (Fig. 3.12) is similar to the characteristics of MTJs in the section 3.4, but the bias dependence with a thicker Gd layer is peculiar. For instance, the TMR in Fig. 3.12(e) at zero bias is +5%. The TMR increases initially up to the maximum of 14 %, but it starts to decrease with increasing the bias voltage. The TMR in Fig. 3.12(f) at zero bias is -5%. With increasing the bias voltage, the TMR crosses zero and becomes positive. The negative TMR contribution in the bias dependence might be due to the $5d$ and $6s$ conduction electrons of the Gd that are anti-ferromagnetically coupled with the conduction electrons ($3d$ electrons) of the Co. It is not certain that this complex bias dependence as an intrinsic property of the Gd-rich GdCo alloy, and a further study is required to explain this. Figure 3.13 shows that the dI/dV as a function of the voltage bias of MTJs. The control sample without a Gd interlayer shows typical zero bias anomaly of MTJs, but the sample with a Gd interlayer display a steep parabolic increase of the conductivity with increasing the voltage bias.

3.6 Conclusions

We have demonstrated that the spin tunnel contacts with a low work function ferromagnet—inserted between the ferromagnet (FM) and the insulator of FM/Al₂O₃/Si tunnel contacts—injects spin-polarized carriers with a reasonably high TSP into the other electrode through a tunnel barrier. We have fabricated a series of MTJs of NiFe/ Gd/ Al₂O₃/ Co and Co/ Gd/ Al₂O₃/ Co, which show a reasonably high value of TMR with clear magnetization switching. We have obtained the TSP of the NiFe/ Gd/ Al₂O₃ and Co/ Gd/ Al₂O₃ electrode from the measured TMR values, and investigated the TSP as a function of thickness of the low-work function interlayer at different temperatures. We find that the spin tunnel contacts with low work-function ferromagnet has a reasonably high TSP, satisfying the second requirements of the source and drain contacts to realize the Si-based spin MOSFET.

We find that the TSP of tunnel contacts with a low work function ferromagnet depends on many parameters: ferromagnet elements, alloy composition, the strength and the sign of magnetic coupling, voltage bias, and temperature. There is still lots of room for improvement of the TSP at high temperature and the bias dependence. For example, this approach is certainly not limited to Gd, but can be extended to other spin tunneling materials with low work function. We may expect an enhanced TSP using other ferromagnets and barrier materials, or engineering the magnetic coupling of the nm-thin low work-function interlayer to a ferromagnetic material with high Curie temperature. In that respect, it is also of interest that it was recently shown that a low work function and a stable interface/surface are not mutually exclusive[84]. Among thousands of ferromagnetic metals, magnetic alloys, and magnetic oxides, there might be better materials in the sense of higher TSP, higher T_C , lower work function, and better chemical-stability than Gd.

This work opens up a whole new category of tunnel contact materials combining high TSP with low work function. This technique is not only essential to semiconductor-based spintronics, but may also find their way to low RA product applications of MTJs such as read heads in magnetic disk drives. This method could prove useful when the desired RA product is so small that the required thickness of the tunnel barrier enters the range where pinholes can no longer be avoided. The MTJs with RE-TM materials reveal complex magnetic interactions between localized magnetic ions and conduction electrons; this may provide various interesting phenomena possibly use-

ful for spin-transfer torque devices, for example, a reduction of the critical current density in the current-induced magnetization switching by achieving zero magnetization with a high tunnel spin polarization.

Engineering of spin tunnel contacts to Si using Cs

In chapter 2, we have shown that it is possible to control the Schottky barrier height and resistance-area (RA) product of spin tunnel contacts to Si using low work-function materials, inserted between the ferromagnet (FM) and the insulator of FM/ Al_2O_3 / Si tunnel contacts. Here we present another route to control and reduce the Schottky barrier height of FM/ Al_2O_3 / Si contacts very effectively by depositing alkali metal atoms, such as Cs, on the Si surface prior to preparation of the tunnel barrier. A series of measurements has been conducted to understand the mechanism of the reduction of the Schottky barrier height. We find very interesting phenomena with this type of contact; the band bending near the contact can be inverted, leading to a possible formation of a two-dimensional electron gas with n -type Si.

4.1 Introduction and motivation

In the previous chapters, it has been shown that the control of the Schottky barrier height is crucial to observe the magnetoresistance (MR) signal from the Si-based spin-MOSFET. For this purpose, we have presented tunable spin tunnel contacts with a low work-function interlayer, for example, FM/ Gd/ Al_2O_3 / Si contacts. By using this type of contact, it is possible to tune the RA product over many orders of magnitude, and maintain reasonable tunnel spin

polarization.

In this chapter, we present an alternative method to control the Schottky barrier height of FM/ Al_2O_3 / Si contacts by depositing alkali-metal atoms on the Si surface. Alkali metal deposition on a host metal surface, for example, Cs on W, has been widely used for reducing the work function of the metal surface for various technical applications[85, 86]. Alkali-metal-covered material surfaces are known to be very effective to improve the emission efficiency in the photoemission[85]. A low work function observed in a cesiated metal surface is due to a complex dipole formation at the surface, by transferring electronic charge from Cs to the host metal layer[87]. We investigate the effect of Cs deposition on the Schottky barrier height of FM/ Al_2O_3 / Si contacts by inserting Cs either at the metal/insulator interface or at the insulator/Si interface. We shall discuss the feasibility of this approach to obtain the desired resistance-area (RA) product of spin tunnel contacts with a higher tunnel-spin polarization (TSP).

Section 4.2 describes the experimental details on the fabrication of FM/ Al_2O_3 / Si contacts with alkali-metal deposition. It will be demonstrated that the Cs deposition on Si surface offers us very effective way to control the Schottky barrier height of the FM/ Al_2O_3 / Si contacts and to get a low Schottky barrier height. In section 4.3, we obtain the density of the gap states and the charge neutrality level of the FM/ Al_2O_3 / Si contacts with the Cs-covered Si interface by controlling the effective work function of the FM and measuring the Schottky barrier height of the tunnel contact to Si. This measurement will explain the mechanism of the reduction of the Schottky barrier height in this type of contact. It will be shown that the band bending near the contact can be inverted, forming an accumulation layer at the n -type Si surface, suggesting that a two-dimensional electron gas is formed at the n -type Si surface.

4.2 Fabrication of FM//Si contacts with Cs

The fabrication process of FM/ Al_2O_3 / Si contacts with an interfacial Cs layer is the same as that described in the chapter 2 except for the Cs deposition. The Cs layer is deposited using alkali-metal dispensers (SAES getters S.p.A.), which contains a mixture of an alkali metal chromate ($\text{Cs}_2\text{Cr}_2\text{O}$) with a reducing agent (Al 16% and Zr 84%)[88]. Cs is evaporated by flowing current

through a wire-shaped dispenser. Current through the wire is increased by 0.5 A in every minute up to 4.0 A, increased by 0.2 A in every minute from 4 A to 6 A, and maintained at 6 A for 15 minutes. Although the amount of Cs flow is sufficient to reach saturation monolayer coverage at the surface, the exact amount of deposited Cs materials on the sample surface is not known. The Cs deposition has been conducted in a small chamber connected to the main chamber that is used for the FM metal deposition. During the Cs deposition, the pressure is kept to below 5×10^{-7} Torr. The same Cs deposition condition is used for all series of samples. After the Cs deposition, the sample is transferred to the main chamber for the oxide layer deposition. The single-crystal Al_2O_3 has been used for the deposition. The same oxidation time (7.5 min) for Al_2O_3 is used for all series of samples. The condition for the metallic layer is also the same as described in chapter 2, section 3.

We have fabricated three different series of samples; the descriptions of each series and the corresponding Schottky barrier heights of each series are summarized in table 4.1. The series A comprises Si/ Al_2O_3 / Cs/ FM tunnel contacts where Cs is deposited on the Al_2O_3 insulator and thereafter the FM is deposited. We will examine whether a lower Schottky barrier is obtained with this type of contact owing to the low work function of Cs. The series B comprises Si/ Cs/ Al_2O_3 / FM tunnel contacts where Cs is deposited on Si, and thereafter the Al_2O_3 insulator and FM layers are formed. We are interested in the effect of Cs on the modification of the electronic structure of the Si surface. The series C comprises Si/ Cs/ Al_2O_3 / Gd/ FM tunnel contacts where both Gd and Cs are used. The location of the Cs is the same as that in the series B. The purpose of the Gd deposition is to control the effective work function of the FM layer as described in the chapter 2. This will allow us to

Table 4.1. Sample layout of three series of samples and their Schottky barrier heights.

Series	Description (thickness in nm)	SBH (eV)
A	Si/ Al_2O_3 (0.5-1.2)/ Cs/ $\text{Ni}_{80}\text{Fe}_{20}$ (10) /Au (10)	0.45~0.65
B	Si/ Cs/ Al_2O_3 (0.5-1.2)/ $\text{Ni}_{80}\text{Fe}_{20}$ (10) /Au (10)	0.16~0.21
C	Si/ Cs/ Al_2O_3 (0.5-2.3)/ Gd (0-3.0)/ $\text{Ni}_{80}\text{Fe}_{20}$ (10) /Au (10)	-0.05~0.30

obtain the density of the gap states and the charge neutrality level of the FM/ Al_2O_3 /Si contacts with Cs-dosed Si interface.

4.3 Effect of Cs-deposition on Schottky barrier

The curve A in Fig. 4.1 shows the measured I - V characteristic of an FM/Cs/ Al_2O_3 /Si tunnel contact, where the Cs is placed in between the insulator Al_2O_3 and FM metal. Because the work function of Cs (2.14 eV) is lower than that of Gd (3.1 eV), a lower Schottky barrier might be expected for the samples in the series A in comparison with the Schottky barrier of FM/Gd/ Al_2O_3 /Si tunnel contact in chapter 2, section 2.5.3. However, the measured I - V characteristics of the contacts in the series A, for example, curve A in Fig. 4.1 reveals a more rectifying behavior with a low current density in the reverse bias range than the Gd contact in Fig. 2.10. The Schottky barrier height of this contact is 0.65 eV, slightly lower than the Schottky barrier height (0.81 eV) of the contact without Cs layer, but much higher than the Schottky barrier height (~ 0.0 eV) of the contact with a thick Gd layer ($t_{\text{Gd}} > 0.8$ nm). This is contrary to the reported result with a metal surface covered by a Cs layer in vacuum (metal/Cs/vacuum), that shows a huge reduction of the work function of the metal surface[85]. When the deposited Cs layer is thin, about a monolayer, for the metal/Cs bi-layer to possess a work function of bulk Cs material, the effective work function of the bi-layer depends on the behavior of the surface dipole. The difference between metal/Cs/ Al_2O_3 and metal/Cs/vacuum might explain why Cs layer in between the metal/insulator interface is not effective to reduce the work function. In the metal/Cs/ Al_2O_3 contacts, Cs can give its electron charge either to the Al_2O_3 or the metal in the contact, while Cs on metal/Cs/vacuum structure can only give its electron charge to the host metal. Therefore, the formation of an electric dipole in metal/Cs/ Al_2O_3 can be different from that in metal/Cs/vacuum.

The curve B in Fig. 4.1 shows the measured I - V characteristics of FM/ Al_2O_3 /Cs/Si tunnel contacts, where the Cs is positioned in between the Al_2O_3 insulator and Si instead of in between the metal and the insulator. This curve appears less rectifying, and shows a low Schottky barrier height, 0.21 eV as deduced from the temperature dependence of the IV characteristics as described in chapter 2, section 2.5.4 (see Fig. 2.15 as an example). In order to

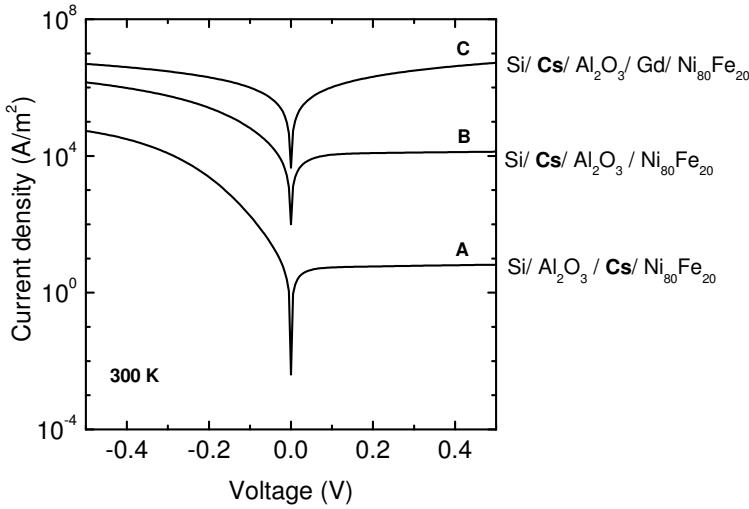


Figure 4.1. Typical I - V curves of three different samples from series A, B, and C. The sample layouts are given in table 4.1. The nominal thickness of the Al_2O_3 insulator is 0.5 nm; the thickness of the Al_2O_3 insulator obtained from the TEM experiment is 1.5 nm (see chapter 2, Fig. 2.4; the oxidation time for Al_2O_3 was 7.5 min.) The thickness of the Gd layer 3 nm, and the thickness of the $\text{Ni}_{80}\text{Fe}_{20}$ layer is 10 nm. The positive voltage corresponds to the electron transport from metal to Si, and the negative voltage to the electron transport from the Si to metal.

interpret this low Schottky barrier height, we have to understand the structure and electrical properties of Cs at the Cs/Si interface. Cs may affect the Schottky barrier height in two ways: Cs atoms adjacent to Si makes a change in the formation of the surface dipole at the Si interface, or Cs can induce electronic states in the band gap of Si[47, 89]. The surface dipole formed at Si surface would make the work function of the Si lower, if the Cs donates its electron to the Si, which increases the work function difference between the FM and Si. Consequently, this would lead to the increase of the Schottky barrier height, which is contrary of the lowering of the Schottky barrier height observed in the Si/ Cs/ Al_2O_3 contact. Hence, the effect of Cs layer in the Si/ Cs/ Al_2O_3 contact is different from the influence of Cs layer in the metal/ Cs/ Al_2O_3 or metal/ Cs/ vacuum. In order to investigate this further, we have performed a series of measurements with various Gd thickness (series C) to be presented below.

The tunnel contacts in series C consist of FM/ Gd (x nm)/ Al_2O_3 / Cs/ Si.

The layer structure is the same as the contacts in the series B except the Gd interlayer which is used to control the effective work function of the FM layer as described in chapter 2. Curve C in Fig. 4.1 shows the I - V curve characteristics of FM/ Gd (3.0 nm)/ Al_2O_3 (0.5 nm)/ Cs/ Si tunnel contacts. This curve appears almost symmetric with a negligible Schottky barrier height. The I - V characteristics of the contacts in series C depend on the barrier thickness as well as the Gd thickness. Fig. 4.2(a) shows the influence of the Al_2O_3 barrier thickness on the I - V characteristics, which indicates the decrease of the current density with increasing the barrier thickness. This means that transport is dominated by the tunneling through Al_2O_3 . Surprisingly, however, we find inverted diode characteristics—the current density in the reverse bias range is higher than that in the forward bias range—in the FM/ Gd (3.0 nm)/ Al_2O_3 / Cs/ Si tunnel contacts with a thick Al_2O_3 barrier. We have investigated the influence of the Gd thickness as shown in Fig. 4.2(b). The FM/ Gd (x nm)/ Al_2O_3 (2.0 nm)/ Cs/ Si tunnel contacts with no Gd layer and a thin Gd layer ($t_{\text{Gd}} \lesssim 0.5$ nm) shows normal I - V characteristics, but the tunnel contacts with a thick Gd layer ($t_{\text{Gd}} \gtrsim 0.7$ nm) reveals an inverted diode characteristic.

In order to investigate the effect of the Cs deposition on the Schottky barrier height, we have used the method as described in chapter 2, section 2.5.5; we can determine the charge neutrality level and the surface density of the gap states if we measure the Schottky barrier height versus the effective work function of an FM electrode, using the relation between the effective work function and Gd thickness (see Eq. 2.5 in chapter 2, section 2.5.5.). We have measured the Schottky barrier height of the FM/ Gd (x nm)/ Al_2O_3 (2.0 nm)/ Cs/ Si tunnel contacts by varying the thickness of the low work-function Gd interlayer. Fig. 4.3(a) shows the Schottky barrier heights of the tunnel contacts plotted as a function of the effective work function of the FM/ Gd (x nm) layer. From a linear fit using Eq. 2.3, we have obtained two coefficients for the Cs-deposited Si: $a = 0.172$ and $b = -0.175$ (for the normal Si surface: $a = 0.426$ and $b = -1.321$). Comparing this result with Eq. 2.1 and Eq. 2.2 in chapter 2, we obtain the surface density of gap states and the charge neutrality level; the surface density of gap states (D_s) = 1.2×10^{18} states/ m^2/eV and the charge neutrality level (ϕ_{CNL}) = 1.0 eV (for the normal Si surface, $D_s = 4.5 \times 10^{17}$ states/ m^2/eV and $\phi_{\text{CNL}} = 0.41$ eV). Fig. 4.3(b) shows the schematic energy diagram of the charge neutrality level located at ~ 1.0 eV above the valence band maximum. In this calculation, we assume the effect of Cs on the electron affinity of Si is very small, which can be inferred from

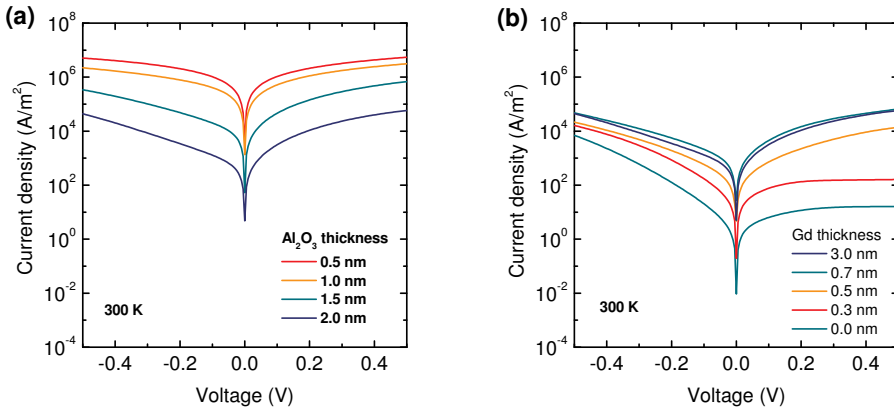


Figure 4.2. (a) I - V curves of Si/ Cs/ Al_2O_3 (0.5~2.0 nm)/ Gd (3 nm)/ $\text{Ni}_{80}\text{Fe}_{20}$ (10 nm) /Au (10 nm) tunnel contacts with various Al_2O_3 thickness. (b) I - V curves of Si/ Cs/ Al_2O_3 (2.0 nm)/ Gd (0~3 nm)/ $\text{Ni}_{80}\text{Fe}_{20}$ (10 nm) /Au (10 nm) tunnel contacts with various Gd thickness. The thickness of the Al_2O_3 insulator obtained from the TEM experiment is 2.0 nm (see Fig. 2.4 in chapter 2; the oxidation time for Al_2O_3 was 7.5 min.) The positive voltage corresponds to the electron transport from metal to Si, and the negative voltage to the electron transport from the Si to metal.

the experiment with series A; we used an insulator thickness of 2.0 nm determined from TEM experiment.

From this result, we find that (i) the Cs deposition makes a huge change in the charge neutrality level from 0.4 eV (Fig. 2.17 in chapter 2) to 1.0 eV; (ii) the density of the gap states has been increased three times due to the presence of the Cs at the Si surface in the Si/ Cs/ Al_2O_3 (2.0 nm)/ FM contact. The measured charge neutrality level is in good agreement with the alkali-metal-induced interface states observed in the photoemission experiments in Ref. [90]; they have shown that alkali metals like K or Cs deposited on Si surface give rise to localized interfacial states at about 0.1 eV below the conduction band minimum. As a consequence, the lowering of the Schottky barrier by Cs deposition in Si/ Cs/ Al_2O_3 contacts is because the Cs affects the surface density of the gap states and the charge neutrality level at the Si interface; and the Fermi energy level in Si is strongly influenced by the alkali-metal-induced interface states at ~ 1.0 eV above the valence band edge.

The results described above present a very effective way to reduce the Schottky barrier height in spin-tunnel contacts to Si and to obtain near zero Schottky barrier height with an ultrathin (about 0.5 nm) low work-function

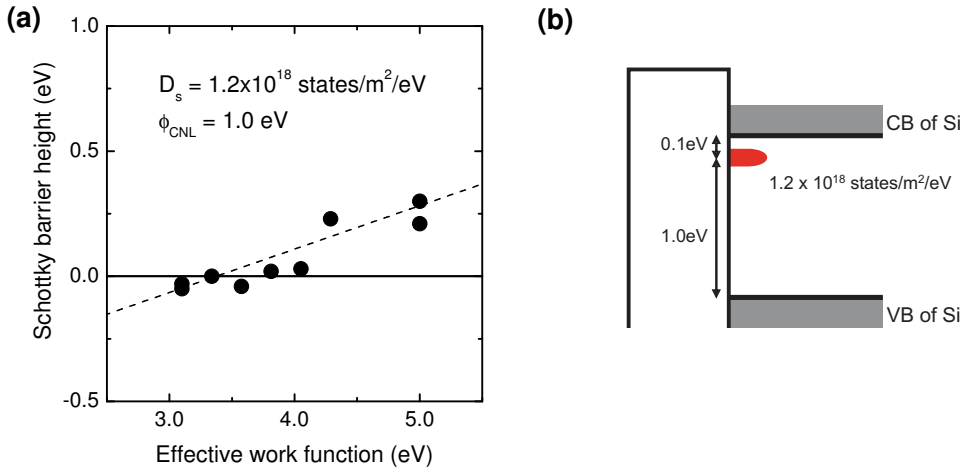


Figure 4.3. The Schottky barrier height of Si/ Cs/ Al_2O_3 (2.0 nm)/ Gd (0~3 nm)/ $\text{Ni}_{80}\text{Fe}_{20}$ (10 nm) /Au (10 nm) tunnel contacts as a function of the effective work function of the metal layer as determined by the Gd thickness. The dashed line is a linear fit using Eq. 2.3 to determine the density of gap states and the position of the charge neutrality level. The positive voltage corresponds to the electron transport from metal to Si (reverse bias), and the negative voltage to the electron transport from the Si to metal (forward bias). (b) Schematic energy band diagram of a MIS contact with Cs-deposited n-type Si. The charge neutrality level is depicted in red.

interlayer. Because the Fermi energy level is very close to the conduction band edge, we are able to obtain a low Schottky barrier height even with high work-function FM materials in FM/ Al_2O_3 (2.0 nm)/ Cs/ Si tunnel contacts. These results are very useful to inject spin polarized carriers into Si, unless the Cs deteriorates the spin information. With the Cs deposition on the Si surface, a smaller Gd thickness is required to obtain the desired RA product in comparison with normal Si surface, such that the TSP is expected to be higher.

Figure 4.4(a) shows the temperature dependence of the I - V characteristics of Si/ Cs/ Al_2O_3 (2.3 nm)/ Gd (0.8 nm)/ $\text{Ni}_{80}\text{Fe}_{20}$ (10 nm) / Au (10 nm). In Fig. 4.4(a), the positive voltage corresponds to the electron transport from metal to Si (reverse bias), and the negative voltage to the electron transport from the Si to metal (forward bias). Surprisingly, the current level in the reverse bias remains the same with decreasing temperature, while the current level in the forward bias decreases slightly. This is opposite to what we have

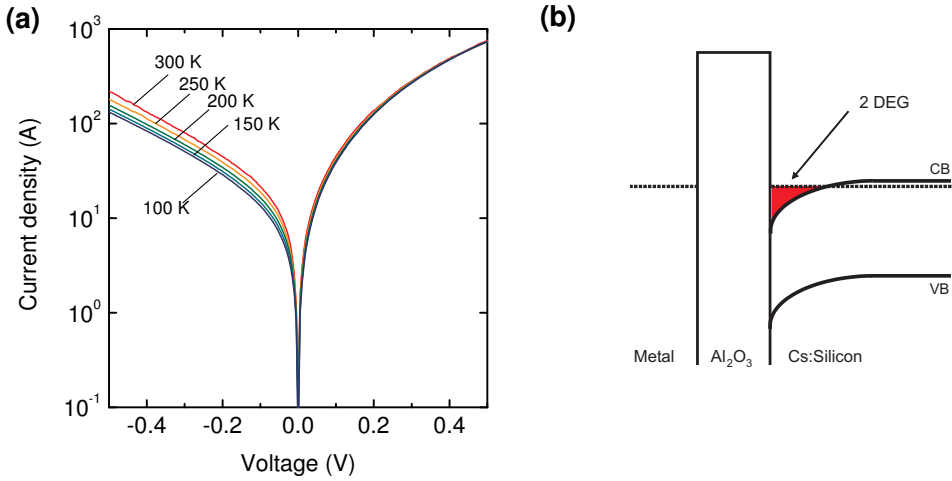


Figure 4.4. (a) Temperature dependence of the I-V characteristic of a Si/Cs/Al₂O₃ (2.0 nm) / Gd (0.8 nm) / NiFe (10 nm) / Au (10 nm) contact. The positive voltage corresponds to the electron transport from metal to Si, and the negative voltage to the electron transport from the Si to metal. (b) Schematic energy band diagram of a MIS contact with Cs-deposited n-type Si surface, which depicts an inverted band bending near the contact and the presence of an accumulation layer at the n-type Si surface

observed in Si/ Al₂O₃/ FM contact with the normal Si surface (see Fig. 2.15 in chapter 2 as an example for comparison). This means that the polarity of the diode has been reversed; the band bending at the interface of this contact as depicted in Fig. 4.4(b) is also opposite to the conventional case (see Fig. 2.1 in chapter 2 as an example). If this band bending is large enough and the Fermi energy level inside Si is close to the conduction band minimum, an accumulation layer might be developed at the surface. This opens a possibility that one can realize a two-dimensional electron gas channel at the n-type Si.

4.4 Conclusions

We have presented a surprisingly effective way to control the RA product of the FM/ Al₂O₃/ Si contacts using an alkali-metal (Cs)-covered Si surface. The spin tunnel contacts to Si with an alkali-metal-coated n-type Si surface show noticeably low Schottky barrier height. We find that the Cs deposition on Si induces three times larger density of gap states, with a charge neutrality level

very close to the conduction band edge of Si. Because of these gap states, the Fermi energy level in Si is close to an alkali-metal-induced surface state level, providing a low Schottky barrier height. By combining this new method with the low work-function approach developed in the previous chapter, we can control the RA product of spin tunnel contacts to Si over a wide range as well as potential energy profile of spin tunnel contacts to Si. Cs deposition on the Si surface represent an alternative method to engineer spin-tunnel contacts to obtain the desired RA product of spin tunnel contacts with a smaller Gd thickness in comparison with normal Si surface, such that the TSP is expected to be higher.

Even more surprisingly, an inverted diode characteristic has been observed in FM/ Gd/ Al_2O_3 / Cs/ Si contacts. This indicates an inverted band bending near the contact and the presence of an accumulation layer at the n -type Si surface. This suggests the formation of two-dimensional electron gas at the n -type Si surface, which is useful to design new devices using the properties of the two-dimensional electron gas.

Chapter 5

Magnetic properties of nano-scale magnetic elements

This chapter is devoted to the magnetic properties of nano-scale magnetic elements. Nano-scale magnetic elements are fabricated using laser interference lithography (LIL) and lift-off technique, and their magnetic properties are characterized using magnetometry and magnetic force microscopy. We study the influence of the size and shape of the elements on their magnetic configuration, and discuss the possibility to obtain almost uniform magnetization in the magnetic elements. We investigate the magnetostatic interaction among the magnetic elements that are densely packed at a length scale of 100 nm. The knowledge obtained from these studies can be applied to design the source and drain contacts of the spin-MOSFET as well as to understand the spin transport in the ferromagnetic element less than 100 nm in size, which is also relevant for the spin-transfer torque devices.

5.1 Introduction and motivation

Nano-scale magnetic elements are of practical importance, because of the possible applications in patterned recording media, spin-transfer torque devices, and MRAMs. It is indispensable to understand the magnetic switching and magnetostatic coupling in arrays of magnetic elements for the applications. For example, a higher switching field of the magnetic elements may imply

more power consumption of the device, or the magnetic instability may result in a loss of information.

The major aim of this chapter is to study the scaling behaviour of the nano-scale magnetic elements and the magnetostatic interaction between them. The magnetic properties of nano-scale magnetic elements is closely related with the size and shape of the elements. As the size of the magnetic element decreases, the element shows different micro-magnetic behaviors from multi-domain state to single domain state as shown in Fig 5.1. The magnetic elements with a few micron lateral dimensions show complex magnetic structures such as multi-domains and domain walls[91]. The magnetic dots with intermediate size (100 nm \sim 1 μ m) have a less complex magnetic configuration such as a vortex structure. In this range, the micromagnetic simulation is a powerful tool to understand the magnetic behavior of the nano-scale elements[92]. The magnetic elements smaller than 100 nm show much simpler magnetic behavior such as flower state, c-state, and s-state, which follows roughly the classical Stoner-Wohlfarth model[93–96]. We shall investigate the scaling behavior of magnetic properties of nano-scale elements. The magnetostatic interaction between the magnetic elements is also one of our concerns in the densely packed arrays.

Understanding magnetic properties of nanoscale magnetic elements and the magnetostatic coupling in closely-packed nanoscale elements is also relevant for the spin-MOSFET. It is very important to control the magnetic properties of the spin injector and detector of the spin-MOSFET, because the spin information injected to Si is based on their magnetization. The magnetostatic interaction among the magnetic elements that are densely packed at a length scale of 100 nm is also related to design the distance between magnetic structures in a spin-MOSFET.

In order to characterize the magnetic properties of the nano-scale magnetic elements, we use two characterization tools, vibrating sample magnetometer (VSM) and magnetic force microscope (MFM). These two tools are complementary each other. In order to study scaling behavior as well as the magnetostatic interactions of magnetic elements, we need to measure the magnetic moment of the element. The VSM measurement provides quantitative, but averaged information of many identical elements. By contrast, the MFM enables us to observe individual elements with high resolution and sensitivity, but the information is qualitative.

The mainstream technology to produce nano-scale elements may be the

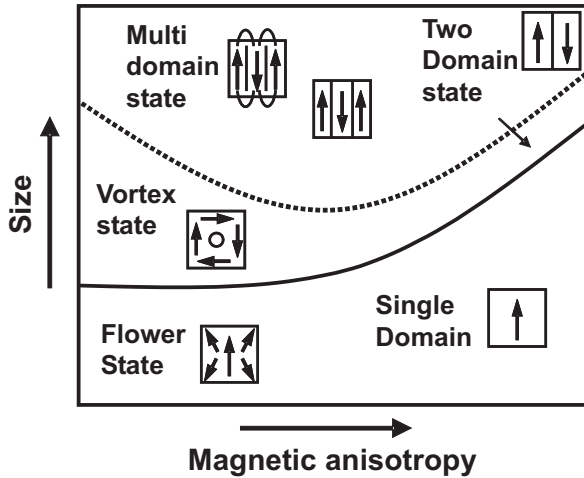


Figure 5.1. Calculated phase diagram of various magnetic states of square nano-scale elements[91]. The size and the magnetic anisotropy increase in log scale along the arrow direction.

optical projection lithography using deep-ultraviolet (DUV) light sources, high numerical aperture lenses, and step-and-repeat exposure tools[97]. For laboratory experiments or prototype manufactures, the scanning electron beam lithography provides high resolution and versatility to realize sub-100 nm patterns with arbitrary shapes. Nevertheless, there are also alternative lithographic techniques with special advantages; the interference lithography is one of them. The interference lithography can be used to fabricate nano-scale magnetic elements, if a large number of identical magnetic elements are needed to characterize their properties using a magnetometer. Interference lithography is a maskless technique suitable for fabricating two-dimensional periodic arrays of the identical patterns over large area in a couple of exposures [95, 98, 99]. We have used the interference lithography because this allows a fast fabrication of the magnetic element array, but we may rely on the optical projection lithography or the scanning electron beam lithography for the real fabrication of the spin-MOSFET.

Section 4.2 describes the fabrication of nano-scale magnetic elements using laser interference lithography and lift-off technique. Section 4.3 describes the characterization of the magnetic properties of various nano-scale magnetic elements using VSM and MFM. We shall discuss the magnetic switching behavior of the structure as well as the magnetostatic interaction between the

magnetic elements in the densely packed arrays. The measured results are analyzed using micromagnetic simulations.

5.2 Fabrication of nano-scale magnetic elements

The fabrication of nano-scale magnetic elements involves lithography and pattern transfer processes. In this section, we describe the basic principles of laser interference lithography and the lift-off technique. Some examples such as photoresist patterns and magnetic dot arrays fabricated by this process will be presented at the end of this section.

5.2.1 Laser interference lithography using image reversal technique

Laser interference lithography is based on the interference of two coherent light beams, as shown in Fig. 5.2, which constructs a sinusoidal standing wave pattern of light on a substrate [95, 98–100]. The exposure of this interference pattern produces line images (Fig. 5.3(a)) in the resist with a period of $\lambda / 2\sin\theta$, where λ is the wavelength of the light, and θ is the half angle of intersection of two laser beams. The change of the intersection angle allows us to control the period of pattern over a wide range. Half wavelength of the light, $\lambda/2$, is roughly the minimum period of the line pattern that can be attained by the interference lithography. For instance, light beams with a wavelength of 266 nm with an incidence angle of 60° produce a line pattern with a period of 150 nm.

Two coherent beams are needed to conduct interference lithography. Ref. [101] describes the details of the LIL system we have used. The laser beam is generated from a Nd:YAG laser. The frequency of the laser beam is doubled twice to obtain a DUV wavelength of 266 nm, and the beam is collimated and expanded until it reaches a Lloyd mirror. On the substrate surface, the laser beam—that directly comes from the source—interferes with the other beam reflected at the mirror. We can control the period of the interference pattern by changing the angle between the substrate and the mirror. Fig. 5.3(a) shows the interference pattern we can obtain on the substrate.

Two-dimensional patterns can also be obtained from a superposition of

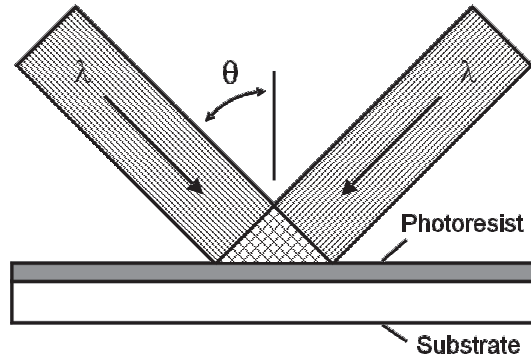


Figure 5.2. Simplified schematics of laser interference lithography[98]. λ is the wavelength of the light, and θ is the half angle of intersection of two laser beams.

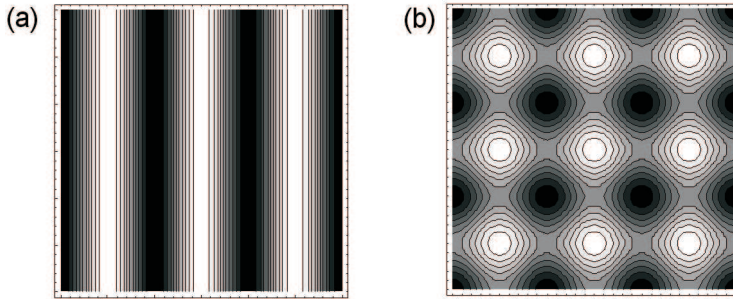


Figure 5.3. (a) Computed interference pattern with single exposure. (b) Computed interference pattern obtained from a superposition of two successive exposures with 90° rotation of the substrate

two successive exposures. After the first exposure of an interference pattern, we rotate the substrate by an angle ϕ , and illuminate the interference pattern again. The total intensity (I) of the exposure at a point (x, y) on the substrate is given by

$$I = A \sin^2\left(\frac{\pi}{a}x\right) + B \sin^2\left(\frac{\pi}{a}(x \cos\phi + y \sin\phi)\right), \quad (5.1)$$

where A and B are the intensity of the exposures, and a is the period of the interference pattern. Usually, the intensity of the two exposures is the same ($A = B$) to get symmetric image patterns. If the angle ϕ is 90° , the image defined by the contour line at the minima or maxima is circular (Fig. 5.3(b)); if $0^\circ < \phi < 90^\circ$, the feature becomes an elliptical shape with various long-

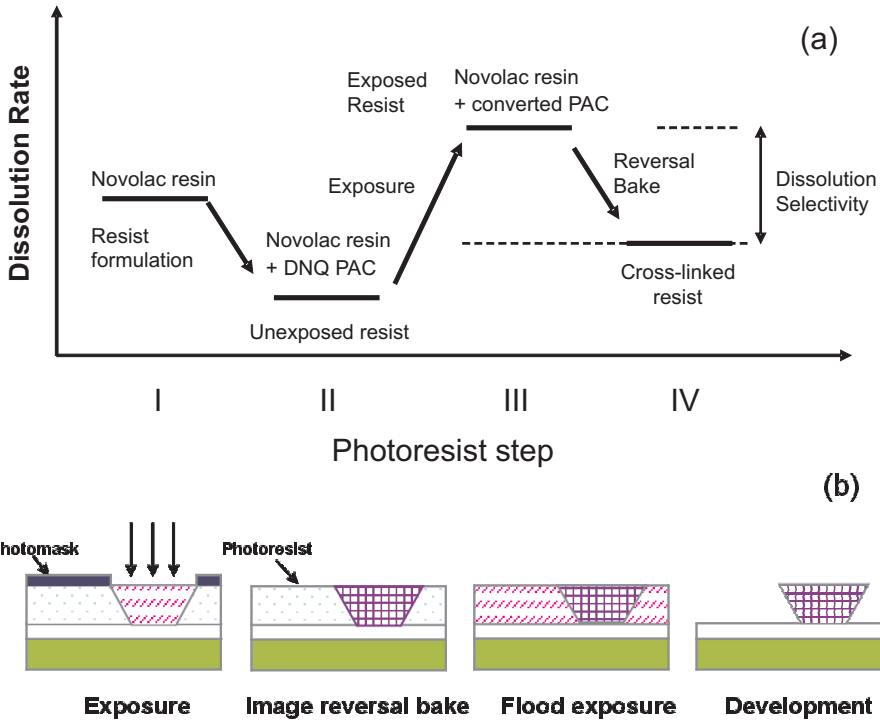


Figure 5.4. (a) Dissolution rate of the resist in image reversal process. (b) Process steps in the image reversal process.

axis-to-short-axis ratios depending on the angle ϕ . The image contrast of the interference pattern is defined as the modulation transfer function, $MTF = (I_{max} - I_{min}) / (I_{max} + I_{min})$, where I_{max} (I_{min}) are the intensity at the maxima (minima). It is important to choose a correct tonality of the resist to obtain a higher image contrast, since the MTF is higher when the critical features are imaged at the minima[99, 100]. Therefore, it is desirable to use negative resists to form an array of holes, while positive resists is suitable for forming an array of pillars. It has been shown that negative imaging on the negative resist or the image reversal resist with laser interference lithography is useful to fabricate the arrays of holes[99, 100, 102].

In this research, the image reversal technique is used to form hole arrays instead of pillar or post arrays, because the formation of holes enables us to use a lift-off technique to fabricate nano-patterns without any etching process. The image reversal technique is an interesting and useful trick based on the

reversal of resist tonality by a baking step after an exposure, so that it functions as a negative resist[103]. This process provides attractive advantages in a device fabrication. For example, this technique allows one to produce a negative or an overhang wall profile which is desirable for a metal lift-off process[103–105].

A conventional optical photoresist consists of three-components: a resin, a photoactive compound, and a solvent[103–105]. Many high-resolution positive resists are based on a hydrophobic diazonaphoquinone sulfonate ester inhibitor in a base-soluble *Novolac* resin matrix. In order to get the image reversal properties, another component is required such as a crosslinking agent. The role of the agent is to induce a crosslinking of the resin, and thereby to reduce the dissolution rate.

Figure 5.4 shows the dissolution rate of the photoresist during the image reversal process[103–105]. Initially, the dissolution rate of the *Novolac* resin is quite high (Step I). The diazonaphoquinone photoactive compound (DNQ PAC: a sensitizer or an inhibitor) added to the *Novolac* resin (Step II) gives the resist its developer resistance and radiation absorption properties, resulting in a decreased dissolution rate. Exposure of light converts the properties of the photoactive compound in the photoresist. The carboxylic acid formed during exposure switches the resin from the hydrophobic to the hydrophilic, the long chain of the resin changes to shorter chain with small molecular weight, and the exposed resist shows a higher dissolution rate about several orders of magnitude (Step III). In order to get the image reversal properties, a baking step is required to activate the crosslinking agent, which induces a crosslinking of the resin, and reduces the dissolution rate of the resist. The increased molecular weight and hydrophobicity in the exposed regions lead to at least a 10-fold reduction in dissolution rate (Step IV), while the unexposed areas still behave like a normal unexposed positive photoresist. The exact chemistries associated with the image reversal step are described in the references[103–105].

Photoresist profile usually has a positive slope of $75^\circ \sim 85^\circ$ because the light penetrating through the resist layer is attenuated by the absorption of the photoactive compound[104]. This results in a higher exposure at the top of the resist and a lower exposure at the bottom of the resist. When a photoresist is processed in the image reversal mode, highly exposed areas in the first exposure is cross-linked to a higher degree than those with lower dose in the reversal bake step. As a consequence, the dissolution rate is higher at the

bottom of the resist, and the dissolution rate is lower at the top of the resist. The final result is negative wall profile ideally suited for lift-off process (See Fig. 5.4(b)).

We have used TI series photoresists (Microchemicals GmbH)[106] which contain a crosslink agent. The basic process steps of the image reversal technique are depicted in Fig. 5.4(b)[106].

- (1) Spin coating and the soft bake of the photoresist.
- (2) **Exposure** with an inverted pattern: a chemical change occurs in the exposed area of the photoresist.
- (3) **Image reversal bake**: the cross-linking of the *Novolac* resin takes place in the exposed area in step 1.
- (4) **Flood exposure**: a dissolution rate increases in the exposed area except the cross-linked area.
- (5) **Development**.

The pattern exposed to the light in the process step (2) and baked in process step (3) remains at the end with a negative sidewall profile. The shape of negative wall profile depends on the first exposure dose, the reversal bake temperature and time, and the development time. Higher first exposure dose results in a reduced under cut, so does higher reversal bake temperature or time. Longer development time promotes an increased undercut.

5.2.2 Pattern transfer using lift-off process

The fabrication of nano-scale magnetic element involves pattern transfer processes, which reproduce a real material structure using the features on the photoresist with high fidelity. There are two different kinds of pattern transfer processes, etching process and lift-off process[107].

Many nano-scale patterns are usually transferred using the etching technique. This process usually begins with a deposited thin film stack. The resist pattern is formed by lithography to define an etch-mask on top of the film stack, and the film stack is etched using this etch-mask. The major disadvantage of this approach is that a etch process, such as ion beam etching and

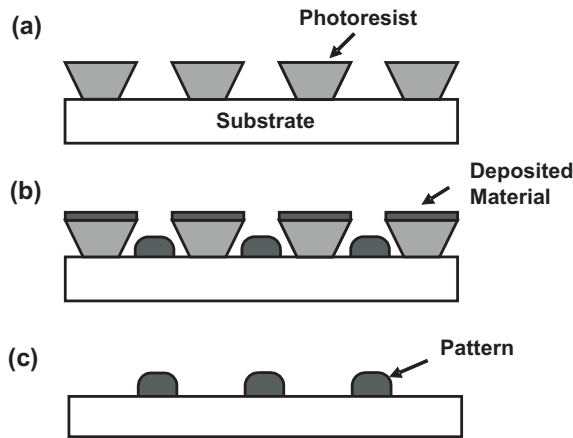


Figure 5.5. Schematic diagram of the lift-off process. (a) the photoresist pattern after the development, (b) the material pattern after deposition, and (c) the material pattern after the lift-off.

reactive ion etching, can cause side effects such as edge damage, faceting, trenches, and the side-wall redeposition[108].

For the lift-off technique (Fig. 5.5), the resist pattern is formed first, and deposition of the thin film layer stack is followed. The real pattern is formed by dissolving away the resist and then "lift-off" the unwanted material[107]. This technique also has the disadvantages; the deposited features with the lift-off technique are in the shape of truncated cones with rounded edges because of the shadowing effect; the technique is limited to temperature below 200~300 °C, at which point resist begins to degrade[107].

In this research, we have used the lift-off process to fabricate nanoscale elements. Figure 5.6 shows the resist patterns of circular holes with different dimensions. We have varied the period of the interference pattern and the exposure condition to control the hole size of the resist pattern. We are able to fabricate resist holes with a diameter of 620 nm to 170 nm by varying the period from 1000 nm to 300 nm.

The elliptical shape is useful to obtain the shape anisotropy of a magnetic element. It is possible to fabricate an elliptical shape by LIL. For circular patterns, we use 90° rotation from the first exposure to the second exposure. For elliptical patterns, we can control the long-axis-to-short-axis ratio by changing the rotation angle between two exposures. Figure 5.7 shows the intensity profile of the interference image pattern with different angle ϕ between the

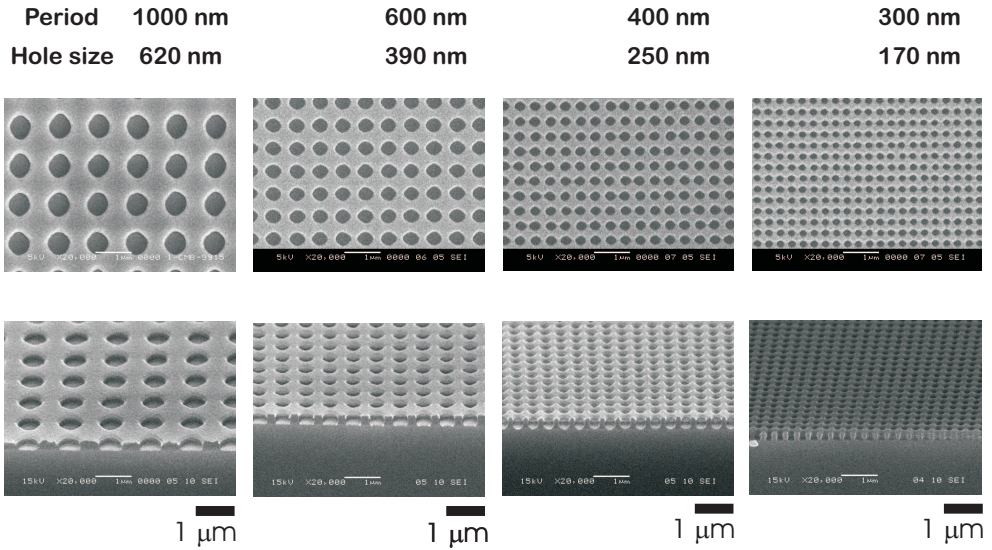


Figure 5.6. SEM images of the resist patterns with circular holes with different dimensions, Top row: top view, bottom row: side view.

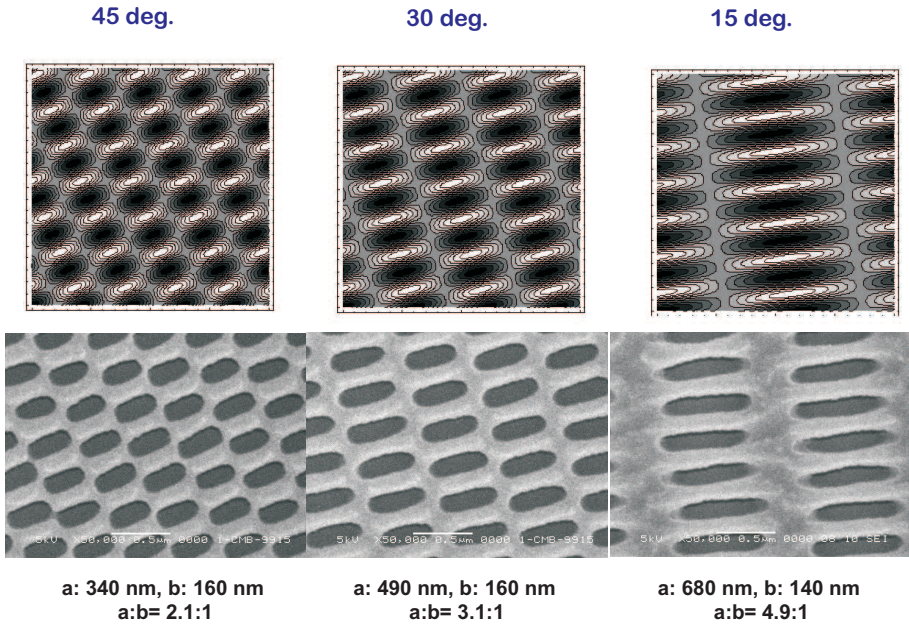


Figure 5.7. Top: calculated laser intensity pattern with different angles (45°, 30°, and 15°) between the first and second exposure). Bottom: SEM images of the resist patterns with elliptical holes with different long-axis-to-short-axis ratios. The white line in the SEM images is 0.5 μm length scale.

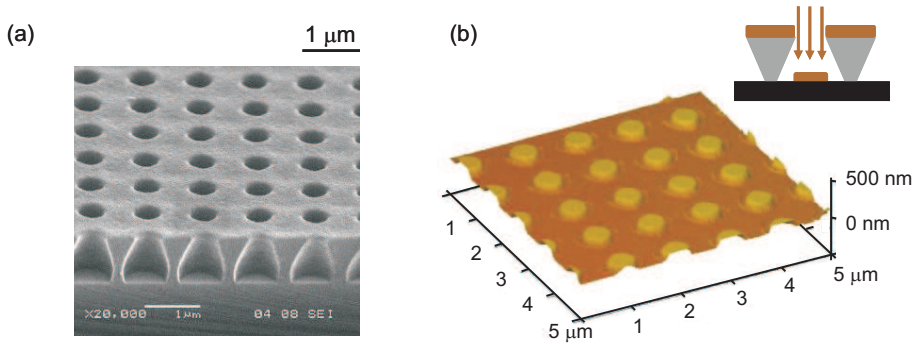


Figure 5.8. (a) SEM image of a photoresist pattern produced by combining LIL and image reversal technique. The shape of the PR has an overhang structure suitable for a lift-off process. (b) AFM image of Co-dots fabricated using the above photoresist pattern. The diameter of the Co dot is 500 nm and the thickness of the Co dots is 100 nm.

first and the second exposures. Using this light intensity profile, we have obtained the photoresist patterns with a long-axis-to-short-axis ratio of 2:1, 3:1, 5:1 by using 45° , 30° , and 15° rotations respectively (Fig. 5.7). The length in short axis direction is roughly 160 nm. The resist pattern with a 90° rotation are in the square array, but the pattern with $0^\circ < \phi < 90^\circ$ are in oblique array.

Figure 5.8(a) shows an SEM image of a photoresist pattern produced by combining LIL and image reversal technique. This resist pattern is used as a shadow mask for Co deposition. The shape of the photoresist has an overhang structure suitable for the lift-off process. We have deposited Co by e-beam evaporation through the resist mask to obtain Co dot arrays. Figure 5.8(b) shows an AFM image of Co-dots fabricated using the above photoresist pattern. The diameter of the Co dot is 500 nm, and the thickness of the Co dots is 100 nm.

5.3 Characterization of nano-scale magnetic elements

In this section, we characterize the magnetic properties of the nano-scale elements fabricated by LIL and lift-off technique. We start from a circular pattern with a diameter of 500 nm, and reduce the size of the circular pattern down

to 150 nm. We analyze magnetostatic interactions between the magnetic elements in the densely packed arrays. Nano-scale elements with an elliptical shape are studied at the end.

5.3.1 Vortex structure in circular nano-scale elements

In order to characterize the magnetic properties of the circular Co-dots with 500 nm diameter (Fig. 5.8) described in the previous section, we have measured M - H hysteresis loops of the sample using VSM. By the benefit of the LIL process, we are able to fabricate enough number of almost identical magnetic elements on the wafer to get a large signal in the VSM measurement. Fig. 5.9 shows the measured M - H hysteresis loop with in-plane magnetic field. The hysteresis loop didn't show any in-plane anisotropy, and the out-of-plane direction was found to be magnetic hard axis. The M - H hysteresis loop measured by VSM (Fig. 5.9) displays the typical vortex characteristics.

When the magnetic field is applied to the ferromagnetic particle larger than a few micrometers, and then the field is reduced, the single-domain state is energetically unfavorable in remanent state because of the large self magnetostatic energy. In order to reduce this huge magnetostatic energy, ferromagnetic particles usually form multi-domain structures separated by domain walls. The formation of the domain wall is associated with additional energies, the exchange energy and the anisotropy energy. As the size of the magnetic elements decreases, this additional energy for the domain wall formation becomes too large. For a nano-scale magnetic element such as the circular dot with 500 nm diameter, the continuous variation of the magnetic moment takes place inside the element instead of the formation of the domain walls. The magnetic moment in the nano-scale elements changes gradually from one point to another to avoid free magnetic poles at the edges and not to increase the exchange energy, showing a curling in-plane magnetic configuration of the magnetic moment. This is known as a magnetic vortex structure[91, 110, 111]. In the center of the elements, if the magnetic moment remains in plane, the angle between adjacent magnetic moment becomes too large to keep the exchange interaction minimum. The energetically stable state is a magnetic structure of which the magnetic moment near the center is perpendicular to the plane. This is known as the core of the vortex structure[91, 110, 111].

We have investigated the magnetic structure of the Co-dots with 500 nm

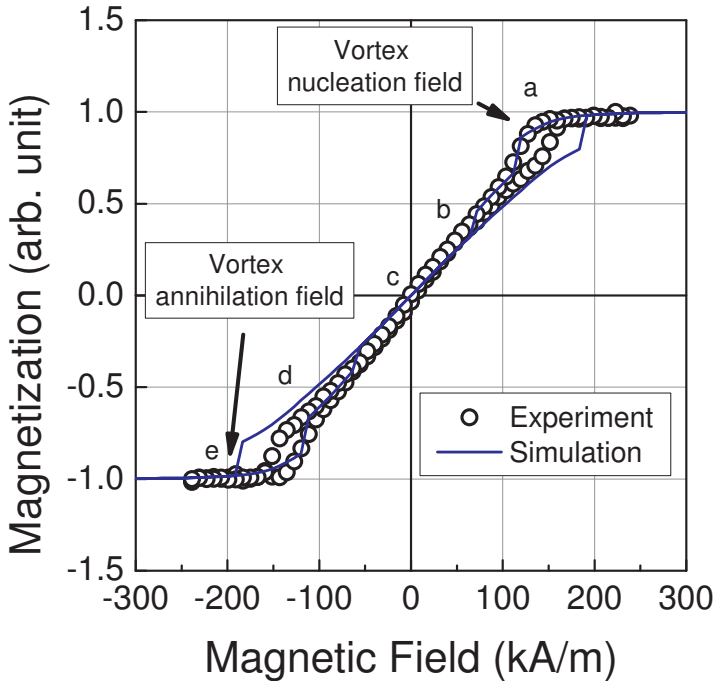


Figure 5.9. M - H hysteresis loops of the Co dot array with a diameter of 500 nm and a thickness of 100 nm. The applied field direction is in-plane. Open circles are the measured data using VSM. The solid line is the simulated result for the comparison.

diameter using MFM. The MFM uses a magnetic tip with a magnetic dipole moment formed at the end of the cantilever[109]. The force on the magnetized tip is detected by measuring the displacement of the end of the cantilever or its mechanical resonance frequency, which is determined by the spring constant of the cantilever and the vertical component of the force gradient. If there is a stray field from a magnetic sample, the resonant peak of the cantilever shifts. In the MFM, the shift of the resonant peak in the frequency domain is measured, as the tip scans a sample surface.

Figure 5.10 shows the magnetic structure of four Co dots in remanent state. The color code represents the frequency shift of the MFM resonance peak which implies a magnetic interaction between the MFM and the sample. The red color indicates that the MFM tip detects an attractive interaction, and the purple color indicates that the tip detects a repulsive interaction. We can clearly observe the vortex core structure at the center of the circular dots in

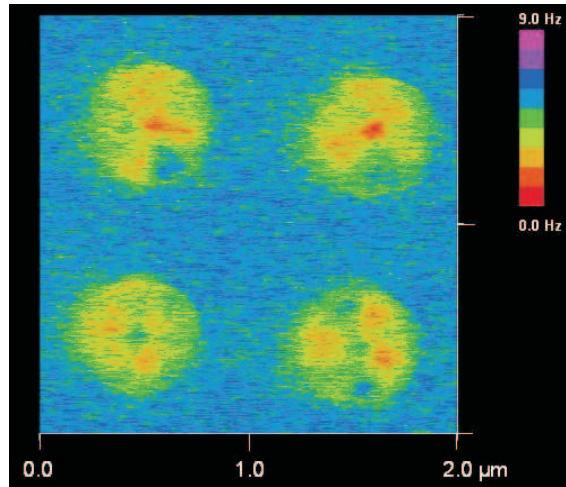


Figure 5.10. MFM image of Co-dots with a diameter of 500 nm and a thickness of 100 nm. The color code indicates the frequency shift of the MFM resonance peak explained in the text.

Fig. 5.10. The magnetization direction at the center of two upper dots is opposite to the magnetization of the tip; by contrast, the magnetization direction at the center of the bottom two dots is the same as the magnetization of the tip. We believe that the small color variation inside the dot is owing to the inhomogeneity of the vertical component of the magnetization originated from the shape of the dot that is slightly different from a perfect circle.

We have conducted a micro-magnetic simulation using the OOMMF code [112] to compare the measured VSM result with the simulation and to understand the behavior of the magnetic vortex structure in a magnetic field. In this simulation, we treat the Co dot as a perfect disc with a diameter of 500 nm and a thickness of 100 nm without any defects and without any in-plane or out-of-plane magnetic anisotropy. The bulk magnetization value of cobalt is 1.4×10^6 A/m, and the exchange stiffness of Co is 3×10^{-11} J/m, which are provided by the OOMMF code[112]. The length of the cubic cell is 5 nm in the computation, which is almost similar to the exchange length of Co (4.9 nm). As shown in the Fig. 5.9, the $M-H$ hysteresis loop computed by this simulation is in good agreement with that of the measured experimental result. Fig. 5.11 shows three circles which correspond to the magnetic structures of the top, center, and bottom slices of the Co disc, respectively. In these

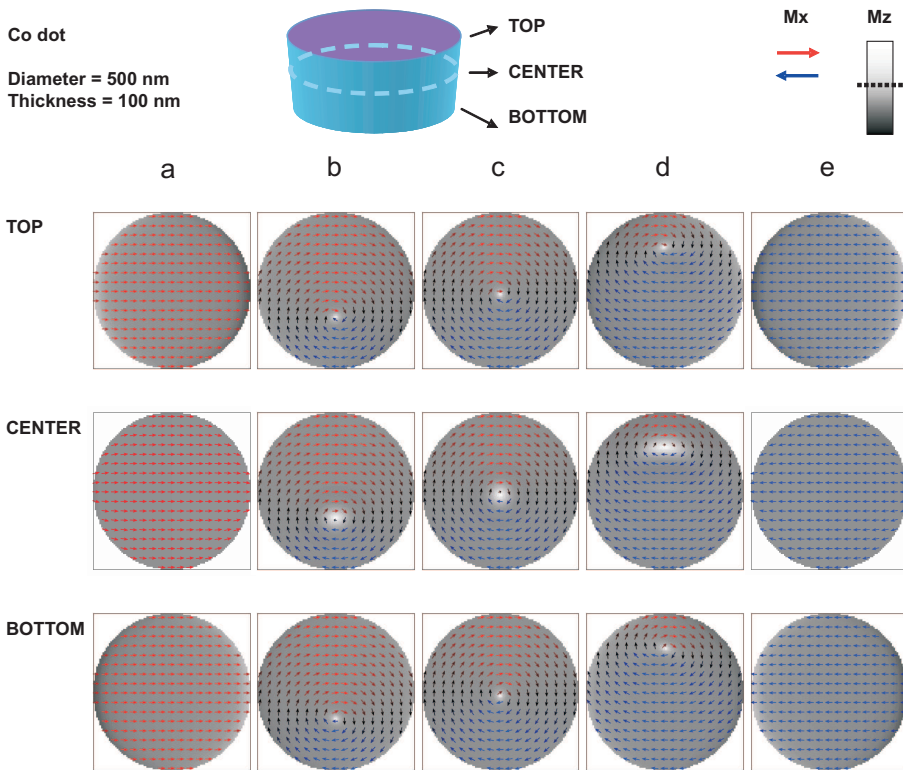


Figure 5.11. Micromagnetic simulation of a Co-dot with a diameter of 500 nm and a thickness of 100 nm at five different points, a-e, in the M - H hysteresis loop (Fig. 5.9). Three circles at each point correspond to the magnetic structures of the top, center, and bottom slices of the Co disc, respectively. The arrows represent the direction of the magnetic moment in the xy plane, and the gray scale represents the vertical component of the magnetic moment.

figures, the arrows indicates the direction of the magnetic moment in the xy plane, and the gray scale represents the perpendicular (z) component of the magnetic moment. Initially, at the very high in-plane magnetic field (point a), the magnetization is saturated in plus x -direction. As we decrease the field, the vortex is nucleated to reduce the magnetostatic energy at some point, and it moves to the center of the dots (point b). At the remanent state, the vortex is located at the center of the circle (point c). As we increase the in-plane magnetic field further in the negative direction, then the vortex moves to the other side of the circle (point d), and the vortex annihilates at some point (point e) to form a uniform magnetization in the entire element.

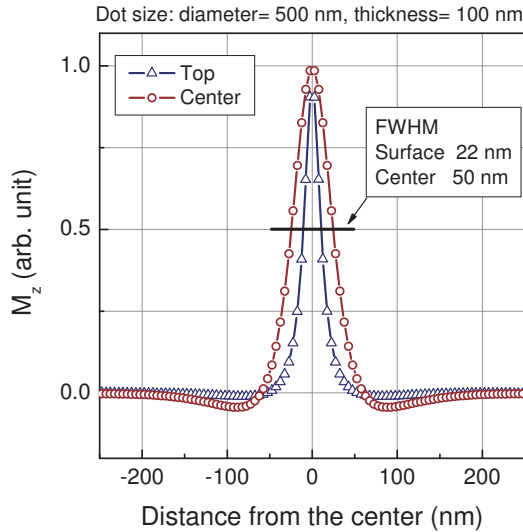


Figure 5.12. Vertical component of the magnetization of the 500-nm Co dot in the vortex state obtained from the simulation. The size of the core at the top surface and in the middle of the dot are shown. The result for the bottom surface of the dot is similar to that of the top surface.

The size of the vortex core can be defined as the full-width at the half maximum of the vertical component of the magnetization. Fig. 5.12 depicts the vertical component of the magnetization of the 500-nm Co dot in the vortex state obtained from the simulation. The size of the vortex core at the surface (22 nm) is smaller than the size of the vortex core at the vertical center of the Co disc (50 nm), which is also in good agreement with the theoretical expectation[91]. This magnetic vortex core structure can be used to determine the spatial resolution of the magnetic microscopy techniques such as spin-polarized scanning tunneling microscopy[111] and ballistic electron magnetic microscopy[113].

5.3.2 Inter-dot magnetic coupling in densely packed arrays

When the length scale of a magnetic element is reduced to a critical size, the expense of the exchange energy exceeds that of the magnetostatic self energy in a multi-domain or a vortex structure. Below this critical size, the magnetic element prefers to have a uniform magnetic moment or a single domain in

the entire element. A true single domain structure—which follows the classical Stoner-Wohlfarth model[93]—can be obtained only with the ellipsoid geometry. Nevertheless, it is known that the magnetic elements smaller than 100 nm reveals relatively simpler magnetic behavior close to a single domain particle such as flower state, c-state, and s-state, depending on the anisotropy energy[91, 94–96].

We have fabricated the circular magnetic Co dot array with 300 nm period. Fig. 5.13(a) shows the SEM image of the photoresist pattern, and Fig. 5.13(b) shows the SEM image of the deposited Co dots after the lift-off. The average diameter of Co dots is about 170 nm, and their thickness is 15 nm. We have measured the magnetization loop of the circular magnetic dot array with varying the in-plane magnetic field orientation in plane. Fig. 5.13(c) depicts the angle convention of the applied in-plane magnetic field in the measurement with respect to the array direction. Fig. 5.14 shows the magnetization loops of the circular magnetic dot array at four different angles, which reveal definitely non-vortex behavior with high coercivity. We find that this array shows in-plane four-fold anisotropy; the 45° and 135° direction are the magnetically easy directions in comparison with 0° and 90° direction. If we disregard this fourfold anisotropy, the shape of this hysteresis curve looks like the magnetization curve of single domain particles whose easy axes are distributed at random orientation as presented in the classical literature[93].

We have measured the M - H hysteresis curves with varying the in-plane magnetic field angle in smaller angular steps, and obtained polar plots of the squareness versus the field angle (Fig. 5.15(a))—where the squareness is defined by the ratio of the remanent magnetization to the saturation magnetization—and the coercivity versus the field angle (Fig. 5.15(b)). Both curves clearly show that the Co dot array has four-fold in-plane anisotropy with which magnetic easy axes are parallel to the diagonal direction of the array. In order to understand the origin of this fourfold in-plane anisotropy, we have measured M - H hysteresis loop of un-patterned film using VSM. These results are shown in Fig. 5.15 for the comparison. The un-patterned film has a uniaxial anisotropy induced during the growth of which magnetic easy axis is roughly 150° . This is a typical morphology-induced magnetic anisotropy that is known to be occur in the magnetic film evaporated from an oblique angle.[114, 115]. The coercivity of the unpatterned film is less than 2 kA/m, which is much smaller than the coercivity of the Co dot array (40 kA/m). Therefore, the growth-induced anisotropy of the unpatterned film cannot ex-

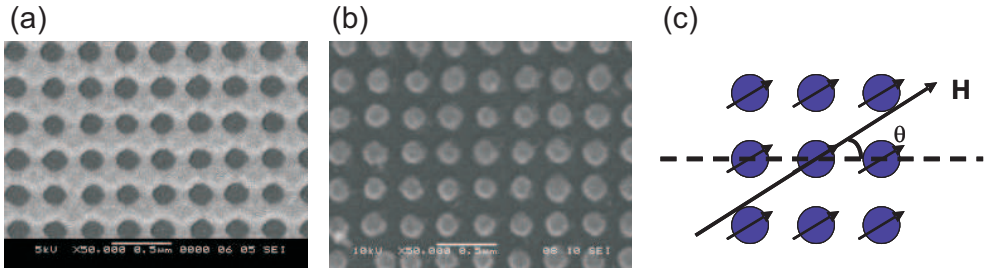


Figure 5.13. (a) SEM image of the photoresist pattern with circular holes, and (b) SEM image of the deposited Co dots after the lift-off. The average diameter of Co dots is about 170 nm, and their thickness is 15 nm. (c) the angle convention of the applied magnetic field with respect to the array direction.

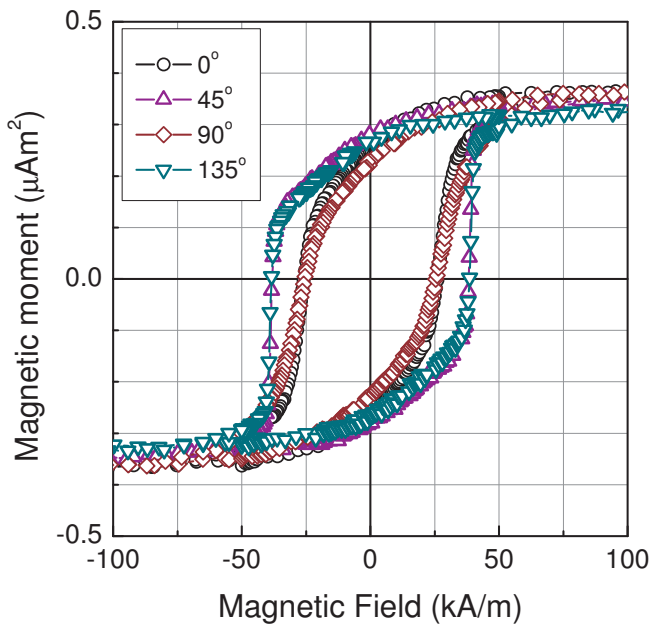


Figure 5.14. Magnetization loops of the circular magnetic dot array at four different angles. The applied field direction is in-plane. The angle convention of the in-plane applied magnetic field is shown in Fig. 5.13(c)

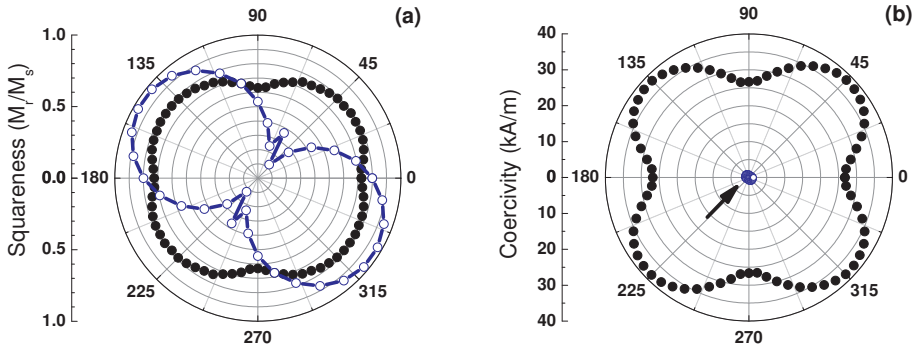


Figure 5.15. Polar plots of (a) the squareness of circular Co dots versus the field angle. (b) the coercivity of circular Co dots versus the field angle. Blue curves are the data for the un-patterned film. Please note the coercivity of the un-patterned film is less than 2 kA/m.

plain the four-fold in-plane anisotropy observed in the dot array.

When the dots in square array are completely magnetized in the external field direction, the magnetic dipoles in the completely magnetized dots make an inter-dot stray field in the direction of the magnetic moment of the dots. The magnetic stray field in other direction cancels out owing to the square array symmetry. The strength of the field (B) is determined by

$$B = \frac{\mu_0 \vec{m}}{4\pi a^3} \cdot \frac{1}{2} \sum_{\substack{j,k=-\infty \\ (j,k) \neq (0,0)}}^{\infty} \frac{1}{(j^2 + k^2)^{3/2}} = \frac{\mu_0 \vec{m}}{4\pi a^3} \cdot 4.51672, \quad (5.2)$$

where μ_0 is the permeability, \vec{m} is the magnetic moment of the individual dot, a is the period of the array pattern, and (j, k) are the integers. The strength of the field converges slowly as we add the contribution from the neighbors. The obtained result in Eq. 5.2 is similar to the results reported in Ref. [116], but we believe our value is more accurate, because we have added contribution not only from nearest neighbors but also from the square cells up to 30,000 cells. This strength of the inter-dot field in the Co dot array is quite substantial, ~ 6.4 kA/m, but this field is always in the same direction of the applied magnetic field. Therefore, this isotropic magnetic field cannot explain the fourfold in-plane anisotropy we have observed.

Other researchers have also observed the similar four-fold in-plane anisotropy

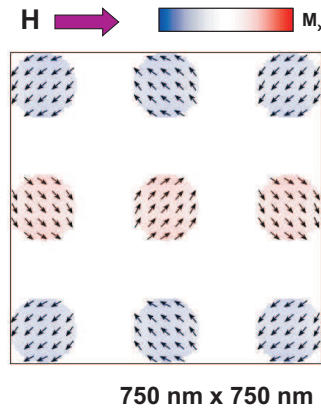


Figure 5.16. Micromagnetic simulations with nine Co dots in remanent state. In this simulation, the saturation in-plane magnetic field is applied parallel to the array axis, and then the field is reduced to zero. The arrows indicates the direction of the magnetic moments.

in square magnetic dots arrays [117–119] and six-fold in-plane anisotropy in the hexagonal array [120]. However, our results differ from their results in that our magnetization loop is similar to that of a single-domain structure, while their magnetization loops show vortex characteristics. Mathieu *et al.* [117] have found that the four-fold in-plane anisotropy in the square array is decreased as the magnetization increases [117]. This suggests that this four-fold in-plane anisotropy is closely related with the magnetic configuration of the dots in the unsaturated state. We have conducted micromagnetic simulations with nine Co dots in square array. Fig. 5.16 shows the result of the micromagnetic simulation with nine Co dots in remanent state. In this simulation, the saturation in-plane magnetic field is applied parallel to the array axis, and then the field is reduced to zero. We find that, at remanent state, the individual Co dots have almost uniform magnetic moment inside the dot, but the magnetic moments of each dot point toward different directions. Each Co dot prefers the magnetic moment direction parallel to the diagonal direction of the array. This configuration forms a global flux closure structure among the nearest neighbor dots, which is similar to the ground state of the square array of 4 single spins [121]. Heyderman *et al.* [122] have reported similar simulation results in a square arrays of circular dots with a smaller size, 50 nm. From this result, we understand that this four-fold in-plane anisotropy is originated from the inter-dot magnetic interaction from the neighbors in the square array

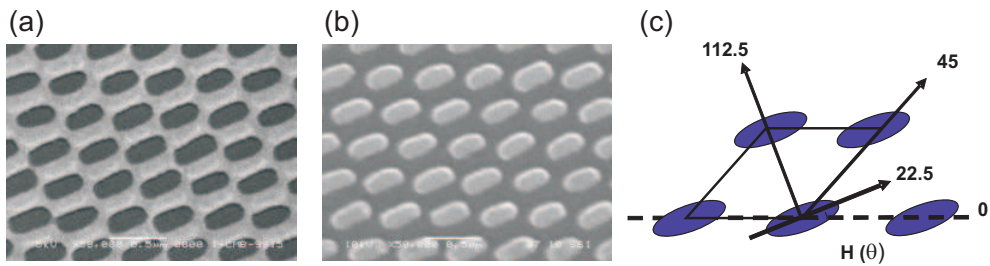


Figure 5.17. (a) SEM image of the photoresist pattern with elliptical holes, and (b) SEM image of the deposited elliptical Co dots after the lift-off. The long axis length of the Co dots is 340 nm, its short axis length is 160 nm, and its thickness is 15 nm. (c) the angle convention of the applied magnetic field with respect to the array direction. The magnetic easy axis direction is 22.5° .

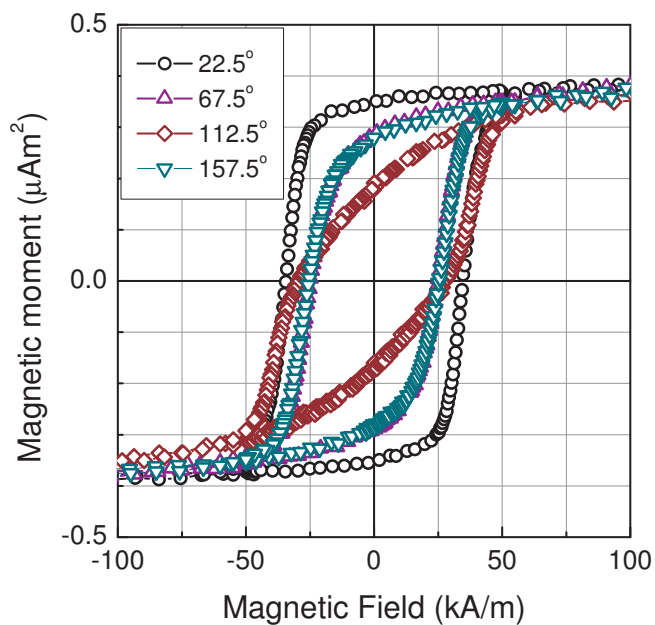


Figure 5.18. Magnetization loops of the elliptical Co dot array at four different angles. The applied field direction is in-plane. The angle convention of the in-plane applied magnetic field is shown in Fig. 5.13(c).

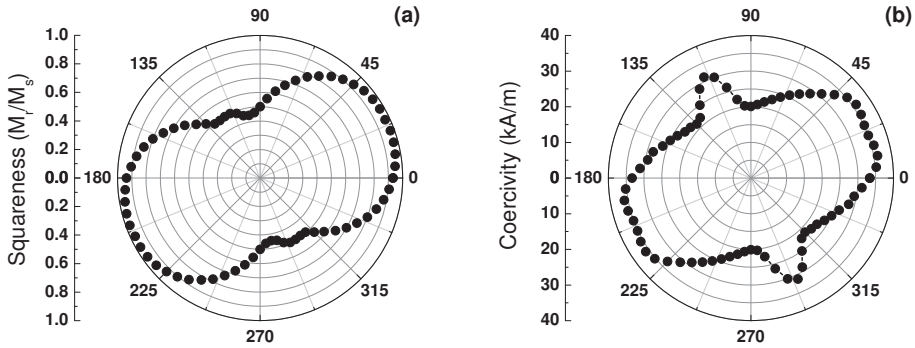


Figure 5.19. Polar plots of (a) the squareness of elliptical Co dots versus the field angle. (b) the coercivity of elliptical Co dots versus the field angle.

in unsaturated state.

We have fabricated elliptical magnetic Co dot arrays with 300 nm period as shown in Fig. 5.17. The long axis length of the Co dots is 340 nm, its short axis length is 160 nm, and its thickness is 15 nm. Figure 5.17(c) depicts the angle convention of the applied in-plane magnetic field in the measurement with respect to the array direction. We measured the magnetization loop of the elliptical magnetic dots with varying the in-plane magnetic field orientation. Figure 5.18 shows the magnetization loop of the elliptical magnetic dot array at four different angles including the magnetic easy axis and the magnetic hard axis in plane. The magnetic easy axis direction is 22.5° , and the magnetic hard axis is 112.5° . The size of this elliptical element is too large to behave like a single domain particle. Nevertheless, these curves are very similar to the magnetization loop of a single domain structure with a uniaxial anisotropy[93], of which easy axis coincides with geometrical long axis direction of the elliptical structure.

We have measured the hysteresis curves with varying the in-plane magnetic field angle, and obtained the polar plots of the squareness versus the field angle (Fig. 5.19(a)) and the coercivity versus the field angle (Fig. 5.19(b)). These measurements confirm the uniaxial shape anisotropy of the elliptical particle, except the increase of the coercivity at 112.5° and 292.5° . This direction coincides with the position of the nearest neighbors. As we have studied in the circular dot array, we believe that this configurational in-plane anisotropy is originated from the magnetic coupling among nearest neighbors

in unsaturated state. From the analysis of the elliptical magnetic element, we find that the elliptical shape with long-axis-to-short-axis ratio of 2:1 is enough to get a uniaxial in-plane anisotropy, but we have to take into consideration the magnetostatic interaction from the nearest neighbors in the densely packed arrays.

5.4 Conclusions

In summary, we have studied the magnetic properties of nano-scale magnet arrays to understand the scaling behaviour of their magnetic configurations and the magnetostatic interaction between them. We have fabricated nano-scale magnetic elements using laser interference lithography (LIL) and lift-off technique, and characterized the magnetic properties of the nano-scale magnetic elements using magnetometry and magnetic force microscopy. The magnetic configuration of the nano-scale elements is closely related with the size and shape of the elements. Circular dots with 500-nm diameter show a vortex structure with a clear vortex core observed by magnetic force microscopy. The behavior of the vortex structure in magnetic field has been studied by magnetometry, which is in good agreement with micromagnetic simulations. We also find that magnetic elements with 150 nm dimensions seem to have a simple magnetic structure except a configurational anisotropic magnetic coupling between the magnetic elements. This configurational anisotropic magnetic coupling plays an important role in the densely packed arrays.

We conclude that the magnetic structure with a vortex configuration is not suitable to obtain uniform magnetization in the magnetic element; an elliptical shape with large shape anisotropy is a proper geometry; the distance between the magnetic elements should be far enough to neglect the magnetostatic interaction among the adjacent magnetic materials. The knowledge obtained from these studies can be applied to obtain a uniform magnetization in magnetic elements, for example, the source and drain contacts of the spin-MOSFET as well as to control the switching of their magnetic moments.

Chapter 6

Prospects for Si-based spintronic devices

The realization of Si-based spintronic devices relies on the proper contacts between the ferromagnetic source/drain and the semiconductor. This chapter first describes that the spin-tunnel contacts with low-work-function ferromagnet (FM) interlayers satisfy three requirements for the source/drain contacts of the Si-based spin MOSFET, namely, suitable resistance-area (RA) product (chapter 2 and 4), high tunnel-spin polarization (chapter 3), and controlled magnetic switching (chapter 5). Using the results obtained in the previous chapters, we show that the spin-tunnel contacts can be integrated into a full device with a Si channel with two FM contacts for the magnetoresistance (MR) observation. We discuss the device-related issues—the design of the source/drain contacts and suitable geometries (lateral and vertical) for the MR observation—to realize the electrical spin injection and detection in Si. We also describe spurious signals owing to the effect of stray magnetic field on the current in the Si channel, and discuss their consequences for the MR observation.

6.1 Introduction and motivation

The main objective of the thesis is to investigate the issues for developing Si-based spintronic devices, such as the Si-based spin-MOSFET, and to provide

the solutions towards a realization of such devices. One of the main functions of the Si-based spin-MOSFET is that the channel conductance is modulated by the relative alignment of the source and drain magnetization. As a consequence, the demonstration of MR in a Si channel with two ferromagnetic contacts is essential to realize such device. In this section 6.1, we first briefly summarize the main results of the previous chapters. Based on this, we will, in section 6.2, discuss the prospects for Si-based spintronic devices.

In chapter 1, it has been shown that the requirements for the electrical spin injection in semiconductor are different from the requirements for the two-terminal MR observation in the spin-MOSFET structures. Three requirements for the proper source and drain contacts are introduced: namely, suitable resistance-area (RA) product, high tunnel spin polarization (TSP), the controlled magnetic switching, which have been accomplished through the researches in the following chapters.

In chapter 2, we have described how to develop FM/I/Si contacts that satisfy the requirements for the suitable source and drain electrodes of the Si spin-MOSFET structure. It has been explained that the Schottky barrier formation in FM/I/Si contacts gives rise to major obstacles for the MR observation in a Si spin-MOSFET structure. The RA product of the FM/I/Si contact—which comprises standard FM (Co or $\text{Ni}_{80}\text{Fe}_{20}$) and Al_2O_3 insulator—has been investigated to find out whether these contacts qualify as conductivity-matched source and drain electrodes. It turns out that the RA product of these contacts are many orders of magnitude higher than the optimum values for the observation of MR in a Si spin-MOSFET, because of the Schottky barrier formation. From these results, we conclude that the MR observation in a Si spin-MOSFET is not possible with standard FM contacts and the conventional method of adjusting the tunnel barrier thickness to control the tunnel conductance. A breakthrough to this problem has been presented, which uses a radically different approach for spin-tunnelling resistance control, introducing a low work-function ferromagnet inserted at the FM/tunnel barrier interface. It has been demonstrated that the insertion of a low work-function Gd interlayer in the FM/I/Si contacts provides remarkable tunability of the Schottky barrier height to Si and thereby the RA product of the contact over eight orders of magnitude. A very small Schottky barrier height with an ultrathin interlayer secures the optimum RA product for the observation of MR in a Si spin-MOSFET. We have also characterized the structural and chemical properties of FM/ Gd/ I/ Si contacts.

In chapter 3, it has been demonstrated that the spin tunnel contacts with a low work-function ferromagnet injects carriers with reasonably high TSP into the other electrode through a tunnel barrier. This was concluded from TMR measurements on a series of MTJs with this type of spin tunnel contacts as an electrode. It has been shown that MTJs with a low work-function ferromagnet provides a reasonably high value of TMR with clear magnetization switching. We have obtained the TSP of the spin tunnel contacts from the measured TMR values, and investigated the TSP as a function of thickness of the low work-function interlayer at different temperatures. We find that the TSP of tunnel contacts with a low work-function ferromagnet depends on many parameters: ferromagnet elements, alloy composition, the strength and the sign of magnetic coupling, voltage bias, and temperature. It has been demonstrated that the spin tunnel contacts with low work-function ferromagnet have a reasonably high TSP, satisfying the second requirements of the source and drain contacts to realize the Si-based spin MOSFET.

In chapter 4, we have presented another method to control the RA product of the FM/I/Si contact and to reduce the Schottky barrier height, namely, by engineering the Si surface with Cs. The properties of the Cs-coated Si surface has been investigated by determining the density of the gap states and the charge neutrality level of FM/I/Si contacts with the Cs-coated Si surface, which are compared to those with the normal Si surface. It has been shown that (i) the Cs-coating of Si results in a change of the charge neutrality level, which becomes located at about 0.1 eV below the conduction band minimum, and (ii) the density of the gap states has been increased owing to the presence of the Cs. As a result, the Schottky barrier height is greatly reduced for all FM materials of the contact, although some tunability using the contact metal work function is still preserved. It turns out that Cs-coated Si provides a very low Schottky barrier height even with very thin Gd layer. We have found indications of two-dimensional electron gas at the n -type Si surface, using the Cs-coated Si in FM/I/Si tunnel contacts.

In chapter 5, the magnetic properties of nano-scale magnetic elements have been studied. From the characterization of their magnetic properties, we have shown that the magnetic configuration of nano-scale magnetic elements is closely related with the size and shape of the elements as well as the magnetostatic interaction among the magnetic elements that are densely packed at a length scale of 100 nm. We have established criteria to obtain almost uniform magnetization in such nano-scale magnetic elements.

Now that the properties of the FM/I/Si contacts are known, using the results from chapter 1 to chapter 4, we are ready to discuss the prospects for the electrical spin injection and detection in Si. Section 6.2 is devoted to discuss the possibility of the MR observation in Si-based spin-MOSFET, when the spin-tunnel contacts, developed in the previous chapters, are integrated into a full device with a Si channel with two FM contacts. We shall discuss the device-related issues, the design of the source/drain contacts as well as suitable device configurations including lateral and vertical geometries for the MR observation. Section 6.3 discusses spurious signals due to the effect of stray magnetic field on the current in the Si channel.

6.2 Towards electrical spin injection and detection in Si

In order to demonstrate spin-polarized transport in a Si channel between a FM sources and drain, we need to observe magnetoresistance (MR) signal in those structures. We set aside a gate-voltage control of the conductance of the Si channel. We first focus on the design of the contact, and describe vertical and lateral device configurations.

6.2.1 Prospects for MR observation in Si spin-MOSFET

In this section, we combine the measured RA product of the $\text{Ni}_{80}\text{Fe}_{20}/\text{Gd}/\text{Al}_2\text{O}_3/\text{Si}$ contacts with a low work-function Gd interlayer in chapter 2 and their measured TSP in chapter 3 to show that this type of tunnel contact satisfies the requirements for the suitable source and drain contacts of a Si-based spin MOSFET. This discussion is based on the model with flat band approximation in diffusive regime[16, 27], which neglects the potential energy landscape as described in chapter 1. This choice will be justified by designing the contact so that it can provide almost zero Schottky barrier height. The results in Fig. 2.14 (chapter 2) and Fig. 3.4 (chapter 3) are combined to give the range over which the RA product of the tunnel contact with the Gd/ $\text{Ni}_{80}\text{Fe}_{20}$ bilayer can be tuned while simultaneously maintaining a reasonable TSP. For instance, if we choose a minimum TSP of 10 %, then the thickness of the Gd

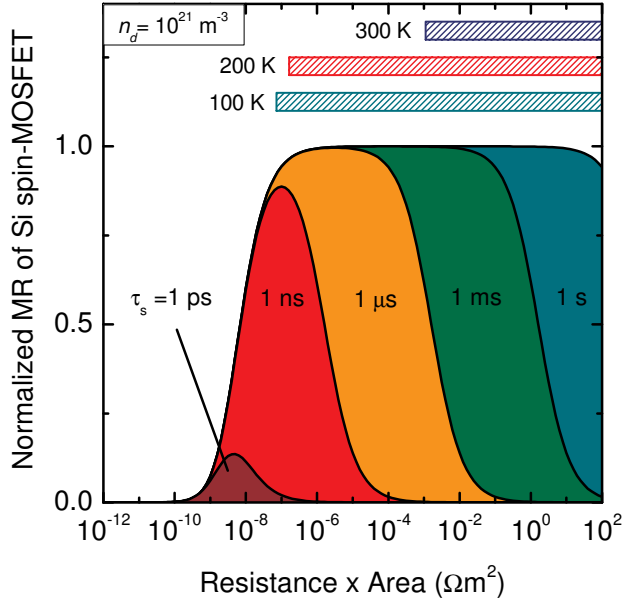


Figure 6.1. Optimum resistance-area product of tunnel contacts for a Si spin-MOSFET. Colour lines depict the calculated MR of FM/I/Si/I/FM spin-MOSFET structures as a function of the RA product of FM/I/Si tunnel contacts for given spin lifetimes in the Si (τ_s). Hatched areas at the top of the graph show the ranges of RA product of $\text{Ni}_{80}\text{Fe}_{20}/\text{Gd}/\text{Al}_2\text{O}_3$ tunnel contacts over which the TSP is larger than 10% at 100 K, 200 K, and 300 K, respectively.

interlayer can be varied from 0 up to 2.0 nm at 100 K, to 0.8 nm at 200 K, and to 0.4 nm at 300 K. This means that the RA product can be tuned down to 10^{-7} , to 10^{-7} , and to $10^{-3} \Omega\text{m}^2$ at 100, 200, and 300 K, respectively. In Fig. 6.1, the range of RA product of tunnel contacts over which the TSP is larger than 10% is compared to the RA product required to obtain MR in a spin-MOSFET for different values of the spin lifetime τ_s in the Si.

The optimum RA product for conductivity matching to Si depends on τ_s , which is a function of temperature and the dopant density of Si. While a τ_s of 7 ns in Si has been measured by electron spin resonance [3], it is unclear whether this is straightforwardly relevant for electrical transport in Si. Considering the fact that the τ_s in *n*-type GaAs ($n_d = 10^{22} \text{ m}^{-3}$) exceeds 100 ns at 5 K and 1 ns at 100 K [35], a longer spin lifetime may be expected for *n*-type Si. Nevertheless, given the uncertainty in τ_s , the MR of the FM/I/Si/I/FM structure versus the RA product of the FM/I/Si contact has been cal-

culated for different τ_s values for a Si dopant density of 10^{21} m^{-3} (Fig. 6.1), and compared to the RA ranges of the FM/I/Si contacts obtained with low work function FM Gd. Figure 6.1 clearly shows that the observation of MR in a Si spin-MOSFET is not possible with conventional FM contacts ($RA = 10^2 \Omega\text{m}^2$ at room temperature) unless the τ_s in Si is more than a second. By contrast, the spin-tunnel contacts with low work-function FM allows one to tune the RA product to the range in which a MR should be observable even for sub-nanosecond τ_s in Si. Hence, spin-tunnel contacts with low work-function ferromagnets raise prospects for spin injection into Si and for the realization of the Si spin-MOSFET. It should be noted that a τ_s of $\sim 1 \text{ ms}$ is required to obtain room-temperature operation. However, the situation is improved when the Cs-coated tunnel contact, Si/ Cs/ Al_2O_3 / Gd/ $\text{Ni}_{80}\text{Fe}_{20}$, is used. Because thinner Gd layer ($\sim 0.5 \text{ nm}$) is enough to obtain a lower RA product with a high TSP at 300 K, the ranges of RA product of tunnel contacts—over which the TSP is larger than 10% at 300 K—can be expanded to $10^{-8} \Omega\text{m}^2$. As a consequence, a τ_s of $\sim 1 \text{ ns}$ is enough to secure the room-temperature operation of the spin-MOSFET.

6.2.2 Design of the source and drain contacts

We have described, in chapter 2 and 4, the layer stack of the source and drain contacts based on Si/ Al_2O_3 / Gd/ $\text{Ni}_{80}\text{Fe}_{20}$ or Si/ Cs/ Al_2O_3 / Gd/ $\text{Ni}_{80}\text{Fe}_{20}$. For the fabrication of a Si channel with the source and drain contacts (FM/ I/ Si/ I/ FM structure), we need to consider the specifications of the contacts, such as the thickness of a low work-function interlayer as well as the length, the resistivity, and the dopant density of the Si channel to obtain the desired characteristics.

The channel conductance of Si and the spin lifetime of electrons in Si determine the suitable resistance-area (RA) product of the source and drain contacts. We have selected a low-doped n -type Si channel with the dopant density of 10^{21} m^{-3} ($\rho_N = 4.5 \times 10^{-2} \Omega\text{m}$), considering that the spin lifetime of electrons in a semiconductor is reduced at higher dopant density[35]. If the spin relaxation time (τ_s) of 7 ns and the Si channel length (t_N) of 100 nm are used as discussed from the previous section, the optimum range for RA product of the source and drain contact would then be in between $4.5 \times 10^{-8} \Omega\text{m}^2$ and $5.7 \times 10^{-6} \Omega\text{m}^2$ at room temperature given by Eq. 1.2. We expect a longer

spin lifetime of electrons at lower temperature. The lower limit ($\rho_N t_N$) of the window for the optimum MR depends on temperature via the resistivity of Si. The resistivity of Si with the dopant concentration of 10^{21} m^{-3} doesn't change drastically from room temperature to 100 K, but it changes drastically below 100 K as will be shown in section 5.3. Both the lower limit ($\rho_N t_N$) and the upper limit ($\rho_N (l_{sf}^N)^2 / t_N$) move up with decreasing temperature due to the increase of ρ_N , but the increase of the upper limit is enhanced by the increase of τ_s (and thus l_{sf}^N) at low temperature; hence, the optimum window for the MR observation becomes wider at low temperature.

Apart from the effect on the RA product of the contacts, a high Schottky barrier height of 0.5 eV also influences adversely the transformation of the spin accumulation (typically, $1 \mu\text{V} \sim 1 \text{ meV}$) at the Fermi energy level of Si to an electrical signal in two terminal measurement. It is also known that the electric field protracts the spin diffusion length along the field direction, but it retracts the spin diffusion length against the field direction [37]. In order to avoid these effects, a flat band condition is desirable. Using the results in chapter 2 and 4, we select the thickness of Gd layer of the contacts which gives rise to a negligible Schottky barrier height, for example, 0.8 nm for normal Si and 0.5 nm for Cs-coated Si. This Gd thickness also provides the optimum value of the RA product of the source and drain contacts.

The maximum tunnel spin polarization (P) at room temperature is $\sim 5\%$ for 0.8 nm Gd interlayer, and $\sim 8\%$ with 0.5 nm Gd interlayer. If we sacrifice the room temperature operation of the device, this can be improved to $\sim 20\%$ with 0.8 nm Gd interlayer and $\sim 25\%$ with 0.5 nm Gd interlayer at 100 K. The maximum MR of a symmetric FM/I/Si/I/FM structure is given by $P^2 / (1 - P^2)$. Thus the expected MR is about $0.3 \sim 0.6\%$ at room temperature and about $4 \sim 7\%$ at 100 K. Obviously this can be improved by further engineering of the TSP of such contacts.

It is desirable to use a source or drain contact that can guarantee almost uniform magnetization (width $< 150 \text{ nm}$). If we used a source or drain contact larger than this size, the TSP of injected electrons would be an averaged value over the area. Consequently, it is recommended to avoid a contact geometry that may result in vortex configuration. It is important to select a proper geometry of the device to observe the MR. We shall describe two possible approaches—a vertical geometry and a lateral geometry—in the following sections, and discuss their advantages and disadvantages.

6.2.3 Vertical geometry

The discussion of the MR of the FM/I/Si/I/FM structure has so far been based on the one-dimensional model of the diffusive electron transport with a flat band assumption as described in chapter 1. A vertical geometry seems to be a natural choice, since it is very close to this one-dimensional model system.

The epitaxial growth of a Si layer on a metallic electrode is not a realistic way to fabricate a vertical geometry because of its practical difficulties. Instead, there are two possible methods to realize a vertical geometry of FM/I/Si/I/FM structure we have considered: one is to use a metal bonding technique as used in the fabrication of the spin-valve transistors, and the other is to use a Si membrane structure. We have selected a Si membrane-based structure.

Figure 6.2 depicts a schematic diagram of the membrane structure that we have designed and fabricated. We have used a backside etching of a silicon-on-insulator (SOI) wafer to form a Si membrane. The backside etching stops at the buried oxide layer, and the device layer thickness of the SOI wafer determines the Si channel length. The details of the membrane fabrication process are described in the appendix. Figure 6.3 shows an SEM image of the fabricated membrane structure. The contact area on both the front side and backside of the membrane is protected by a 40 nm dry-oxide layer before the thin film deposition. After removing these sacrificial oxide layers on the membrane, proper multilayer stacks are deposited consecutively both on the front side and on the backside of the membrane for the spin tunnel contact formation. This deposition process is basically the same as the process for the MIS contact fabrication in chapter 2.

The use of a Si membrane has many advantages. First, it is possible to control the Si channel length accurately down to 200 nm by fabricating a thin Si membrane. Second, one can deposit different film stacks for the source and drain electrode, which is very useful to control the RA product and the magnetization of each electrode independently. Third, there is no limit in the lateral size of the source and drain contact, which guarantees a large current signal with an averaged spin-polarization of electrons from a continuous film. The Si membrane approach also has possible disadvantages. For example, a mechanical defect like warpage of the membrane might deteriorate the quality of the tunnel barrier. There is a possibility that the resistance of the Si channel can be affected by the ordinary (Lorentz) magneto-resistance of the

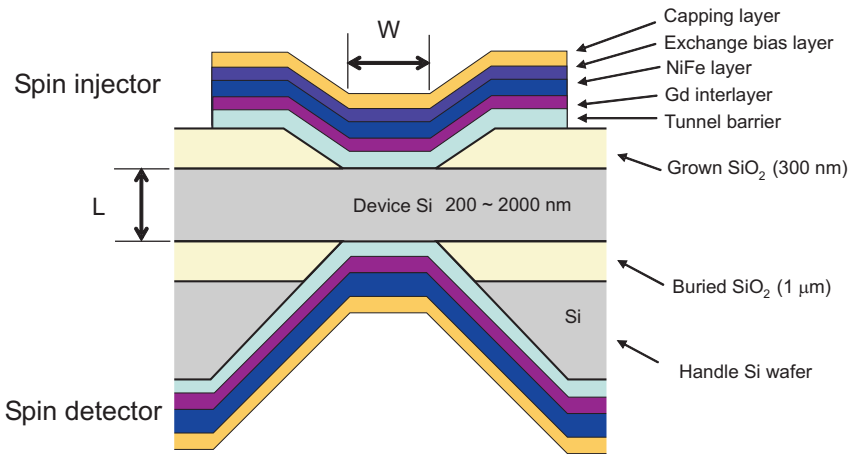


Figure 6.2. A schematic diagram of a vertical geometry for two-terminal MR observation. The Si channel length (L) is determined by the thickness of the device Si layer. The contact area defined by the grown oxide determines the width (W) of the Si channel.

Si channel itself as discussed in the next section.

We need a careful attention to design the fabrication process of the membrane to avoid any possible imperfection. For example, Fig. 6.3 (b) and (c) show the difference between two membrane structures at the edges of the backside. The edge undercut in the buried oxide (BOX) in Fig. 6.3(b) may give rises to a shadow effect during the metal contact layer deposition by e-beam evaporation process, which leaves undeposited area on the backside Si contact. In order to avoid the adverse effect from the edge undercut, we have conducted an additional Si etching step in between two buried oxide removal steps, which results in a well-defined edge between the Si surface and the BOX layer shown on the Fig. 6.3(c). In this case, the small undercut is located in between the half etched BOX layer and the completely etched BOX layer, which can be easily covered afterwards by a deposition method with better coverage like a sputtering process.

In an ideal case, the size and shape of the front side contact is exactly the same as the backside contact, and the alignment of the front side contact to backside is perfect. As this may not always be the case, we used a semiconductor device simulator (ATLAS, Silvaco international) to conduct a simple simulation of the electric field profile inside the Si membrane. In this simulation, the front side circular contact has a diameter of $4\ \mu\text{m}$ and the backside

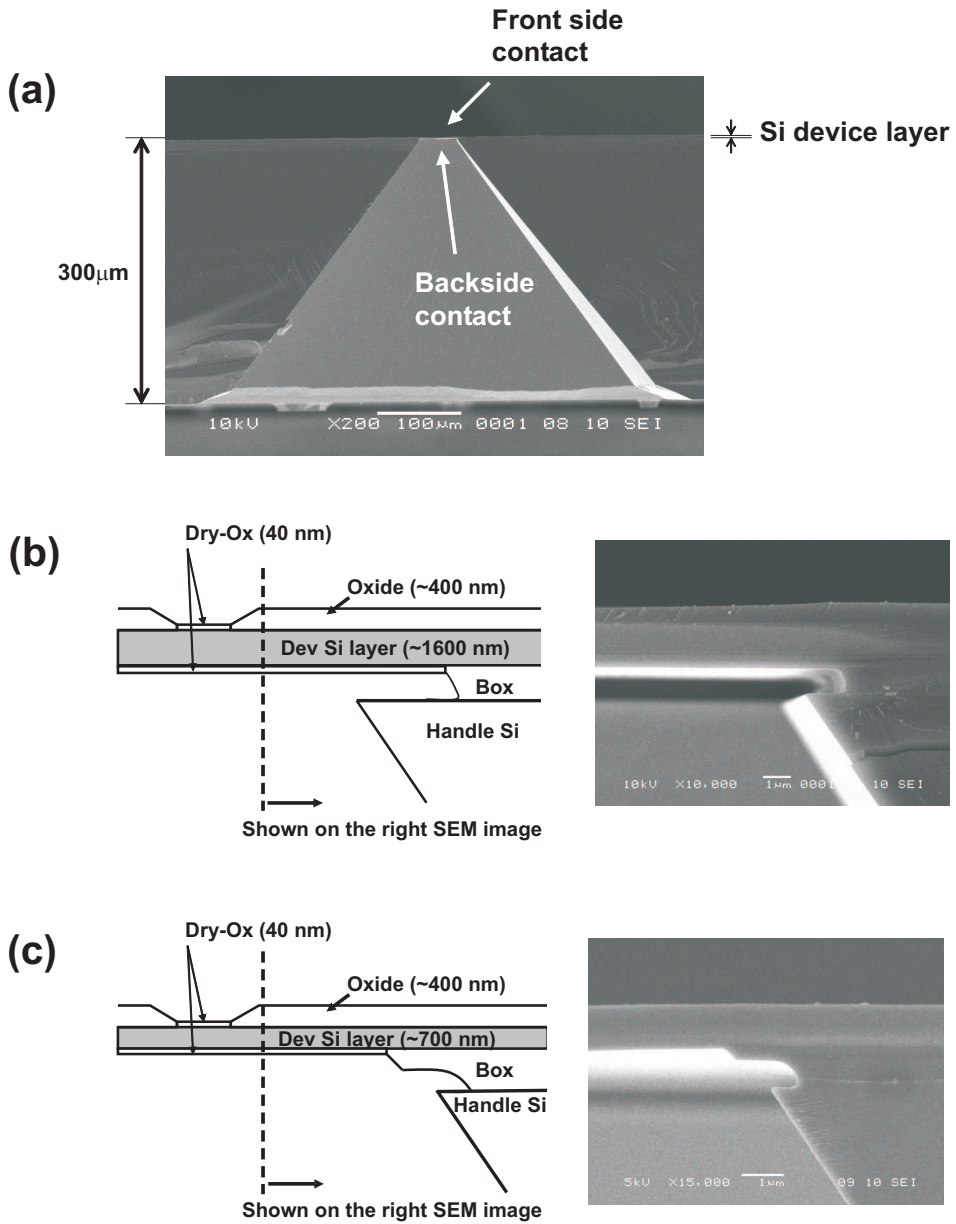


Figure 6.3. SEM images of the (a) membrane structure. Schematics and SEM images of (b) membrane with undercut (c) membrane without undercut.

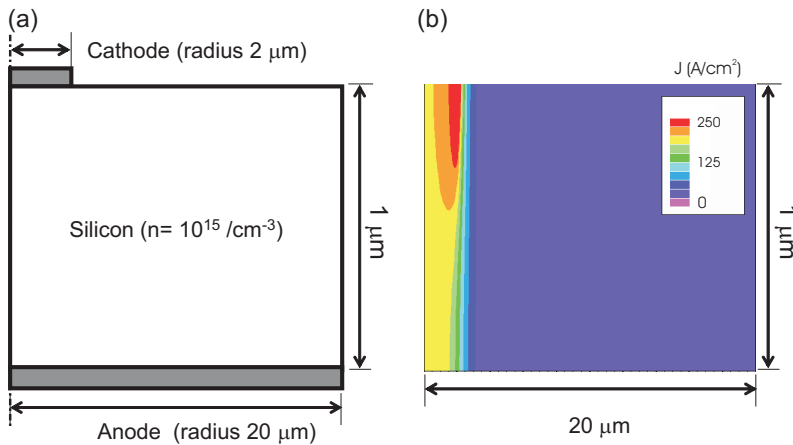


Figure 6.4. (a) Schematic device geometry used in the simulation. Please note that the cross section of the half of the device is shown in cylindrical coordinate system, and the lateral length scale is not the same as the vertical length scale. This thickness of the Si channel is $1 \mu\text{m}$. (b) Simulated current density profile inside the Si. Color code indicates the level of current density in Si.

circular contact has a diameter of $40 \mu\text{m}$. The cross section of the half of the device is shown in cylindrical coordinate system (Fig. 6.4(a)). If the current spreading is large, the actual distance between the source and the drain is not determined by the device Si thickness, but by the geometrical distance including the lateral size contribution. This might draw a crucial consequence in the spin transport, because all spin information of electrons may attenuate completely during the travel over a long current path. Figure 6.4(b) shows a simulated current density profile inside a $1\text{-}\mu\text{m}$ -thick Si channel ($n = 10^{15} \text{ cm}^{-3}$). The Schottky barrier height was set to zero in this calculation, assuming a flat band condition. It is shown that the current spreading is not significant when the contact resistance is negligible.

6.2.4 Lateral geometry

Figure 6.5 shows a lateral geometry which can be used for non-local measurement of a spin accumulation in the Si channel. The spin-polarized electrons are injected from one of the current probes (I^-), and the electrons flow from the injector to the other current probe (I^+). Two separate voltage probes are

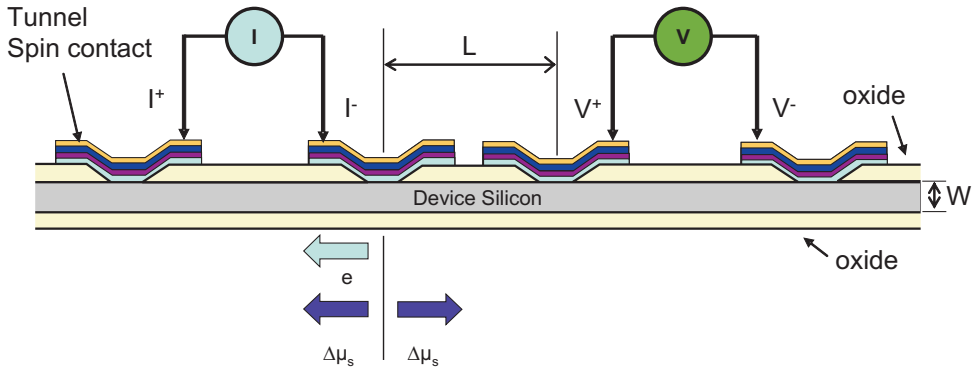


Figure 6.5. A schematic diagram of a lateral geometry for non-local MR observation. The Si channel length (L) is determined by the distance between the I^- and V^+ contacts. The width (W) of the Si channel is determined by the thickness of the device Si layer. Spin polarized electrons flow from the I^- contact to the I^+ contact, producing a spin accumulation ($\Delta\mu_s$). This $\Delta\mu_s$ is detected by two separate voltage probes, V^+ and V^- contacts.

used to measure the chemical potential difference due to the spin accumulation ($\Delta\mu_s$) in the Si channel produced by the injected spin-polarized electrons.

The current flowing in the Si channel generates spurious effects such as local Hall effect and MR, but confined to the MR of two current probes (I^+ , I^-). The advantage of the non-local voltage probes is that one can determine the spin accumulation while minimizing spurious effects. Because the current between two voltage probes (V^+ , V^-) is negligible in comparison with the current between two current probes (I^+ , I^-), the current and the voltage circuits are relatively well separated in this geometry[123]. This technique has proven its usefulness in many experiments [36, 123].

The spacing between two probes should be within the spin diffusion length in Si to expect a large electrical signal. As the spin diffusion length seems to be on the order of a few microns at room temperature, we need a nano-scale fabrication technique like e-beam lithography to attain high spatial resolution. Because of this small dimension of the source and drain contact, the control of the magnetic configuration is also very important for the lateral geometry. A difference in the dimensions of the injector and detector strip provides the difference in the coercivity of those contacts and thereby the switching from the one magnetic configuration (anti-parallel or parallel) to another. The optimum window of the RA product of the contact for the lateral geometry is

slightly different from that of the vertical geometry as discussed in Ref. [27]. A pattern transfer process like ion beam etching usually results in an edge damage of the pattern. Consequently, it is useful to have a contact hole to the Si defined by a passivation insulator as shown in Fig. 6.5. If the metallic source and drain pattern is larger than the contact hole, the edge damage of the patterns during the etching process doesn't influence the quality of the real contact during the process.

The vertical geometry in the previous section has advantages in that the standard photolithography allows us a short channel length with controlled magnetic configurations of the spin injector and detector; this approach is useful to prove the two-terminal MR of the device, but it is difficult to integrate a gate control. The lateral geometry may require a lithography technology to fabricate a channel length less than $1\ \mu\text{m}$, but this geometry is similar to the real spin-MOSFET structure. As a consequence, the lateral geometry would be the ultimate choice for the real spin-MOSFET fabrication. Another advantage of the lateral geometry is that the four-terminal non-local measurement technique can be used to prove the spin accumulation in semiconductor and to study the fundamental physics. However, the actual spin-MOSFET is based on the current between the source and drain; it will operate in two-terminal geometry. The demonstration of a MR in the two-terminal measurement is required to prove the operation of spin-MOSFET. This is also relevant for the vertical devices. Therefore, it is important to quantify the spurious effects, like local Hall effect and the MR owing to the current in the Si channel, which is the topic of the next section.

6.3 Stray field in the Si channel

When a finite ferromagnet pattern is magnetized, a strong magnetic fringe field—an order of 1 T—develops near the edges of the ferromagnet pattern[124, 125]. If this field is perpendicular to the current path, the deflection of the current causes a hall voltage in the transverse direction of the current. This effect is especially significant in a low-doped Si channel with high mobility. Sometimes, a spurious signal from this local Hall effect can mimic the true magnetoresistive response of the device[124, 125]

Besides the local Hall effects, there exists the ordinary (or Lorentz) MR of a Si channel. Every material has the ordinary MR originated from the in-

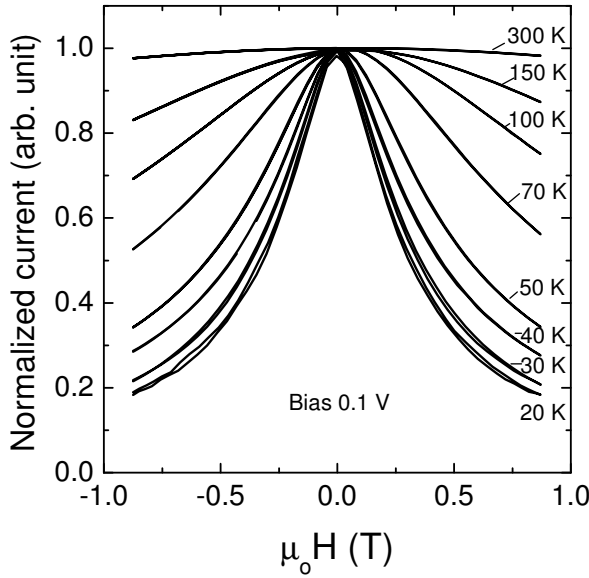


Figure 6.6. MR of a Si channel (resistivity, $\rho = 5 \sim 10 \Omega\text{cm}$; P dopant density, $n_d = 10^{15} \text{ cm}^{-3}$) versus magnetic field measured at various temperatures.

fluence of the Lorentz force on the motion of electrons. The resistivity of a semiconductor is a function of magnetic field as a transverse magnetic field, and the MR is determined by [126]

$$\frac{\rho(B)}{\rho(0)} = T_M \mu^2 B^2, \quad (6.1)$$

where ρ is the resistivity of semiconductor, T_M is the magnetoresistance scattering coefficient, and μ is the mobility of electrons. It is known that the MR depends more strongly on the scattering mechanism than does the Hall coefficient; the T_M varies between 0.38 (for acoustic deformation potential scattering) and 2.15 (for ionized impurity scattering)[126]. The shape of the MR curve is well described by

$$I = \frac{V}{R_{Si}(1 + T_M \mu^2 B^2)}, \quad (6.2)$$

where R_{Si} the resistance of the Si channel at zero magnetic field.

In order to investigate the MR of a Si channel, we have fabricated a Si channel (the resistivity, $\rho = 5 \sim 10 \Omega\text{cm}$; the dopant (P) density, $n_d = 10^{15}$

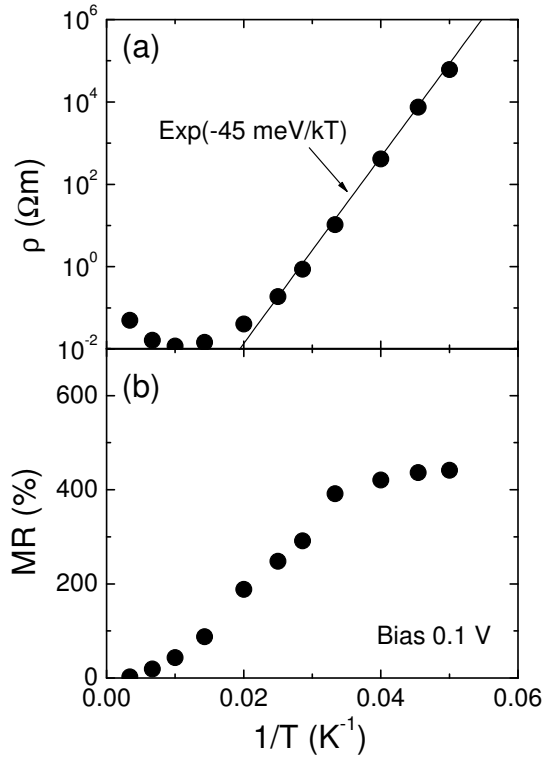


Figure 6.7. (a) Resistivity and (b) MR of a Si channel (resistivity, $\rho = 5 \sim 10 \text{ } \Omega\text{cm}$; dopant (P) density, $n_d = 10^{15} \text{ cm}^{-3}$) versus temperature. The fit for R in (a) is for the activation energy calculation.

cm^{-3}) with four ohmic contacts with low contact resistance. Figure 6.6 shows the MR of the Si channel at different temperatures. Very surprisingly, the magnitude of MR is as large as 400% at low temperature! The shape of the MR curves is Lorentzian as described by Eq. 6.2. The magnitude of MR and the width of the curves depend on temperature, because of the temperature dependence of the resistivity and mobility.

Figure 6.7(a) shows the resistivity of the Si channel as a function of temperature. As the temperature decreases, the resistivity decreases slowly down to 100 K owing to the increased mobility, but it increases exponentially below 50 K as the freezing of carriers limits the conductivity. The linear fit at low temperature represents the activation energy of 45 meV, which is in good agreement with the ionization energy of phosphorous donors in the literature [127]. Figure 6.7(b) shows the MR of the Si channel as a function of temper-

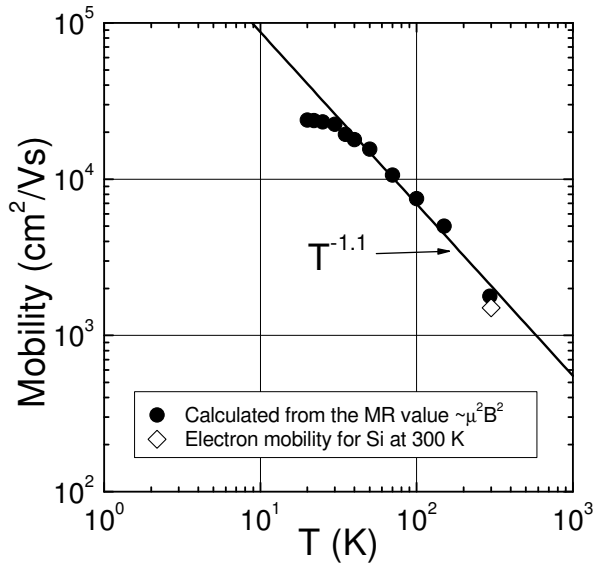


Figure 6.8. Mobility of electrons in Si calculated from the MR experiments (Fig. 6.7 using Eq. 6.1). The fit shows the temperature dependence of the electron mobility in Si. The electron mobility in Si at room temperature from literature[45] is shown for comparison.

ature. This MR value is measured 0.1 V bias and calculated as $(\rho(0.8 \text{ T}) - \rho(0 \text{ T})) / \rho(0 \text{ T})$. The MR increases rapidly with decreasing temperature down to 50 K, and it saturates at low temperature. It is striking that the values of the MR is as high as 400% at low temperature.

Assuming the MR of channel follows Eq. 6.1 and Eq. 6.2, we can calculate the mobility of the Si from the measured value of the MR (Fig. 6.7) or the shape of the MR curves (Fig. 6.6). Figure 6.8 shows the calculated mobility of electrons in Si from the MR values using Eq. 6.1 with $T_M=1$. We find that the mobility is proportional to $T^{-1.1}$, which is in good agreement with the general temperature dependence of the mobility in Ref. [45]. This confirms that this MR originates from the effect of the Lorentz force on the electron motion in a magnetic field. Moreover, we find that the large μ at low temperature, and the μ^2 dependence of MR (Eq. 6.1) gives rise to large MR effects.

Because the conductivity matching necessarily requires that the channel resistance should be more or less similar to the contact resistance, the ordinary MR is unavoidable in the Si channel, and the only way to solve it is to minimize fringe fields. We expect an MR less than 10% from the electrical

spin injection and detection. If the fringe field from the ferromagnetic pattern is large, for example, ~ 1 T, this field changes the resistance of the Si channel near the ferromagnet up to 400% depending on the temperature, which may be misunderstood as a signal from the spin accumulation. In order to distinguish between these two contributions, we need to design a careful control experiment.

6.4 Conclusions

The development of the Si-based spintronic devices requires proper design of the contacts between the ferromagnetic source/drain and the semiconductor. The spin-tunnel contacts with a low-work-function interlayer satisfy the requirement for the suitable contact for the source and drain contact of Si-base spin MOSFET. We have shown that the spin-tunnel contact with a low-work-function interlayer allows tuning of the RA product over many orders of magnitude—while a reasonable tunnel spin polarization is maintained—in which a MR in a full device with a Si channel and two FM contacts should be observable even for sub-nanosecond τ_s in Si. By contrast, the observation of MR in a Si spin-MOSFET is not possible with conventional FM contacts unless the τ_s in Si is more than a second in diffusive regime. Hence, spin tunnel contacts with low work function ferromagnets raise prospects for spin injection into Si and for the realization of the Si spin-MOSFET. As a consequence, the spin-tunnel contacts can be integrated into a full device for the MR observation. The expected MR is about 0.3~0.6% at room temperature and about 4~7% at 100 K. Obviously this can be improved by further engineering of the TSP of such contacts.

We have described two suitable configurations for the MR observation, a vertical geometry with a Si membrane, and a lateral geometry with non-local spin accumulation measurement, and discussed the advantages and disadvantages of both approaches. We find that the large mobility of electrons in the Si channel at low temperature and the quadratic mobility dependence of MR give rise to surprisingly huge MR effects, as large as 400% at low temperature. Because the spin-MOSFET is based on the two-terminal MR response between the source and drain—if we set aside a gate-voltage control of the conductance of the Si channel—it is important to minimize stray field effects

in the Si channels, especially the MR originated from the Lorentz force on the electron current in a magnetic field.

Conclusions

Recent progress in semiconductor-based spintronics opens up a possibility to develop novel devices that can be applied for the solid-state information devices. One of the main goals of the semiconductor-based spintronics is to realize a three terminal device, a spin transistor, which has memory and amplification functionalities in one device. The aim of the thesis is to investigate the issues for the development of semiconductor-spintronic devices, such as the spin-MOSFET, and to provide the solutions towards a realization of such devices. The spin-MOSFET structure consists of a semiconductor channel and two ferromagnetic contacts for the source and drain electrodes. In order to realize the device, three requirements should be satisfied: (i) injection of spin-polarized current of electrons from FM into semiconductor, (ii) transport of electrons through the semiconductor without losing the spin information, (iii) detection of spin-dependent transmission into the FM drain contact. We have selected Si as a semiconductor because the mainstream semiconductor industry is based on Si technology, and Si is expected to have a longer spin life time with less spin-relaxation mechanisms than III-V compound semiconductors due to smaller spin-orbit coupling and a lattice with inversion symmetry. However, there has been no evidence of the spin accumulation in Si, the technologically most important semiconductor. The injection and the detection of spin-polarized electrons in Si has been fettered, since it is difficult to use optical detection techniques as one can do with III-V semiconductors. The MR in a Si channel with two ferromagnetic contacts should be demonstrated to realize the Si spin-MOSFET, which requires careful design of the contacts between the ferromagnetic source/drain and the semiconductor. Inserting a

tunnel barrier has been key to achieve spin-injection from ferromagnetic (FM) metals into GaAs to avoid the conductivity mismatch problems. However, as introduced in chapter 1, it has been shown that the requirements for the electrical spin injection in semiconductor are different from the requirements for the two-terminal MR observation in the spin-MOSFET structures. This results in three requirements for the proper source and drain contacts: namely, suitable resistance-area (RA) product, high tunnel spin polarization (TSP), the controlled magnetic switching.

In chapter 2, the properties of FM/I/Si contacts has been studied for the application of the source and drain electrodes of the Si spin-MOSFET structure. A series of high-quality FM/I/Si contacts has been fabricated with standard ferromagnetic materials, such as Co and $\text{Ni}_{80}\text{Fe}_{20}$ alloy. It turns out that the RA product of these contacts are many orders of magnitude higher than the optimum values for the MR observation in a Si spin-MOSFET structure, because the Schottky barrier formation in the FM/I/Si contacts gives rise to the major obstacle to the MR observation: namely, (i) low current due to a (reverse biased) Schottky barrier, (ii) electrons tunnel into or out of states at elevated energy, for which the TSP is strongly reduced, and (iii) a huge conductivity mismatch of many orders of magnitude between Si and tunnel contacts with ferromagnetic metals such as Co and NiFe alloys. From these results, we conclude that the observation of MR in a Si spin-MOSFET is not possible with standard FM contacts and the conventional method of adjusting the tunnel barrier thickness to control the tunnel conductance.

In chapter 2, we have presented a breakthrough to this problem by introducing a low work-function ferromagnet inserted at the FM/tunnel barrier interface. It has been shown that the Schottky barrier is completely removed by using a thick Gd electrode, the resistance-area (RA) product of FM/ Al_2O_3 /Si contacts is reduced by eight orders of magnitude, and the optimum RA product for the MR observation in spin-MOSFET structure is obtained. Besides a low RA product, the ability to *tune* the RA product is essential, since the RA product of the tunnel contact should be in an optimum range that also depends on the spin life-time in Si, which is not accurately known. The tuning of Schottky barrier height has been demonstrated using a sub-nm low-work-function Gd interlayer, based on the idea that the work-function of the electrode is determined by the outermost layers. We find that the Gd thickness needed to completely remove the Schottky barrier is only 0.8 nm. In this way the resistance-area (RA) product of FM/ Al_2O_3 /Si contacts can be tuned over

eight orders of magnitude, and the optimum RA product for the MR observation in spin-MOSFET structure can be achieved.

It has been shown in chapter 2 that the work-function engineering of the spin tunnel contact is a very useful tool to reduce the Schottky barrier of Si/Al₂O₃/Gd/Ni₈₀Fe₂₀ contacts. We find that the effective work-function of Gd/Ni₈₀Fe₂₀ bi-layer of the contact is linearly proportional to the Gd interlayer thickness up to 0.8 nm. By varying the effective work-function of the metal, we have obtained the surface density of gap states (D_s) and the charge neutrality level (ϕ_{CNL}) at the Si/Al₂O₃/ interface of the contact. Structural analysis of Si/Al₂O₃/Gd/Ni₈₀Fe₂₀ contacts shows that the deposited Gd layer is amorphous with relatively uniform thickness. The chemical and electrical analysis indicates that the oxidation of the deposited Gd layer is negligible in the contact. This confirms that the work-function engineering by a sub-nm Gd interlayer has been done by the metallic Gd. Therefore, the FM/I/Si contacts with a low work-function ferromagnet interlayer satisfies the first requirement for the source and drain electrodes of the Si spin-MOSFET, the RA matching to a Si channel.

It has been demonstrated in chapter 3 that the spin tunnel contacts with a low work function ferromagnet—inserted between the ferromagnet and the insulator of FM/Al₂O₃/Si tunnel contacts—injects spin-polarized carriers with a reasonably high TSP into the other electrode through a tunnel barrier, satisfying the second requirements of the source and drain contacts to realize the Si-based spin MOSFET. A series of MTJs of NiFe/Gd/Al₂O₃/Co and Co/Gd/Al₂O₃/Co have shown a reasonably high value of TMR with clear magnetization switching. We have obtained the TSP of the NiFe/Gd/Al₂O₃ and Co/Gd/Al₂O₃ electrode from the measured TMR values, and investigated the TSP as a function of thickness of the low-work function interlayer at different temperatures. The TSP of tunnel contacts with a low work function ferromagnet depends on many parameters, ferromagnetic elements, alloy composition, the strength and the sign of magnetic coupling, voltage bias, and temperature. There are still lots of room for improvement of the TSP at high temperature and the bias dependence. Further study is required to understand the complex behavior of MTJs with RE-TM materials which might be originated from the magnetic interactions between localized magnetic ions and conduction electrons.

In chapter 4, we have presented another effective way to control the RA product of the FM/Al₂O₃/Si contacts using an alkali-metal (Cs)-covered Si

surface. The spin tunnel contacts to Si with an alkali-metal-coated *n*-type Si surface show noticeably low Schottky barrier height. The Cs deposition on Si induces three times larger density of gap states, with a charge neutrality level very close to the conduction band edge of Si. Because of these gap states, the Fermi energy level in Si is close to an alkali-metal-induced surface state level, providing a low Schottky barrier height. By combining this new method with the low work function approach one can control the RA product of spin tunnel contacts to Si over a wide range as well as potential energy profile of spin tunnel contacts to Si. The Cs deposition on the Si surface represents an alternative method to engineer spin-tunnel contacts to obtain the desired RA product of spin tunnel contacts with a smaller Gd thickness in comparison with the normal Si surface, such that the TSP is expected to be higher. Surprisingly, an inverted diode characteristic has been observed in FM/ Gd/ Al₂O₃/ Cs/ Si contacts. This indicates an inverted band bending near the contact and the presence of an accumulation layer at the *n*-type Si surface. This suggests the formation of two-dimensional electron gas at the *n*-type Si surface, which is useful to design new devices using the properties of the two-dimensional electron gas.

In chapter 5, the magnetic properties of nano-scale magnet arrays have been studied to understand the scaling behaviour of their magnetic configurations and the magnetostatic interaction between them. We have fabricated nano-scale magnetic elements using laser interference lithography (LIL) and lift-off technique, and characterized the magnetic properties of the nano-scale magnetic elements using magnetometry and magnetic force microscopy. The magnetic configuration of the nano-scale elements is closely related with the size and shape of the elements. Circular dots with 500-nm diameter show a vortex structure with a clear vortex core observed by magnetic force microscopy. The behavior of the vortex structure in magnetic field has been studied by magnetometry, which is in good agreement with micromagnetic simulations. We also find that magnetic elements with 150 nm dimensions seem to have a simple magnetic structure except a configurational anisotropic magnetic coupling between the magnetic elements. This configurational anisotropic magnetic coupling plays an important role in the densely packed arrays. We find that the magnetic structure with a vortex configuration is not suitable to obtain uniform magnetization in the magnetic element; an elliptical shape with a shape anisotropy is a proper geometry; the distance between the magnetic elements should be far enough to neglect the magnetostatic interaction

among the adjacent magnetic materials. The knowledge obtained from these studies can be applied to obtain a uniform magnetization in magnetic elements, for example, the source and drain contacts of the spin-MOSFET as well as to control the switching of their magnetic moments.

It has been shown in chapter 6 that the development of the Si-based spintronic devices requires proper design of the contacts between the ferromagnetic source/drain and the semiconductor. We find the spin-tunnel contacts with a low-work-function interlayer satisfy three requirements for the suitable contact for the source and drain contact of Si-base spin MOSFET. We have shown that the spin-tunnel contact with a low-work-function interlayer allows tuning of the RA product over many orders of magnitude—while a reasonable tunnel spin polarization is maintained—in which a MR in a full device with a Si channel and two FM contacts should be observable even for sub-nanosecond spin life time in Si. By contrast, the observation of MR in a Si spin-MOSFET is not possible with conventional FM contacts unless the τ_s in Si is more than a second in diffusive regime. Hence, spin tunnel contacts with low work-function ferromagnets raise prospects for spin injection into Si and for the realization of the Si spin-MOSFET. As a consequence, this type of spin-tunnel contacts can be integrated into a full device for the MR observation. The expected MR is about 0.3~0.6% at room temperature and about 4~7% at 100 K. Obviously this can be improved by further engineering of the TSP of such contacts. We have described two suitable configurations for the MR observation, a vertical geometry with a Si membrane, and a lateral geometry with non-local spin accumulation measurement, and discussed the advantages and disadvantages of both approaches. We find that the large mobility of electrons in the Si channel at low temperature and the quadratic mobility dependence of MR give rise to surprisingly huge MR effects, as large as 400% at low temperature. Because the spin-MOSFET is based on the two-terminal MR response between the source and drain—if we set aside a gate-voltage control of the conductance of the Si channel—it is important to minimize stray field effects in the Si channels, especially the MR originated from the Lorentz force on the electron current in a magnetic field.

It is yet to be demonstrated whether the Si channel between the sources and drains shows a MR signal from the electrical spin injection and detection in the diffusive transport regime. It seems that there is no fundamental barrier for the electrical spin injection and detection in Si, but there are still a few technical issues to be improved. Improvement in TSP will certainly raise the

MR signal level, and the improvement in the device geometry will present advantages to avoid spurious effects from the stray field and the current in the Si channel. It is meaningful to study alternative methods to observe the spin accumulation in Si. For example, a magnetization switching of nano-magnets by the spin-polarized current would be useful to prove the spin accumulation in semiconductor.

The main outcome of this research is that we have identified the major obstacles to the electrical spin injection and detection in Si in the diffusive transport regime, and provided an innovative solution to these major obstacles. This thesis presents the interface engineering of spin tunnel contacts with an interfacial nanolayer, which makes a bridge across the fundamental mismatch between a ferromagnetic metal contact and a Si channel. We have used Gd to demonstrate the approach with a low-work-function nanolayer at the electrode side of the contact, while Cs was used to illustrate the approach in which the chemistry of the Si/Al₂O₃ interface is modified. However, these approaches are certainly not limited to Gd or Cs. Gd represents one example of a whole new category of tunnel contact materials combining high TSP with low work function. Among thousands of ferromagnetic metals, magnetic alloys, and magnetic oxides, there might be better materials in the sense of higher TSP, higher T_C , lower work function, and better chemical-stability than Gd. We may expect an enhanced TSP using other ferromagnets and barrier materials, or engineering the magnetic coupling of the nm-thin low work-function interlayer to a ferromagnetic material with high Curie temperature.

The methods developed here to engineer spin-tunnel contacts to Si can also be applied to other semiconductors in spintronic devices. Examples are in spin-tunnel contacts for spin-injection into organic semiconductors, semiconductor carbon nanotubes, graphene, Ge, some III-V semiconductors, and so on. This technique is not only essential to semiconductor-based spintronics, but may also find their way to low RA product applications of MTJs such as read heads in magnetic disk drives. This method could prove useful when the desired RA product is so small that the required thickness of the tunnel barrier enters the range where pinholes can no longer be avoided. The work function engineering using an interfacial nanolayers is more generally applicable than using it to control the RA product in spin devices. This technique is relevant for metal gates in MOSFETs, in contacts to organics, and, in fact, in any device where work function is important.

Bibliography

- [1] J. Bardeen and W. H. Brattain, "The Transistor, a Semi-Conductor Triode," *Physical Review* **74** (2), 230-231 (1948).
- [2] S. A. Wolf, D. D. Awschalom, R. A. Buhrman *et al.*, "Spintronics: A spin-based electronics vision for the future," *Science* **294**, 1488-1495 (2001).
- [3] I. Žutić, J. Fabian, and S. Das Sarma, "Spintronics: Fundamentals and applications," *Reviews of Modern Physics* **76** (2), 323-410 (2004).
- [4] S. Parkin, X. Jiang, C. Kaiser *et al.*, "Magnetically engineered spintronic sensors and memory," *Proceedings of the IEEE* **91** (5), 661-680 (2003).
- [5] M. N. Baibich, J. M. Broto, A. Fert *et al.*, "Giant Magnetoresistance of (001)Fe/(001)Cr Magnetic Superlattices," *Physical Review Letters* **61** (21), 2472-2475 (1988).
- [6] G. Binasch, P. Grünberg, F. Saurenbach *et al.*, "Enhanced Magnetoresistance in Layered Magnetic-Structures with Antiferromagnetic Interlayer Exchange," *Physical Review B* **39** (7), 4828-4830 (1989).
- [7] B. Dieny, V. S. Speriosu, S. S. P. Parkin *et al.*, "Giant Magnetoresistance in Soft Ferromagnetic Multilayers," *Physical Review B* **43** (1), 1297-1300 (1991).
- [8] R. Meservey and P. M. Tedrow, "Spin-Polarized Electron-Tunneling," *Physics Reports-Review Section of Physics Letters* **238** (4), 173-243 (1994); P. M. Tedrow and R. Meservey, "Spin Polarization of Electrons Tunneling from Films of Fe, Co, Ni, and Gd," *Physical Review B* **7** (1), 318-326 (1973).
- [9] J. S. Moodera, L. R. Kinder, T. M. Wong *et al.*, "Large Magnetoresistance at Room-Temperature in Ferromagnetic Thin-Film Tunnel-Junctions," *Physical Review Letters* **74** (16), 3273-3276 (1995).

- [10] T. Miyazaki and N. Tezuka, "Giant Magnetic Tunneling Effect in Fe/Al₂O₃/Fe Junction," *Journal of Magnetism and Magnetic Materials* **139** (3), L231-L234 (1995).
- [11] S. Tehrani, J. M. Slaughter, M. Deherra *et al.*, "Magnetoresistive random access memory using magnetic tunnel junctions," *Proceedings of the IEEE* **91** (5), 703-714 (2003).
- [12] H. Ohno, "Making nonmagnetic semiconductors ferromagnetic," *Science* **281**, 951-956 (1998); H. Ohno, D. Chiba, F. Matsukura *et al.*, "Electric-field control of ferromagnetism," *Nature* **408**, 944-946 (2000).
- [13] D. J. Monsma, J. C. Lodder, T. J. A. Popma *et al.*, "Perpendicular Hot-Electron Spin-Valve Effect in a New Magnetic-Field Sensor - the Spin-Valve Transistor," *Physical Review Letters* **74** (26), 5260-5263 (1995); D. J. Monsma, R. Vlutters, and J. C. Lodder, "Room temperature - Operating spin-valve transistors formed by vacuum bonding," *Science* **281**, 407-409 (1998).
- [14] K. Mizushima, T. Kinno, T. Yamauchi *et al.*, "Energy-dependent hot electron transport across a spin-valve," *IEEE Transactions on Magnetics* **33** (5), 3500-3504 (1997).
- [15] R. Jansen, "The spin-valve transistor: a review and outlook," *Journal of Physics D-Applied Physics* **36** (19), R289-R308 (2003).
- [16] A. Fert, J. M. George, H. Jaffrès *et al.*, "Semiconductors between spin-polarized sources and drains," *IEEE Transactions on Electron Devices* **54** (5), 921-932 (2007).
- [17] D. D. Awschalom and M. E. Flatte, "Challenges for semiconductor spintronics," *Nature Physics* **3** (3), 153-159 (2007).
- [18] M. E. Flatte, "Spintronics," *IEEE Transactions on Electron Devices* **54** (5), 907-920 (2007).
- [19] S. Datta and B. Das, "Electronic analog of the electro-optic modulator," *Appl. Phys. Lett.* **56**, 665-667 (1990).
- [20] M. Tanaka and S. Sugahara, "MOS-based spin devices for reconfigurable logic," *IEEE Transactions on Electron Devices* **54** (5), 961-976 (2007).
- [21] S. Sugahara, "Spin metal-oxide-semiconductor field-effect transistors (spin MOS-FETs) for integrated spin electronics," *IEE Proc. Circuits Devices Syst.* **152**, 355-365 (2005).
- [22] H. Saito, S. Yuasa, K. Ando *et al.*, "Spin-polarized tunneling in metal-insulator-semiconductor Fe/ZnSe/Ga_{1-x}Mn_xAs magnetic tunnel diodes," *Applied Physics Letters* **89** (23), 232502 (2006).

- [23] W. Van Roy, P. Van Dorpe, R. Vanheertum *et al.*, "Spin injection and detection in semiconductors - Electrical issues and device aspects," *IEEE Transactions on Electron Devices* **54** (5), 933-944 (2007).
- [24] B. T. Jonker, "Progress toward electrical injection of spin-polarized electrons into semiconductors," *Proceedings of the IEEE* **91** (5), 727-740 (2003).
- [25] G. Schmidt, D. Ferrand, L. W. Molenkamp *et al.*, "Fundamental obstacle for electrical spin injection from a ferromagnetic metal into a diffusive semiconductor," *Physical Review B* **62** (8), R4790-R4793 (2000).
- [26] E. I. Rashba, "Theory of electrical spin injection: Tunnel contacts as a solution of the conductivity mismatch problem," *Physical Review B* **62** (24), R16267-R16270 (2000).
- [27] A. Fert and H. Jaffrès, "Conditions for efficient spin injection from a ferromagnetic metal into a semiconductor," *Physical Review B* **64** (18), 184420 (2001).
- [28] J. M. Kikkawa and D. D. Awschalom, "Lateral drag of spin coherence in gallium arsenide," *Nature* **397**, 139-141 (1999).
- [29] R. Fiederling, M. Keim, G. Reuscher *et al.*, "Injection and detection of a spin-polarized current in a light-emitting diode," *Nature* **402**, 787-790 (1999).
- [30] Y. Ohno, D. K. Young, B. Beschoten *et al.*, "Electrical spin injection in a ferromagnetic semiconductor heterostructure," *Nature* **402**, 790-792 (1999).
- [31] V. F. Motsnyi, J. De Boeck, J. Das *et al.*, "Electrical spin injection in a ferromagnet/tunnel barrier/semiconductor heterostructure," *Applied Physics Letters* **81** (2), 265-267 (2002).
- [32] O. M. J. van 't Erve, G. Kioseoglou, A. T. Hanbicki *et al.*, "Comparison of Fe/Schottky and Fe/Al₂O₃ tunnel barrier contacts for electrical spin injection into GaAs," *Applied Physics Letters* **84** (21), 4334-4336 (2004).
- [33] X. Jiang, R. Wang, R. M. Shelby *et al.*, "Highly spin-polarized room-temperature tunnel injector for semiconductor spintronics using MgO(100)," *Physical Review Letters* **94** (5), 056601 (2005).
- [34] S. A. Crooker, M. Furis, X. Lou *et al.*, "Imaging spin transport in lateral ferromagnet/semiconductor structures," *Science* **309** (5744), 2191-2195 (2005).
- [35] J. M. Kikkawa, and D. D. Awschalom, "Resonant spin amplification in *n*-type GaAs," *Phys. Rev. Lett.* **80**, 4313-4316 (1998).
- [36] X. H. Lou, C. Adelmann, S. A. Crooker *et al.*, "Electrical detection of spin transport in lateral ferromagnet-semiconductor devices," *Nature Physics* **3** (3), 197-202 (2007).

- [37] Z. G. Yu and M. E. Flatte, "Electric-field dependent spin diffusion and spin injection into semiconductors," *Physical Review B* **66** (20), 201202 (2002); Z. G. Yu and M. E. Flatte, "Spin diffusion and injection in semiconductor structures: Electric field effects," *Physical Review B* **66** (23), 235302 (2002).
- [38] A. T. Filip, J. J. H. M. Schoonus, H. J. M. Swagten *et al.*, "Towards all electrical spin injection and detection in GaAs in a lateral geometry," *Journal of Superconductivity* **18** (3), 379-384 (2005).
- [39] Y. Q. Jia, R. C. Shi, and S. Y. Chou, "Spin-valve effects in nickel/silicon/nickel junctions," *IEEE Transactions on Magnetics* **32** (5), 4707-4709 (1996).
- [40] R. Klasges, C. Carbone, W. Eberhardt *et al.*, "Formation of a ferromagnetic silicide at the Fe/Si(100) interface," *Physical Review B* **56** (17), 10801-10804 (1997).
- [41] R. D. Thompson, B. Y. Tsaui, and K. N. Tu, "Contact Reaction between Si and Rare-Earth-Metals," *Applied Physics Letters* **38** (7), 535-537 (1981).
- [42] W. E. Beadle, J. C. C. Tsai, and R. D. Plummer (eds) *Quick reference manual for silicon integrated circuit technology* (Wiley, New York, 1984).
- [43] B. G. Park, T. Banerjee, B. C. Min *et al.*, "Tunnel spin polarization of Ni₈₀Fe₂₀/SiO₂ probed with a magnetic tunnel transistor," *Physical Review B* **73** (17), 172402 (2006).
- [44] J. Bardeen, "Surface states and rectification at a metal semiconductor contact" *Phys. Rev.* **71**, 717-727 (1947).
- [45] S. M. Sze, *Physics of Semiconductor Devices*, 2nd ed. (Wiley and Sons, New York, 1981); A. M. Cowley and S. M. Sze, "Surface States and Barrier Height of Metal-Semiconductor Systems," *Journal of Applied Physics* **36** (10), 3212 (1965).
- [46] V. Heine, "Theory of Surface States," *Physical Review* **138** (6A), 1689 (1965).
- [47] R. T. Tung, "Recent advances in Schottky barrier concepts," *Materials Science and Engineering R-Reports* **35**, 1-138 (2001); R. T. Tung, "Chemical bonding and Fermi level pinning at metal-semiconductor interfaces," *Physical Review Letters* **84** (26), 6078-6081 (2000); R. T. Tung, "Formation of an electric dipole at metal-semiconductor interfaces," *Physical Review B* **64** 205310 (2001).
- [48] J. Tersoff, "Schottky-Barrier Heights and the Continuum of Gap States," *Physical Review Letters* **52** (6), 465-468 (1984).
- [49] S. O. Valenzuela, D. J. Monsma, C. M. Marcus, V. Narayanamurti, and M. Tinkham, "Spin polarized tunneling at finite bias," *Phys. Rev. Lett.* **94**, 196601 (2005).

- [50] B. C. Min, K. Motohashi, J. C. Lodder, and R Jansen, "Tunable spin-tunnel contacts to silicon using low-work-function ferromagnets," *Nature Materials* **5** 817 (2006) ; B. C. Min, K. Motohashi, J. C. Lodder, and R Jansen, "Cobalt-Al₂O₃-silicon tunnel contacts for electrical spin injection into silicon," *J. Appl. Phys.* **99** 08s701 (2006).
- [51] J. G. Simmons, "Generalized formula for the electric tunnel effect between similar electrodes separated by a thin insulating film," *J. Appl. Phys.* **34**, 1793 (1963).
- [52] C. A. Mead and W. G. Spitzer, "Fermi Level Position at Semiconductor Surfaces," *Physical Review Letters* **10** (11), 471 (1963); W. G. Spitzer and C. A. Mead, "Barrier Height Studies on Metal-Semiconductor Systems," *Journal of Applied Physics* **34** (10), 3061 (1963).
- [53] L. Pantisano, T. Schram, B. O'Sullivan *et al.*, "Effective work function modulation by controlled dielectric monolayer deposition," *Applied Physics Letters* **89** (11), 113505 (2006).
- [54] W. Van Roy, P. Van Dorpe, J. De Boeck, and G. Borghs, "Spin injection in LED's and in unipolar devices," *Materials Science and Engineering B* **126** 155-163 (2006).
- [55] H. B. Michaelson, "The work function of the elements and its periodicity," *J. Appl. Phys.* **48**, 4729-4733 (1977).
- [56] D. Connelly, C. Faulkner, P. A. Clifton, and D. E. Grupp, "Fermi-level depinning for low-barrier Schottky source/drain transistors," *Appl. Phys. Lett.* **88**, 12105 (2006).
- [57] K. N. Tu, R. D. Thompson, and B. Y. Tsauer, "Low Schottky barrier of rare-earth silicide on *n*-Si," *Appl. Phys. Lett.* **38**, 626-628 (1981).
- [58] R. Meservey, D. Paraskevoopoulos, and P. M. Tedrow, "Tunneling measurements of conduction-electron-spin polarization in heavy rare-earth metals," *Physical Review B* **22**, 1331-1337 (1980).
- [59] B. Y. Tsui and C. F. Huang, "Wide range work function modulation of binary alloys for MOSFET application," *IEEE Electron Device Letters* **24** (3), 153-155 (2003); C. D. Gelatt and Ehrenrei.H, "Charge-Transfer in Alloys - AgAu," *Physical Review B* **10** (2), 398-415 (1974).
- [60] R. F. Egerton, *Electron-Energy Loss Spectroscopy in the electron microscope*, 2nd ed. (Springer, New York, 1996).
- [61] M. B. Stearns, "Simple Explanation of Tunneling Spin-Polarization of Fe, Co, Ni and Its Alloys," *Journal of Magnetism and Magnetic Materials* **5** (2), 167-171 (1977).
- [62] J. C. Slonczewski, "Conductance and Exchange Coupling of 2 Ferromagnets Separated by a Tunneling Barrier," *Physical Review B* **39** (10), 6995-7002 (1989).

- [63] E. Y. Tsymbal, O. N. Mryasov, and P. R. LeClair, "Spin-dependent tunnelling in magnetic tunnel junctions," *Journal of Physics-Condensed Matter* **15** (4), R109-R142 (2003).
- [64] W. H. Butler, X. G. Zhang, T. C. Schulthess *et al.*, "Spin-dependent tunneling conductance of Fe vertical bar MgO vertical bar Fe sandwiches," *Physical Review B* **63** (5), 054416 (2001).
- [65] S. S. P. Parkin, C. Kaiser, A. Panchula *et al.*, "Giant tunnelling magnetoresistance at room temperature with MgO (100) tunnel barriers," *Nature Materials* **3** (12), 862-867 (2004).
- [66] S. Yuasa, T. Nagahama, A. Fukushima *et al.*, "Giant room-temperature magnetoresistance in single-crystal Fe/MgO/Fe magnetic tunnel junctions," *Nature Materials* **3** (12), 868-871 (2004).
- [67] J. M. De Teresa, A. Barthelemy, A. Fert *et al.*, "Role of metal-oxide interface in determining the spin polarization of magnetic tunnel junctions," *Science* **286** (5439), 507-509 (1999).
- [68] M. Julliere, "Tunneling between Ferromagnetic-Films," *Physics Letters A* **54** (3), 225-226 (1975).
- [69] B. G. Park, T. Banerjee, B. C. Min *et al.*, "Temperature dependence of magnetocurrent in a magnetic tunnel transistor," *Journal of Applied Physics* **98** (10), 103701 (2005).
- [70] R.J. Gambino, "Rare earth-transition metal amorphous alloy media", R.J. Gambino and T. Suzuki eds. *Magneto-optical recording materials* (IEEE Press, New York, 2000).
- [71] P. Hansen, "Magnetic amorphous alloys", K.H.J. Buschow eds. *Handbook of magnetic materials* vol **6** (North-Holland, Amsterdam, 1991).
- [72] K. Moorjani and J.M.D. Coey, *Magnetic glasses* (Elsevier, Amsterdam, 1984).
- [73] S. Legvold, "Rare earth metals and alloys", E. P. Wohlfarth eds. *Ferromagnetic materials* vol **1** (North-Holland, Amsterdam, 1980).
- [74] P. Hansen, C. Clausen, G. Much *et al.*, "Magnetic and Magneto-Optical Properties of Rare-Earth Transition-Metal Alloys Containing Gd, Tb, Fe, Co," *Journal of Applied Physics* **66** (2), 756-767 (1989).
- [75] T. R. McGuire and R. J. Gambino, "Magnetic and Transport Properties of Gd-Ni Amorphous Alloys," *IEEE Transactions on Magnetics* **14** (5), 838-840 (1978).
- [76] M. Farle, K. Baberschke, U. Stetter *et al.*, "Thickness-Dependent Curie-Temperature of Gd(0001)/W(110) and Its Dependence on the Growth-Conditions," *Physical Review B* **47** (17), 11571-11574 (1993).

- [77] R. E. Camley, "Properties of Magnetic Superlattices with Antiferromagnetic Interfacial Coupling - Magnetization, Susceptibility, and Compensation Points," *Physical Review B* **39** (16), 12316-12319 (1989); R. E. Camley and D. R. Tilley, "Phase-Transitions in Magnetic Superlattices," *Physical Review B* **37** (7), 3413-3421 (1988); O. F. K. McGrath, N. Ryzhanova, C. Lacroix *et al.*, "Observation and interpretation of a partial Gd twisted spin state in an epitaxial Gd/Fe bilayer," *Physical Review B* **54** (9), 6088-6091 (1996); J. L. Prieto, B. B. van Aken, G. Burnell *et al.*, "Transport properties of sharp antiferromagnetic boundaries in Gd/Fe multilayers," *Physical Review B* **69** (5), - (2004).
- [78] J. P. Andres, J. L. Sacedon, J. Colino *et al.*, "Interdiffusion up to the eutectic composition and vitrification in Gd/Co multilayers," *Journal of Applied Physics* **87** (5), 2483-2489 (2000).
- [79] A. Niemeyer and G. Reiss, "Magnetic tunnel junctions with compensated magnetic moment by directly exchange-coupled NiFe/CoGd/NiFe trilayers," *Applied Physics Letters* **88** (18), 182503 (2006); Y. H. Fan and H. Bruckl, "Magnetic moment compensation in exchange-biased trilayers with antiparallel spin alignment," *Applied Physics Letters* **83** (15), 3138-3140 (2003).
- [80] R. Ranchal, C. Aroca, and E. Lopez, "In-plane magnetotransport properties of Permalloy/gadolinium/Permalloy trilayers," *Journal of Applied Physics* **100** (10), 103903 (2006); R. Ranchal, C. Aroca, M. C. Sanchez *et al.*, "Improvement of the structural and magnetic properties of Permalloy/Gadolinium multilayers with Mo spacers," *Applied Physics a-Materials Science and Processing* **82** (4), 697-701 (2006); R. Ranchal, C. Aroca, M. C. Sanchez *et al.*, "Effective exchange coupling in permalloy-gadolinium films," *Physica Status Solidi a-Applications and Materials Science* **203** (6), 1415-1419 (2006).
- [81] R. Jansen and J. S. Moodera, "Magnetoresistance in doped magnetic tunnel junctions: Effect of spin scattering and impurity-assisted transport," *Physical Review B* **61** (13), 9047-9050 (2000).
- [82] C. Kaiser, A. F. Panchula, and S. S. P. Parkin, "Finite tunneling spin polarization at the compensation point of rare-earth-metal-transition-metal alloys," *Physical Review Letters* **95** (4), 047202 (2005); C. Kaiser, S. van Dijken, S. H. Yang *et al.*, "Role of tunneling matrix elements in determining the magnitude of the tunneling spin polarization of 3d transition metal ferromagnetic alloys," *Physical Review Letters* **94** (24), 247203 (2005).
- [83] C. Kittel, *Introduction to solid state physics*, 7th ed. (John Wiley, New York, , 1996).
- [84] M. A. Uijttewaal, G. A. de Wijs, R. A de Groot *et al.* "Interrelation of work function and surface stability: the case of BaAl₄," *Chem. Mater.* **17**, 3879-3882 (2005).

- [85] C. S. Wang, "High Photoemission Efficiency of Submonolayer Cesium-Covered Surfaces," *Journal of Applied Physics* **48** (4), 1477-1479 (1977); E. P. Gyftopoulos and J. D. Levine, "Work Function Variation of Metals Coated by Metallic Films," *Journal of Applied Physics* **33** (1), 67 (1962).
- [86] H. Mimura, Y. Neo, H. Shimawaki *et al.*, "Improvement of the emission current from a cesiated metal-oxide-semiconductor cathode," *Applied Physics Letters* **88** (12), 123514 (2006).
- [87] E. Wimmer, A. J. Freeman, M. Weinert *et al.*, "Cesiation of W(001) - Work Function Lowering by Multiple Dipole Formation," *Physical Review Letters* **48** (16), 1128-1131 (1982).
- [88] M. Succi, R. Canino, and B. Ferrario, "Atomic-Absorption Evaporation Flow-Rate Measurements of Alkali-Metal Dispensers," *Vacuum* **35** (12), 579-582 (1985).
- [89] J. D. Levine, "Structural and Electronic Model of Negative Electron Affinity on Si-Cs-O Surface," *Surface Science* **34** (1), 90-107 (1973); Goldstein.B, "Leed, Auger and Plasmon Studies of Negative Electron Affinity on Si Produced by Adsorption of Cs and O," *Surface Science* **35** (1), 227-245 (1973); J. E. Ortega, E. M. Oellig, J. Ferron *et al.*, "Cs and O Adsorption on Si(100) 2 X-1 - a Model System for Promoted Oxidation of Semiconductors," *Physical Review B* **36** (11), 6213-6216 (1987).
- [90] R. Biagi, P. Fantini, V. De Renzi *et al.*, "Photoemission investigation of the alkali-metal-induced two-dimensional electron gas at the Si(111)(1x1): H surface," *Physical Review B* **67** (15), 155325 (2003); Y. C. Chao, L. S. O. Johansson, and R. I. G. Uhrberg, "Adsorption of Na on Si(100)2x1 at room temperature studied with photoelectron spectroscopy," *Physical Review B* **55** (11), 7198-7205 (1997); N. Takagi, N. Minami, and M. Nishijima, "Electron-Scattering from the K-Exposed Si(100)(2x1)-H Surface," *Physical Review B* **45** (23), 13524-13530 (1992).
- [91] A. Hubert and R. Schafer, *Magnetic domains: The analysis of magnetic microstructures*, (Springer, Berlin, 1998).
- [92] E. H. Frei and W. F. Brown, "Fundamental Theorem of Fine-Ferromagnetic-Particle Theory," *Journal of Applied Physics* **39** 993 (1968).
- [93] E. C. Stoner and E. P. Wohlfarth, "A Mechanism of Magnetic Hysteresis in Heterogeneous Alloys," *Philosophical Transactions of the Royal Society of London Series a-Mathematical and Physical Sciences* **240** (826), 599-642 (1948).
- [94] R. P. Cowburn and M. E. Wetland, "Phase transitions in planar magnetic nanostructures," *Applied Physics Letters* **72** (16), 2041-2043 (1998); R. P. Cowburn, D. K. Koltsov, A. O. Adeyeye *et al.*, "Single-domain circular nanomagnets," *Physical Review Letters* **83** (5), 1042-1045 (1999).

- [95] C. A. Ross, M. Hwang, M. Shima *et al.*, "Micromagnetic behavior of electrodeposited cylinder arrays," *Physical Review B* **65** (14), - (2002); C. A. Ross, H. I. Smith, T. Savas *et al.*, "Fabrication of patterned media for high density magnetic storage," *Journal of Vacuum Science and Technology B* **17** (6), 3168-3176 (1999).
- [96] X. X. Liu, J. N. Chapman, S. McVitie *et al.*, "Introduction and control of metastable states in elliptical and rectangular magnetic nanoelements," *Applied Physics Letters* **84** (22), 4406-4408 (2004).
- [97] T. A. Brunner, "Why optical lithography will live forever", *Journal of Vacuum Science and Technology B* **21**(6) 2632 (2003).
- [98] W. Hinsberg, F. A. Houle, J. Hoffnagle *et al.*, "Deep-ultraviolet interferometric lithography as a tool for assessment of chemically amplified photoresist performance," *Journal of Vacuum Science and Technology B* **16** (6),3689-3694 (1998).
- [99] M. Farhoud, J. Ferrera, A. J. Lochtefeld *et al.*, "Fabrication of 200 nm period nanomagnet arrays using interference lithography and a negative resist," *Journal of Vacuum Science and Technology B* **17** (6), 3182-3185 (1999).
- [100] A. Fernandez, J. Y. Decker, S. M. Herman *et al.*, "Methods for fabricating arrays of holes using interference lithography," *Journal of Vacuum Science and Technology B* **15** (6), 2439-2443 (1997).
- [101] R. Murillo, Magnetic media patterned by laser interference lithography, PhD thesis, (University of Twente, Enschede, 2006).
- [102] J. Y. Decker, A. Fernandez, and D. W. Sweeney, "Generation of subquarter-micron resist structures using optical interference lithography and image reversal," *Journal of Vacuum Science and Technology B* **15** (6), 1949-1953 (1997).
- [103] S. Wolf and R. N. Tauber, *Silicon processing for the VLSI era*, volume 1, (Lattice press, Sunset Beach, 1987) 407-458.
- [104] AZ5214E, image reversal photoresist, product data sheet, Clariant Corp.
- [105] G. N. Taylor, "Forefront of photolithographic materials", in R. A. Levy ed., *Microelectronics Materials and Processes*, (Kluwer, Dordrecht, 1989)341-407.
- [106] TI09XR, image reversal resist, technical data sheet, Microchemicals GmbH.
- [107] R. J. Schutz, "Reactive plasma etching" in S. M. Sze ed., *VLSI Technology*, (McGraw-Hill, Singapore, 1988) 184-232.
- [108] P. G.. Glöersen, "Ion beam etching", *J. Vac. Sci. Technol.* **12** (1), 28 (1975); R. E. Lee, "Microfabrication by ion beam etching", *J. Vac. Sci. Technol.* **16**(2), 164 (1979); O. Auciello, "Ion interaction with solids: Surface texturing, some bulk effects, and their

- possible applications", *J. Vac. Sci. Technol.* **19**(4) 841 (1981); P. R. Puckett, S. L. Michel, and W. E. Hughes, "Ion Beam Etching" in J. L. Vossen and W. Kern ed., *Thin film processes II*, (Academic Press, San Diego, 1991) 749-782.
- [109] Y. Martin and H. K. Wickramasinghe, "Magnetic Imaging by Force Microscopy with 1000-Å Resolution," *Applied Physics Letters* **50** (20), 1455-1457 (1987).
- [110] T. Shinjo, T. Okuno, R. Hassdorf *et al.*, "Magnetic vortex core observation in circular dots of permalloy," *Science* **289** (5481), 930-932 (2000).
- [111] A. Wachowiak, J. Wiebe, M. Bode *et al.*, "Direct observation of internal spin structure of magnetic vortex cores," *Science* **298** (5593), 577-580 (2002).
- [112] M. J. Donahue and D.G. Porter, *OOMMF User's Guide*, Version 1.0 Interagency Report NISTIR 6376, National Institute of Standards and Technology, Gaithersburg, MD (Sept 1999).
- [113] E. Haq, T. Banerjee, M. H. Siekman *et al.*, "Ballistic hole magnetic microscopy," *Applied Physics Letters* **86** (8), 082502 (2005); E. Haq, H. Gokcan, T. Banerjee *et al.*, "Nanoscale magnetic hysteresis of Ni₈₀Fe₂₀/Au/Co trilayers using ballistic electron magnetic microscopy," *Journal of Applied Physics* **95** (11), 6930-6932 (2004).
- [114] D. O. Smith, M. S. Cohen, and G. P. Weiss, "Oblique-Incidence Anisotropy in Evaporated Permalloy Films," *Journal of Applied Physics* **31** (10), 1755-1762 (1960).
- [115] A. G. Dirks and H. J. Leamy, "Columnar Microstructure in Vapor-Deposited Thin-Films," *Thin Solid Films* **47** (3), 219-233 (1977).
- [116] M. Grimsditch, Y. Jaccard, and I. K. Schuller, "Magnetic anisotropies in dot arrays: Shape anisotropy versus coupling," *Physical Review B* **58** (17), 11539-11543 (1998).
- [117] C. Mathieu, C. Hartmann, M. Bauer *et al.*, "Anisotropic magnetic coupling of permalloy micron dots forming a square lattice," *Applied Physics Letters* **70** (21), 2912-2914 (1997).
- [118] R. P. Cowburn, A. O. Adeyeye, and M. E. Welland, "Configurational anisotropy in nanomagnets," *Physical Review Letters* **81** (24), 5414-5417 (1998).
- [119] M. Natali, A. Lebib, Y. Chen *et al.*, "Configurational anisotropy in square lattices of interacting cobalt dots," *Journal of Applied Physics* **91** (10), 7041-7043 (2002).
- [120] S. M. Weekes, F. Y. Ogrin, and P. S. Keatley, "Configurational anisotropy in hexagonal arrays of submicron Co elements," *Journal of Applied Physics* **99** (8), 08B102 (2006).
- [121] K. Y. Guslienko, "Magnetostatic interdot coupling in two-dimensional magnetic dot arrays," *Applied Physics Letters* **75** (3), 394-396 (1999).

-
- [122] L. J. Heyderman, H. H. Solak, C. David *et al.*, "Arrays of nanoscale magnetic dots: Fabrication by x-ray interference lithography and characterization," *Applied Physics Letters* **85** (21), 4989-4991 (2004).
- [123] F. J. Jedema, A. T. Filip, and B. J. van Wees, "Electrical spin injection and accumulation at room temperature in an all-metal mesoscopic spin valve," *Nature* **410** (6826), 345-348 (2001).
- [124] H. X. Tang, et al "Spin injection and transport in micro- and nanoscale devices" in *Semiconductor Spintronics and Quantum Computation*, eds. by D. Awschalom *et al.* (Springer, New York, 2002).
- [125] F. G. Monzon, M. Johnson, and M. L. Roukes, "Strong Hall voltage modulation in hybrid ferromagnet/semiconductor microstructure," *Applied Physics Letters* **71** (21), 3087-3089 (1997).
- [126] K. Seeger, *Semiconductor Physics: An introduction*, 3rd ed. (Springer-Verlag, Berlin, 1985).
- [127] G. L. Pearson and J. Bardeen, "Electrical Properties of Pure Silicon and Silicon Alloys Containing Boron and Phosphorus," *Physical Review* **75** (5), 865-883 (1949).

Appendices

Appendix A. Process details of the fabrication of MIS contacts

Wafer: *n*-type Si (100), thickness: 500 μm

A1 Oxide template patterning

A1.1 Standard wafer cleaning

100% HNO_3 , 10 min
Quick dump rinse (QDR) in de-ionized (DI) water
69% HNO_3 at 95°C, 10 min
QDR in DI water
1% HF, 1 min
QDR in DI water
Spin dry

A1.2 Dry oxidation

300 nm SiO_2 dry-oxide: 1100°C, 5 hours
Thickness measurement: ellipsometry

A1.3 SiO_2 pattern mask

Pre-bake 10 min at 120°C to remove water vapor
Spin coating an adhesion promoter, hexamethyldisilozane (HDMS) 20 sec, 4000 rpm
Spin coating 1.2 μm photoresist (PR) (Olin 907/1.2) 20 sec, 4000 rpm
Soft bake, 1 min at 95°C
Standard exposure (4.5 sec)
Post-bake exposure, 1 min at 120°C

Development OPD4262, 60 sec
QDR in DI water
Spin dry
Inspection with optical microscope

A1.4 SiO₂ etching

Ammonium fluoride buffer-hydrofluoric acid mixture (BHF)
BHF 5 min (Etch rate: 60 nm/min)
QDR in DI water PR strip HNO₃ 100%, 10 min
QDR in DI water
Spin dry
Inspection with optical microscope

A1.5 Standard wafer cleaning

100% HNO₃, 10 min
Quick dump rinse (QDR) in DI
69% HNO₃ at 95 °C, 10 min
QDR in DI water
1% HF, 1min
QDR in DI water
Spin dry

A1.6 Dry oxidation

40 nm SiO₂ dry-oxide: 950°C, 1 hour 20 min
Cool down to 400°C
Heat up to 1150°C
Annealing 30 min at 1150°C
Cool down to room temperature (RT)
Thickness measurement: ellipsometry

A1.7 Wafer dicing

Protect a wafer with PR.
Wafer is diced to 11 mm x 11 mm.

A2 Metal layer deposition

A2.1 wafer preparation (11 mm x 11 mm)

100% HNO₃, 10 min
DI water rinse, 7 min
BHF 1 min
DI water rinse, 1 min
Spin dry
Load the wafers in the deposition robot

Transfer the robot into the load-lock chamber

A2.2 Layer deposition

Al₂O₃ deposition by e-beam evaporation

Plasma oxidation at 800V, 100 mTorr

Metallic layer deposition

A3 Metal layer patterning

A3.1 Front-side metal pattern mask

Pre-bake 10 min at 120°C to remove water vapor

Spin coating 1.2 μm PR (Olin 907/1.2), 20 sec, 4000 rpm

Soft bake 1 min at 95°C

Standard exposure (4.5 sec)

Post-bake exposure 1 min at 120°C

Development OPD4262, 60 sec

QDR in DI water

Spin dry

Inspection with optical microscope

A3.2 Ion beam etching (IBE) of metal layers

Kaufman type broad beam source (21 cm)

with a plasma bridge neutralizer

with MPS5001 power supply (Veeco Instruments)

Ar pressure 3×10^{-4} mTorr

Discharge voltage= 55 V

Beam voltage= 500 V, Beam current= 20 mA

Acceleration voltage=100 V, Acceleration current = 1 mA

Plasma bridge neutralizer current = 25 mA

IBE for suitable time

with constant rotation of the sample at tilted angle 20°.

Cleaning IBE of edge-redeposition, 2 min at tilted angle 75°, if necessary

Inspection with optical microscope

A3.3 Photoresist (PR) strip

Removal of the backside paste with Isopropyl Alcohol (IPA)

Cleaning in IPA with ultrasonic agitation

PR strip in Acetone with ultrasonic agitation

Rinse in IPA

Rinse in DI water 1 min

Spin dry

Inspection with optical microscope

A4 Cr/Au contact pad patterning

A4.1 Front side Cr/Au pad pattern mask

Pre-bake 10 min at 120°C to remove water vapor

Spin coating HDMS 20 sec, 4000 rpm

Spin coating 1.2 μm PR (Olin 907/1.2), 20 sec, 4000 rpm

Softbake 1 min at 95°C

Standard exposure (4.5 sec)

Post-bake exposure 1 min at 120°C

Development OPD4262, 60 sec

QDR in DI water

Spin dry

Inspection with optical microscope

A4.2 Sputtering Cr/Au contacts on the front side

DC magnetron sputtering (sputterke)

Ar pressure= 6.6 mTorr, power=300W

Cr 12 nm/ Au 100 nm

Lift-off in Acetone with ultrasonic agitation

Rinse in IPA

Rinse in DI water 1 min

Spin dry

Inspection with optical microscope

Appendix B. Process details of the fabrication of the vertical geometry for two-terminal MR observation

Wafer : SOI wafer, *n*-type Si (100), Device layer: 0.5~3 μ m, Handle wafer: 350 μ m

B1 Membrane fabrication

B1.1 Standard wafer cleaning

100% HNO₃, 10 min
Quick dump rinse (QDR) in Deionized (DI) water
69% HNO₃ at 95°C, 10 min
QDR in DI water
1% HF, 1 min
QDR in DI water
Spin dry

B1.2 Wet oxidation

1000 nm: 2 hours 30 min at 1150°C
Thickness measurement with ellipsometer

B1.3 Backside mask

Pre-bake 10 min at 120°C to remove water vapor
Spin coating HDMS (20 sec, 4000 rpm)
Spin coating 1.2 μ m photoresist (PR: Olin 907/1.2) 20 sec, 4000 rpm
Softbake 1 min at 95°C
Standard Exposure (4.5 sec)
Post-exposure bake 1 min at 120°C
Development OPD4262, 60 sec
QDR in DI water
Spin dry
Inspection with optical microscope

B1.4 Front side protection

Spin coating HDMS (20 sec, 4000 rpm)
Spin coating 1.2 μ m PR (20 sec, 4000 rpm)
Softbake 1 min at 95 °C

B1.5 Oxide mask etching

Hardbake 15 min at 120 °C
Ammonium fluoride buffer-hydrofluoric acid mixture (BHF)
BHF 19 min (Etch rate: ~ 60 nm/min)
QDR in DI water
PR strip in 100% HNO₃, 10 min

QDR in DI water
Spin dry
Inspection with optical microscope

B1.6 Si etching

25 wt% KOH, 6 hours at 75 °C
(Etch rate: 1 nm/min for SiO₂, 1 μm/min for Si (001))
Inspection with optical microscope

B1.7 Wafer cleaning

RCA solution (H₂O:H₂O₂:HCl= 5:1:1), 15 min at 85°C
QDR in DI water
Spin dry

B2 Front side Si pattering

B2.1 Standard wafer cleaning

100% HNO₃, 10 min
QDR in DI water
69% HNO₃ at 95°C, 10 min
QDR in DI water
Spin dry

B2.2 Front-side Si pattern mask

Pre-bake 10 min at 120°C to remove the water vapor
Spin coating HDMS (20 sec, 4000 rpm)
Spin coating 1.2 μm PR (Olin 907/1.2), 20 sec 4000 rpm
Soft-bake 1 min at 95 °C
Standard Exposure (4.5 sec)
Post-exposure bake 1 min at 120°C
Development OPD4262, 60 sec
QDR in DI water
Spin dry
Inspection with optical microscope

B2.3 Oxide mask etching

Hardbake 15 min at 120°C
BHF 12 min (Etch rate: 60 nm/min)
*The backside Burried oxide (Box) layer is also etched in part at the same time.
QDR in DI water
PR strip HNO₃ 100%, 10 min
QDR in DI water
Spin dry

Inspection with optical microscope

B2.4 Front side Si etching

25 wt% KOH, 3 min at 75 °C

(Etch rate: 1 nm/min for SiO₂, 1 μm/min for Si (001))

*The backside Handle Si layer is etched at the same time.

Inspection with optical microscope

Inspection with Dektak (Thickness profile)

B2.5 Wafer cleaning

RCA solution (H₂O:H₂O₂:HCl= 5:1:1), 15 min at 85 °C

QDR in DI water

Spin dry

B3 Front-side SiO₂ patterning and backside BOX etching

B3.1 Standard wafer cleaning

HNO₃ 100%, 10 min

QDR in DI water

69% HNO₃ at 95°C, 10 min

QDR in DI water

Spin dry

B3.2 Front-side SiO₂ pattern mask

Pre-bake 10 min at 120°C to remove water vapor

Spin coating HDMS, 20 sec, 4000 rpm

Spin coating 1.2 μm PR (Olin 907/1.2), 20 sec, 4000 rpm

Soft-bake 1 min at 95°C

Standard exposure (4.5 sec)

Post-bake exposure 1 min at 120°C

Development OPD4262 60 sec

QDR in DI water

Spin dry

Inspection with optical microscope

B3.3 SiO₂ etching

BHF 7 min (Etch rate: 60 nm/min)

*The remaining backside Box layer is completely etched at the same time.

QDR in DI water

PR strip HNO₃ 100%, 10 min

QDR in DI water

Spin dry

Inspection with optical microscope

B3.4 Standard wafer cleaning

100% HNO₃, 10 min
Quick dump rinse (QDR) in DI
69% HNO₃ at 95°C, 10 min
QDR in DI water
1% HF, 1 min
QDR in DI water
Spin dry

B3.5 Dry oxidation

40 nm SiO₂ dry oxide: 1 hour 20 min at 950°C
Cool down to 400°C
Heat up to 1150°C
Annealing 30 min at 1150°C
Cool down to RT
Thickness measurement: ellipsometry

B3.6 Front-side protection SiO₂ deposition

RF sputtering (Nordiko)
Pressure=7.5 mTorr (Oxygen:Ar=1:9), Power= 300 W
Deposition time= 30 min, thickness= ~80 nm

B3.7 Wafer dicing

Protect a wafer with PR
Wafer is diced to 11 mm x 11 mm.

B4 Metal layer deposition**B4.1 wafer preparation (11 mm x 11 mm)**

100% HNO₃, 10 min
DI water rinse, 7 min
BHF 1 min
DI water rinse, 1 min
Spin dry
Load the wafers in the deposition robot.
Transfer the robot into the load-lock chamber.

B4.2 Layer deposition on the backside

Al₂O₃ deposition by e-beam evaporation
Plasma oxidation at 800 V, 100 mTorr
Metallic layer deposition

B4.3 Sputtering the Cr/Au contact on the backside

DC magnetron sputtering (sputterke)
Ar pressure=6.6 mTorr, power=300 W
Cr 12 nm/ Au 100 nm

B4.4 Removal of front side SiO₂

BHF, 1 min
DI water rinse, 1 min
Spin dry
Load the wafers in the deposition robot.
Transfer the robot into the loadlock chamber.

B4.5 Layer deposition on the front-side

Al₂O₃ deposition by e-beam evaporation
Plasma oxidation at 800 V, 100 mTorr
Metallic layer deposition

B5 Metal layer patterning**B5.1 Front side metal pattern mask**

Pre-bake 10 min at 120°C to remove water vapor
Spin coating HDMS, 20 sec, 4000 rpm
Spin coating 1.2 μm PR (Olin 907/1.2), 20 sec, 4000 rpm
Soft-bake 1 min at 95°C
Standard exposure (4.5 sec)
Post-bake exposure 1 min at 120°C
Development OPD4262, 60 sec
QDR in DI water
Spin dry
Inspection with optical microscope

B5.2 Wet etching of metal layer

Au etchant (KI 34 g, I₂ 4.5 g, Glycerol 150 ml, Water 300 ml)
1:20 diluted Au etchant (Au etchant: Glycerol : DI water:= 15: 100: 200)
Backside protection with PR
60 sec in standard Al etchant at 55°C
60 sec in the diluted Au etchant
Remaining time in Al etchant
Rinse in DI water 1 min
Spin dry
Inspection with optical microscope
PR strip in Acetone (No ultrasonic agitation)
Rinse in Isopropyl Alcohol (IPA)

Rinse in DI water 1 min
Spin dry
Inspection with optical microscope

B6 Cr/Au contact pad patterning

B6.1 Front-side Cr/Au pad pattern mask

Pre-bake 10 min at 120 °C to remove water vapor
Spin coating HDMS 20 sec, 4000 rpm
Spin coating 1.2 μm PR (Olin 907/1.2), 20 sec, 4000 rpm
Soft-bake 1 min at 95°C
Standard exposure (4.5 sec)
Post-bake exposure 1 min at 120°C
Development OPD4262, 60 sec
QDR in DI water
Spin dry
Inspection with optical microscope

B6.2 Sputtering Cr/Au contacts on the front side

DC magnetron sputtering (sputterke)
Ar pressure=6.6 mTorr, power=300 W
Cr 12 nm/ Au 100 nm
Lift-off in Acetone (No ultrasonic agitation)
Rinse in IPA
Rinse in DI water 1 min
Spin dry
Inspection with optical microscope

Summary

This thesis is devoted to silicon-based spintronic devices, and describes the investigation of the issues for the development of such devices, and provides solutions towards realization thereof. By combining ferromagnetic properties and semiconductor characteristics and using the spin of the electron, semiconductor-based spintronics opens up the possibility to realize novel electronic devices. One example is the silicon spin-MOSFET, a gate-controlled magneto-resistive device with a silicon channel and a ferromagnetic source and drain, in which the channel conductance can be modulated by the relative alignment of the source and drain magnetization. Silicon is most attractive as the material for the semiconductor channel not only because of its use in mainstream semiconductor technology, but also because Si is expected to have a long spin lifetime.

For the realization of this device and the observation of magnetoresistance (MR) between source and drain, the electrical injection, transport, and detection of spin-polarized carriers in Si are required. This, in turn, requires proper design of the contacts between the ferromagnetic source/drain and the semiconductor, as these determine the communication of the spin information between the channel and the ferromagnetic electrodes. This thesis starts by outlining what the requirements are for the ferromagnetic metal/ tunnel barrier/ Si (FM/I/Si) contacts in order to allow the observation of MR in such devices. These are a suitable resistance-area (RA) product, high tunnel spin-polarization (TSP), and controlled magnetic switching.

To examine these requirements, FM/ Al_2O_3 / Si structures are studied. It is found that the observation of MR in a Si spin-MOSFET is not possible with such FM contacts if common ferromagnetic metals such as Co and NiFe al-

loys are used. Also, the conventional method of adjusting the tunnel barrier thickness to control the tunnel conductance is found to be ineffective. The resistance of FM/I/Si contacts with Co and NiFe alloys is 4 to 8 orders of magnitude too large. Schottky barrier formation in the FM/I/Si contacts is identified as the main reason.

This thesis presents a solution to this problem by interface engineering of spin tunnel contacts using a sub-nm interfacial nanolayer, bridging the ferromagnetic metal and the Si channel. Two approaches are introduced and demonstrated. The first approach involves a nanolayer of a ferromagnetic material with a low work function, inserted at the magnetic electrode side of the contact. It is demonstrated that FM/I/Si contacts with Gd-based low-work-function ferromagnetic electrodes have greatly reduced RA products, because the Schottky barrier is effectively removed. Moreover, by adjusting the thickness of the nanolayer, tuning of Schottky barrier height and thereby the RA product can be achieved over 8 orders of magnitude. Simultaneously, it is demonstrated that a reasonable tunnel spin-polarization is still preserved, although some improvement in the room temperature values would be desirable. A few material modifications are therefore also studied, although many more options are still to be explored.

The second approach to control the RA product of the FM/I/Si contacts uses alkali-metal (Cs) coverage of the Si surface prior to tunnel barrier preparation. This is also found to suppress the Schottky barrier height efficiently, due to the modified pinning position of the Fermi level at the oxide/Si interface. By combining the second "interface chemistry" method with the low work-function approach, one has complete control of the RA product as well as potential energy profile of spin tunnel contacts to Si. Especially, an inverted band bending can be obtained in FM/ Gd/ Al_2O_3 / Cs/ Si contacts, which indicates the possibility of the formation of two-dimensional electron gas at the n -type Si surface.

Following this, the thesis discusses device-related issues such as proper geometry for the MR observation, where the interface-engineered tunnel contacts are integrated into a full device. Because the spin-MOSFET is based on the two-terminal MR response, stray field effects in the Si channel should be carefully minimized. Also the magnetic properties of nano-scale magnetic elements are investigated, which is needed to design the ferromagnetic source and drain electrodes. It is concluded that with the interface-engineered spin-tunnel contacts developed here, the MR in a full device with a Si channel and

two FM contacts is expected to be observable even if the spin lifetime in the Si is in the sub-nanosecond range. Hence, the spin-tunnel contacts described in this thesis raise prospects for the realization of the Si spin-MOSFET. Moreover, the approaches presented here can be extended to other elements, alloys and compounds, opening up a whole new class of materials for spin-tunnel junctions. The methods developed here to engineer spin-tunnel contacts to Si can be generally applied to semiconductor-based spintronic devices, low RA product applications of magnetic tunnel junctions, but also to metal gates in MOSFETs, and, in fact, to many devices where the work function is important.

Samenvatting

Dit proefschrift gaat over spin-elektronica componenten gebaseerd op silicium en beschrijft onderzoek naar de belangrijkste aspecten en knelpunten voor de ontwikkeling van silicium spintronica componenten, en de oplossingen daarvoor. Door eigenschappen van magnetische materialen en halfgeleiders te combineren en gebruik te maken van de spin van het elektron, geeft halfgeleider spintronica nieuwe mogelijkheden voor de ontwikkeling van elektronische componenten. Een voorbeeld is de Si spin-MOSFET, een spin-transistor met een Si kanaal en twee ferromagnetische contacten, waarbij de geleiding door het kanaal tussen de contacten kan worden beïnvloed via de relatieve oriëntatie van de magnetisatie van beide contacten. Silicium is het aangewezen materiaal voor een spin-transistor, daar het de bestaande halfgeleider technologie domineert, en bovendien kan worden verwacht dat de levensduur van de spin van elektronen in Si zeer lang is.

Voor de ontwikkeling van dergelijke silicium componenten met een magnetoweerstand effect zijn de elektrische injectie, transport en detectie van spin-gepolariseerde ladingsdragers in Si vereist. Dit stelt specifieke eisen aan het ontwerp van de ferromagnetische contacten met het Si, want de contactgrenzen spelen een bepalende rol in de communicatie van de spin informatie tussen ferromagneet (FM) en halfgeleider. Dit proefschrift begint met de specificatie van de eisen die worden gesteld aan de ferromagneet / tunnel isolator / Si contacten zodat een magnetoweerstand kan worden verkregen. Deze eisen zijn een geschikte waarde van het product van weerstand en oppervlak, een hoge waarde voor de tunnel spin-polarisatie, en het gecontroleerd schakelen van de magnetisatie van de contacten.

Ten einde deze eisen te bestuderen zijn FM/Al₂O₃/Si gemaakt. Er is

gevonden dat met zulke contacten, indien daarvoor conventionele magnetische materialen zoals Co en NiFe legeringen worden gebruikt, het niet mogelijk is een significant magnetoweerstand effect te bereiken in een Si spin-MOSFET. Verder blijkt dat de traditionele methode om de tunnel weerstand in te stellen op de gewenste waarde, via de dikte van de tunnel isolator, niet werkt voor zulke contacten. De weerstand van FM/Al₂O₃/Si contacten met Co of NiFe legeringen is 4 tot 8 ordes van grootte te hoog, waarvoor de vorming van een Schottky barrière als de oorzaak is gevonden.

Dit proefschrift beschrijft de ontwikkelde oplossing voor dit fundamentele probleem, waarbij de specifieke eigenschappen van de spin-tunnel contacten gecontroleerd worden aangepast door introductie van een zeer dunne nanolaag van een speciaal materiaal in het contact gebied. Hiermee wordt een brug geslagen tussen het ferromagnetische materiaal en het silicium. Twee verschillende manieren zijn bedacht en verwezenlijkt. In de eerste methode wordt een nanolaag van een ferromagnetische materiaal met een lage werkfunctie aangebracht tussen de ferromagnetische elektrode en de Al₂O₃ tunnel isolator. Door gebruik te maken van een laagje van minder dan 1 nm gemaakt van Gd, een magnetisch materiaal met een zeer lage werkfunctie, is laten zien dat FM/Al₂O₃/Si contacten met een veel lagere weerstand kunnen worden verkregen, omdat de Schottky barrière wordt verwijderd. Verder is laten zien dat door de dikte van de Gd nanolaag te variëren, de hoogte van de Schottky barrière en daarmee de weerstand van de contacten kan worden ingesteld over een bereik van 8 ordes van grootte. En, daarbij is het tevens mogelijk gebleken een redelijk grote waarde voor de tunnel spin-polarisatie te behouden, alhoewel het wenselijk is de verkregen waarde bij kamertemperatuur nog wat te verbeteren. Hiervoor is een begin gemaakt door een beperkt aantal materiaal aanpassingen te bestuderen, maar vele andere materialen zijn nog mogelijk.

De tweede methode om de contact eigenschappen in te stellen, maakt gebruik van een dunne laag van het alkali metaal cesium, aangebracht op het silicium oppervlak voordat de Al₂O₃ isolator wordt gedeponed. Gevonden werd dat ook dit leidt tot een sterke reductie van de Schottky barrière hoogte. In dit geval wordt dat bewerkstelligd door de verandering van de energetische positie van de toestanden aan het oxide/Si grensvlak, waardoor de positie van het Fermi niveau verschuift. Door deze "grensvlak chemie" methode te combineren met de eerste methode gebaseerd op magnetische materialen met lage werk functie, wordt complete controle verkregen over de weerstand en het energie profiel van spin-tunnel contacten op Si. In het bijzonder kan een

geïnverteerde band buiging worden verkregen in FM/ Gd/ Al₂O₃/ Cs/ Si contacten, waarbij de mogelijkheid tot de vorming van een twee dimensionaal elektronen gas ontstaat aan het grensvlak van Si en het tunnel oxide.

Vervolgens is gekeken naar andere aspecten die van belang zijn voor het functioneren van een Si spin-MOSFET met daarin geïntegreerd de ontwikkelde spin-tunnel contacten. De optimale geometrie van de transistor voor de observatie van magnetoweerstand is bekeken, waarbij het minimaliseren van magnetische strooivelden van de contacten een belangrijk aspect is. Ook zijn de magnetische eigenschappen van magnetische elementen met afmetingen op nanoschaal bestudeerd, waarmee de ferromagnetische contacten van de spin-MOSFET kunnen worden ontworpen. De conclusie is dat door gebruik te maken van de in dit proefschrift ontwikkelde spin-tunnel contacten, het mogelijk wordt om een meetbaar magnetoweerstand effect te verkrijgen in een silicium spin-MOSFET zelfs als de spin levensduur van de ladingsdragers in het Si minder dan een nanoseconde is. Dus, de hier ontwikkelde magnetische tunnel contacten met instelbare eigenschappen maken de weg vrij naar een magnetische transistor gebaseerd op spin-transport in silicium. Voor deze nieuwe methoden kan worden geput uit een breed scala van elementen, legeringen en stoffen, waarmee een geheel nieuwe klasse van materialen voor magnetische tunnel contacten is geïntroduceerd. De in dit proefschrift ontwikkelde methoden om de eigenschappen van magnetische contacten op silicium gecontroleerd in te stellen, kunnen in zijn algemeenheid worden toegepast in halfgeleider spintronica componenten en magnetische tunnel juncties, maar ook in toekomstige generaties van niet-magnetische halfgeleider structuren en in diverse andere componenten waarin de werkfunctie een rol speelt.

Acknowledgements

This thesis has benefited greatly from the contribution and support provided by many people.

I would like to express my gratitude to Prof.dr. Cock Lodder for being my *promotor*. I am indebted to him for his continuous encouragement and advice. When I attended his lecture, the group seminar, and the monthly discussion, his enthusiasm gradually spread to me. I am fortunate to be his student, and will be forever grateful to him.

I wish especially to thank my daily supervisor and *assistent promotor*, Dr. Ronnie Jansen. I found that it would be impossible to finish this thesis without his endless support and open-minded discussion. With his superb guidance, I have learned how to plan experiments, analyze the results, and present them.

Additional thanks go to my *promotor* and *assistent promotor*, for they read my drafts of the thesis with great patience and corrected them with tremendous efforts.

I would like to express my gratitude to the members of my Ph.D. defence committee who have taken time out of their busy schedules and given me invaluable comments.

I gladly acknowledge to the financial support from the Netherlands Nanotechnology network, NANOIMPULS and NANONED, supported by the Ministry of Economic Affairs, the Netherlands. My thanks also go to all the members of the NANOIMPULS and NANONED network for the useful discussions.

Johnny Sanderink has greatly assisted the research in many ways. The plasma oxidation chamber and the Cs deposition system are of his masterpieces. I remain indebted to Kazunari Motohashi for the collaboration in the research on the MIS diodes. I am further indebted to Dr. Rogelio Murillo for the help in the laser interference lithography, to Martin Siekman for the help in the MFM measurements, and to Thijs Bolhuis for the technical support related with VSM and computer software. I wish to thank former and present members of the NanoElectronics (NE) group: Dr.

Byong Guk Park, Dr. Ferry Postma, Dr. Ehtsham-ul-Haq, Dr. Hüseyin Gökcan, Dr. Tamalika Banerjee, Mercy Mathews, Rajesh Ramaneti, Ivan Vera Marún, and Yun-jae Lee for the support in research and the useful discussions during the bi-weekly group meeting. It is also my pleasure to express my thanks to former members of the Systems and Materials Group for Information Storage (SMI). I am also grateful to secretaries, Karen Wannyn, Thelma Nordholt-Prenger, and Carolien Wierbos-Post for their help in many ways. Thanks to support from the NE group members and ex-SMI group members, the sixth floor of the Hogekamp has been a paradise for me to conduct my Ph.D. research.

I am indebted to Dr. Rico Keim for the TEM measurements, and to Dr. Emiel Speets for the XPS measurements. I appreciate the wonderful support from the clean-room staffs of the MESA⁺ Institute for Nanotechnology. I appreciate Dr. Ray Huetting and Sander Smits who allow me to use the device simulator. I also wish to thank Harry Steffens for the liquid helium.

I will come back to Korea after staying four years in the Netherlands. I would like to express my appreciation to the people in Korea.

I gladly acknowledge to the financial support from the IT Scholarship Program of the Ministry of Information and Communication, Republic of Korea, supervised by the Institute for Information Technology Advancement (IITA).

I am very grateful to Prof.dr. Sung-Chul Shin in Korea Advanced Institute of Science and Technology (KAIST), and to former and present members of Center for Nanospinics of Spintronic Materials (CNSM) in KAIST. I would like to express my gratitude to Dr. Byungdu Oh and ex-members of the superconductivity research group in LG Electronics; especially to the project leader, Dr. Young-Hwan Choi and the members of the high-temperature superconducting (HTS) microwave front-end system project.

It would be almost impossible to do my Ph.D. study without unrelenting support and sacrifice of my family. I am very grateful to my mother and two sisters, Jeong-Eun and Jee-Eun. My late father would be happy with this thesis. I wish to thank my parents-in-law and two sisters-in-law, Jeong-Ock and Ju-Young as well as the brother-in-law, Chang-Su. I would like to express my gratitude to other family members and friends whom I did not write down all the names. Last but not least, I wish especially to thank my wife, Kyung-Eun.

Curriculum Vitae

PERSONAL DATA

Name: Byoung-Chul Min
Date of birth: January 2nd, 1971
Place of birth: Kyung-Book, South Korea

EDUCATION

08/2003 - 08/2007: Ph.D. in Electrical Engineering, University of Twente, Enschede, The Netherlands. Promoter: Prof. dr. J.C. Lodder, Co-promoter: Dr. R. Jansen.

03/1994 - 02/1996: M.S. in Physics, Korea Advanced Institute of Science and Technology (KAIST), Daejon, South Korea. M.S. thesis: "*Study on the Magnetoresistance of NiFe Thin Films.*" Advisor: Prof.dr. Sung-Chul Shin.

03/1988 - 02/1992: B.S. in Physics. Korea Advanced Institute of Science and Technology (KAIST), Daejon, South Korea.

03/1986 - 02/1988: Gyeonggi High School of Science, South Korea.

PROFESSIONAL EXPERIENCE

- 02/1996 - 07/2003:** Senior Research Engineer, LG Electronics Institute of Technology, Device and Materials Lab, Seoul, South Korea. Research area: High- T_c superconducting (HTS) microwave filter systems for wireless communications. HTS Josephson junctions and dc SQUIDs.
- 04/1992 - 10/1992:** Military Service in the Republic of Korea Navy.

PUBLICATIONS

- [1] B. C. Min, K. Motohashi, J. C. Lodder, and R. Jansen, "Tunable spin-tunnel contacts to silicon using low-work-function ferromagnets", *Nature Materials* **5**, 817 (2006).
- [2] B. C. Min, K. Motohashi, J. C. Lodder, and R. Jansen, "Cobalt- Al_2O_3 -silicon tunnel contacts for electrical spin injection into silicon", *J. Appl. Phys.* **99**, 08S701 (2006).
- [3] B. G. Park, E. Haq, T. Banerjee, B. C. Min, J. C. Lodder, and R. Jansen, "Excitation and transport of hot holes in a magnetic tunnel transistor", *J. Appl. Phys.* **99**, 08S703 (2006).
- [4] B. G. Park, T. Banerjee, B. C. Min, J. C. Lodder, and R. Jansen, "Tunnel spin polarization of $\text{Ni}_{80}\text{Fe}_{20}/\text{SiO}_2$ probed with a magnetic tunnel transistor", *Phys. Rev. B* **73**, 172402 (2006).
- [5] B. G. Park, T. Banerjee, B. C. Min, J. G. M. Sanderink, J. C. Lodder, and R. Jansen, "Temperature dependence of magnetocurrent in a magnetic tunnel transistor", *J. Appl. Phys.* **98**, 103701 (2005).
- [6] B. C. Min, Y. H. Choi, S. H. Moon, S. M. Lee, Sang-Young Lee, and B. Oh, "Double-sided YBCO thin films made by off-axis pulsed laser deposition", *Superconductor Science and Technology* **14**, 543 (2001).
- [7] B. C. Min, Y. H. Choi, S. K. Kim, and B. Oh, "Cross-coupled band-pass filter using HTS microstrip resonators", *IEEE Transactions on the Applied Superconductivity* **11**, 485 (2001).
- [8] I. B. Vendik, A. N. Deleniv, V. O. Sherman, A. A. Svishchev, V. V. Kondratiev, D. V. Kholodniak, A. V. Lapshin, P. N. Yudin, B. C. Min, Y. H. Choi, and B. Oh, "Narrow-band Y-Ba-Cu-O Filter with Quasi-Elliptic Characteristic", *IEEE Transactions on the Applied Superconductivity* **11**, 477 (2001).
- [9] B. K. Jeon, J. H. Kim, C. J. Lee, B. C. Min, Y. H. Choi, S. K. Kim, and B. Oh, "Seven-pole HTS microstrip bandpass filter using non-adjacent coupling of pseudo-lumped element resonator", *Electronic Letters* **36**, 1394 (2000).

- [10] A. Deleniv, D. Kholodniak, A. Lapshin, I. Vendik, P. Yudin, B. C. Min, Y. H. Choi, and B. Oh, "Extracting the model parameters of high-temperature super-conductor film microwave surface impedance from the experimental characteristics of resonators and filters," *Superconductor Science and Technology* **13**, 1419 (2000).
- [11] H. T. Kim, B. C. Min, Y. H. Choi, S. H. Moon, S. M. Lee, B. Oh, J. T. Lee, I. Park, and C. C. Shin, "A Compact Narrow-Band HTS Microstrip Filter for PCS Application", *IEEE Transactions on the Applied Superconductivity* **9**, 3909 (1999).
- [12] Byoung-Chul Min, Young-Hwan Choi, Hong Teuk Kim, Seung-Hyun Moon, Seung-Min Lee, and Byungdu Oh, "High temperature Superconducting Pseudo-Lumped Element Bandpass Filter", *Progress in Superconductivity* **1**, 42 (1999).
- [13] B. C. Min, Y. H. Choi, S. H. Moon, S. M. Lee, H. T. Kim, and B. Oh, " Double sided YBCO Thin Films Deposited on 2-inch LaAlO₃ Wafers by Pulsed Laser Deposition" *Korean Applied Physics (Ungyong Mulli)* **11**, 423 (1998).
- [14] S. H. Moon, B. Oh, H. T. Kim, Y. H. Choi, B. C. Min, Y. H. Lee, H. C. Kwon, Y. K. Park, J. C. Park, "Two channel high-T_c SQUID magnetometer for MCG", *J. Korean Phy. Soc.* **31**, p.342 (1997).
- [15] B. Oh, Y. H. Choi, S. H. Moon, H. T. Kim, and B. C. Min, "YBCO/ NBCO/ YBCO edge junctions and SQUIDS", *Appl. Phys. Lett.* **69**, 2288 (1996).
- [16] Byoung-Chul Min and Sung-Chul Shin, "The Effects of Ar Gas Pressure on the Magnetic and Galvano-magnetic Properties of NiFe Thin Films Prepared by dc Magnetron Sputtering", *Journal of Korean Magnetism Society* **6**, 105 (1996).
- [17] S. -C. Shin, B. C. Min, and C. S. Kim, "Theoretical Consideration for Analyzing Torque Curves of Magnetic Thin Films Having Oblique Anisotropy", *New Physics (Sae Mulli)* **33**, 63 (1993).

PRESENTATIONS

- [1] B. C. Min, K. Motohashi, J. C. Lodder, and R. Jansen, "Spin tunnel contact to silicon with interfacial nanolayers," International Symposium on Advanced Magnetic Materials and Applications, ISAMMA 2007 (Korea, Jeju Island, May-2007). Oral presentation. INVITED TALK.
- [2] B. C. Min, K. Motohashi, J. C. Lodder, and R. Jansen, "Tunable spin tunnel contacts to Si using low work function ferromagnets", The Foundation for Fundamental Research on Matters meeting, FOM meeting @Veldhoven (The Netherlands, Veldhoven, Jan-2007). Oral presentation.
- [3] B. C. Min, K. Motohashi, J. C. Lodder, and R. Jansen, "Tunable spin tunnel contacts to Si using low work function ferromagnets", The 10th JOINT MMM/InterMAG conference (USA, Baltimore, Jan-2007). Oral presentation.

- [4] B. C. Min, K. Motohashi, J. C. Lodder, and R. Jansen, "Tunable spin tunnel contacts to Si using low work function ferromagnets", The 4th International Conference on Physics and Applications of Spin Related Phenomena in Semiconductors, PASPS IV (Japan, Sendai, Aug-2006). Poster presentation.
- [5] B. C. Min, K. Motohashi, J. C. Lodder, and R. Jansen, "Ferromagnet-Al₂O₃-silicon contacts for electrical spin injection into silicon", The 50th annual conference on the magnetism and magnetic materials, MMM (USA, San Jose, Sep-2005). Oral presentation.
- [6] B. C. Min, K. Motohashi, J. C. Lodder, and R. Jansen, "Ferromagnet-Al₂O₃-silicon contacts for electrical spin injection into silicon", The third international school and conference on spintronics and quantum information technology, SPINTECH III (Japan, Hyogo, June-2005). Poster presentation.
- [7] B. C. Min, Y. H. Choi, S. K. Kim, and B. Oh, "Cross-coupled band-pass filter using HTS microstrip resonator," Applied Superconductivity Conference 2000, (USA, Virginia Beach, Sep-2000). Poster presentation.
- [8] B. C. Min, Y. H. Choi, H. T. Kim, S. H. Moon, S. M. Lee, and B. Oh. "High Temperature Superconducting Pseudo-Lumped Element Bandpass Filter", Korean Superconductivity Society 99 (Korea, Yongpyung, Aug-1999). Poster presentation.
- [9] B. C. Min, Y. H. Choi, H. T. Kim, S. H. Moon, S. M. Lee, and B. Oh. "High Temperature Superconducting Pseudo-Lumped Element Bandpass Filter", The 75th Korean Physical Society Spring Meeting (Korea, Seoul, April-1999). Oral presentation.
- [10] B. C. Min, H. T. Kim, Y. H. Choi, S. H. Moon, S. M. Lee, B. Oh, J. T. Lee, I. Park, and C. C. Shin. "A Compact Narrow-Band HTS Microstrip Filter for PCS Application", Korean Conference on Materials and Applications of Superconductivity 1998 (Korea, Yongpyung, Korea, Aug-1998). Poster presentation.
- [11] B. C. Min, Y. H. Choi, S. H. Moon, S. M. Lee, H. T. Kim, and B. Oh, " Double sided YBa₂Cu₃O_{7- δ} Thin Films Deposited on 2-inch LaAlO₃ Wafers by Pulsed Laser Deposition", Korean Conference on Materials and Applications of Superconductivity 1997 (Korea, Yongpyung, Aug-1997). Poster presentation. BEST POSTER AWARD.

*Sit down before fact as a little child,
be prepared to give up every preconceived notion,
follow humbly wherever and to whatever abysses nature leads,
or you shall learn nothing.*

Thomas Henry Huxley (1825-1895)
British biologist

